THESIS FOR THE DEGREE OF DOCTOR OF PHILOSOPHY

Biomolecule Trapping With Stimuli-Responsive Polymer Coated Nanostructures

Justas Svirelis

Department of Chemistry and Chemical Engineering
CHALMERS UNIVERSITY OF TECHNOLOGY
Göteborg, Sweden 2022

Biomolecule Trapping With Stimuli-Responsive Polymer Coated Nanostructures

Justas Svirelis

ISBN 978-91-7905-739-8

Doktorsavhandlingar vid Chalmers tekniska högskola

Ny series Nr. 5205

ISSN 0346-718X

Department of Chemistry and Chemical Engineering
Chalmers University of Technology
SE-412 96 Göteborg
Telephone 031-772 10 00

Cover:
"A trapped life" rendered by Justas Svirelis (RemasH on Discord) on Midjourney, used under CC BY-NC 4.0.

Printed by Chalmers Reproservice

Göteborg, Sweden 2022

Biomolecule Trapping With Stimuli-Responsive Polymer Coated Nanostructures

Justas Svirelis
Chemistry and Chemical Engineering
Chalmers University of Technology

Abstract

Trapping biomolecules in nanosized gaps is of great interest in novel systems for single molecule analysis and membranes, which filter biomolecules. Current platforms are lacking in full functionality to facilitate biomolecule trapping and transport in their native environment and without covalent tethering to surfaces. Thus, we propose a system of thermo-responsive polymer poly(*N*-isopropylacrylamide) (PNIPAM) coated nanostructures, which are suited to controllably trap and release proteins, and overcome such challenges. PNIPAM polymer brushes (i.e. the barrier for proteins) on nanostructures were prepared via Activators Regenerated by Electron Transfer Atom Transfer Radical Polymerization (ARGET-ATRP) by employing a self-assembled monolayer of initiator molecules for the reaction. Variation of PNIPAM reaction time and/or solvent constituency during the polymerization results in different swollen/collapsed polymer brush thicknesses, indicated by the plasmonic shifts in extinction spectroscopy and surface plasmon resonance experiments. By having sufficient polymer film thickness and grafting density for nanowells, e.g. 120 nm, polymer conformational change below and above LCST allowed for controlled gating of these nanostructures. This feature was used to allow or block proteins from entering the interior of the nanostructures (small molecules diffuse freely in both states) as investigated by nanostructure plasmonic activity (extinction spectroscopy) and fluorescence microscopy below and above PNIPAM lower critical solution temperature (32 °C in water). In addition, with fluorescence microscopy experiments we showed that it is possible to trap and release many proteins with single nanowell resolution.

Keywords: Poly(*N*-Isopropylacrylamide), poly(ethylene glycol), polymer brushes, surface plasmon resonance, fluorescence microscopy, quartz crystal microbalance with dissipation monitoring, biomolecule transportation, protein interaction

List of Publications

This thesis is based on the following papers:

I. Surface plasmon resonance sensing with thin films of palladium and platinum–quantitative and real-time analysis

J. Andersson, J. Svirelis, G. F.-D. Del Castillo, T. Sannomiya and A. Dahlin

Physical Chemistry Chemical Physics, 24 **(2022)** , *4588–4594*

II. Accurate Correction of the "Bulk Response" in Surface Plasmon Resonance Sensing Provides New Insights on Interactions Involving Lysozyme and Poly (ethylene glycol)

J. Svirelis, J. Andersson, A. Stradner and A. Dahlin

ACS sensors, 7 **(2022)** , *1175–1182*

III. Pore performance: artificial nanoscale constructs that mimic the biomolecular transport of the nuclear pore complex

J. Andersson, J. Svirelis, J. Medin, J. Järlebark, R. Hailes and A. Dahlin

Nanoscale Advances, **(2022)**

IV. Stable Trapping of Multiple Proteins at Physiological Conditions Using Nanoscale Chambers with Macromolecular Gates

J. Svirelis, Z. Adali, G. Emilsson, R. Vattikunta, J. Andersson, K. Kolman, O. Olsson, Y. Sakiyama, R. Y. H. Lim and A. Dahlin

Preprint available. To be submitted to Nature Communications, 2022

My Contributions to the Publications

Paper I

Performed half of the Surface Plasmon Resonance experiments and took part in the Fresnel model calculations for layer thickness determination. Also, participated in writing and editing the manuscript.

Paper II

Performed all of the experimental work (i.e. SPR measurements). Also, have participated in majority of the quantitative calculations, written the first manuscript and helped editing the final version.

Paper III

Written a significant part of the review paper manuscript and helped forming the discussion and future outlook sections with J.A. and A.D., thus share the first co-authorship.

Paper IV

Performed the majority of experimental work (e.g. developed the synthesis protocol, extinction, SPR, QCM-D and fluorescence experiments) and designed a custom made flow cell. Participated in writing and editing the manuscript.

Additional publications which are not included in the thesis:

Video Speed Switching of Plasmonic Structural Colors with High Contrast and Superior Lifetime

K. Xiong, O. Olsson, J. Svirelis, C. Palasingh, J. Baumberg and A. Dahlin

Advanced Materials, 33 **(2021)** *, 2103217*

Role of sulphation pattern in modulating the interactions between human papillomavirus and cell surface glycosaminoglycans at the single particle level

F. Banoa, L. Soria Martinez, K. Seier, D. Conca, E. Heidenfels, J. Svirelis, K. Throssteinsson, A. Dahlin, M. Schelhaas and M. Bally

In manuscript, 2022

Contents

List of Figures

List of Tables

1 Introduction

Life is the most precious diamond we have on planet Earth. It includes a variety of different organisms - plants, animals, bacteria, etc. But how much knowledge do we have about life, really? It seems that over centuries researchers have put in a great effort to create tools, which help understand the foundation of life. The current understanding we have about what we call life is that it consists of building blocks called molecules, which take shape in a variety of forms. Some examples include proteins, DNA, metal complexes, polymers and others. Until now, scientists have mostly looked at an ensemble of molecules, constituting an organism. In this thesis, we will focus on some of the cell's most prominent vehicles - proteins.

Proteins are responsible for a vast number of functions in an organism and have been investigated since the discovery of 3D structure of myoglobin by John Kendrew *et al*. in 1958 [7]. These include how different collective functions of such biomolecules influence muscle, protection, digestive, cognitive, hormonal and other self-regulatory work happening inside each one of us. On the protein level, the functions come down to enzyme activity [8], protein-protein interaction [9], protein oligomerization [10, 11] and others. Until recently, most studies on proteins were looking at ensembles, but it is necessary to look at single molecules as they can function individually as well. This means that if ensemble methods are used to examine groups of molecules, they would usually generate mean average values of the system. However, if single molecule methods are applied, a more probabilistic distribution is achieved (including sides of the mean). This could possibly lead to new (or previously unidentified) energetic or conformational states of proteins, because now the whole distribution of possible conformations would be analysed. In addition, it was shown that proteins can have unfamiliar crowding effects on one another when in a group within a living cell (e.g. variation in conformation) [12].

It has been known for decades now, that proteins exist in a variety of conformations, varying over a certain period of time (e.g. millisecond range) in the same [13, 14] or different environments [15]. Investigating single protein's molecular structure, shape and function, separately from the ensemble, however, is limited by the tools currently available [8, 15–17]. Nowadays, x-ray crystallography and nuclear magnetic resonance techniques can help us identify the structure of a protein when it is in a certain equilibrium or sometimes in dynamic ensemble systems [18–21]. Unfortunately,

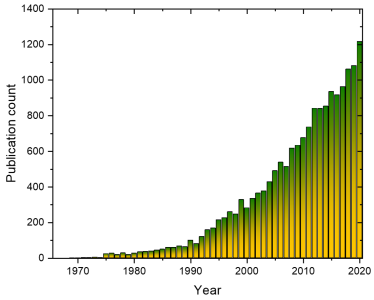

Figure 1.1: Annual publication count according to PubMed on IDPs and IDPRs, by using such terms in the search panel: inherently/natively/intrinsically and disordered/unfolded/unstructured proteins [23]

these techniques are either capable of measuring ensembles (X-ray crystallography) or not sensitive enough to study single proteins with intrinsic disorder (NMR), thus leading to an inaccurate determination of the structures. This is because the structure of a single molecule is averaged out by other molecules in the ensemble, making the analysis devoid of heterogeneity [22]. Intrinsically disordered proteins are such, that their residue Ramachandran angles and backbone atoms undergo small-amplitude changes relative to their local environment [14]. These random fluctuations are not defined by equilibrium positions over time-averaged values and are dynamic in nature [13]. The proteins might be intrinsically disordered as whole molecules, also known as intrinsically disordered proteins (IDPs), or have regions, which are partially disordered (intrinsically disordered protein regions or IDPRs). IDPs and IDPRs have received a significant increase of interest from the research community over the last decades. As can be seen in fig. 1.1 the rough estimation of yearly publication count reached over one thousand in the last years (e.g. on PubMed only) [23]. Moreover, according to the Protein Data Bank (PDB), less than 1/3 of the known crystal structures are completely devoid of disorder [24].

IDPs and IDPRs were shown to have concrete functions in the organism such as cellular signalling and regulation [27–31]. Because IDP might change it's function over time by re-arranging conformation, it could disrupt cellular processes [13, 14, 27, 32, 33]. An example of this could be IDP participation in pathological transformation of the biological cell leading to cancer [34].

In the midst of the pandemic, protection against the SARS-CoV-2 virus were able to be manufactured, because the structure of it's surface S protein is known (fig. 1.2, bottom) [26]. On the other hand, there are proteins, such as fibrinogen (known for it's participation in coagulation cascade and thrombosis), which does not have an equilibrium conformation due to evident IDPR (marked in grey in fig. 1.2, top). This IDPR is involved in blood clotting as it binds to several components in this process, which is allowed by the flexibility of IDPR [35–38]. If this IDPR would not exist, it is possible that the blood clotting would not happen.

In order to resolve single molecules and their interaction with others, an increasing number of light microscopy and other tools are being created every year. Such methods include fluorescence correlation spectroscopy (FCS) [39, 40], photoactivated localisation microscopy (PALM) [41], stimulated emission depletion microscopy (STED) [42], stochastic optical reconstruction microscopy (STORM) [43], Förster energy resonance transfer (FRET) [44], optical/magnetic tweezers [45, 46], atomic force microscopy (AFM) [47], etc. However, all of these have certain issues to get a clear picture of

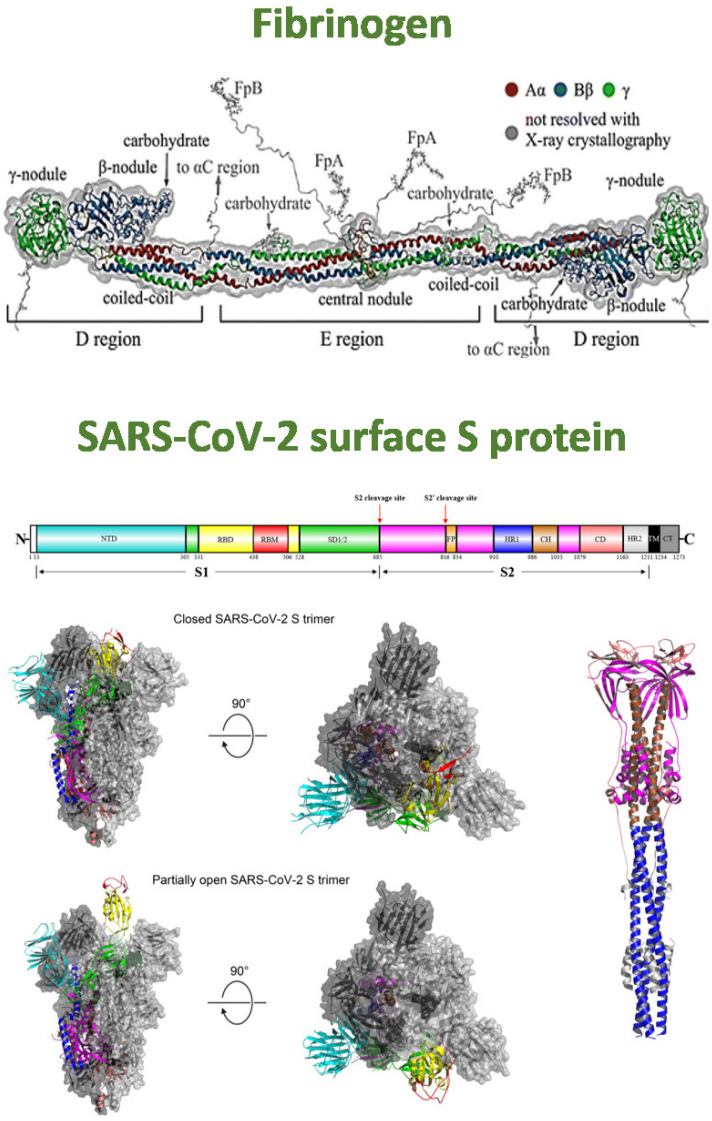

Figure 1.2: Partially intrinsically disordered Fibrinogen protein (top) and well established SARS-CoV-2 surface S-protein precursor structure (bottom; full domain arrangement may be seen above the protein schematics). Only around ~2/3 of the Fibrinogen molecule is resolved by X-ray crystallography. Adapted from Weisel *et al*. and Duan *et al*. [25, 26]

how single proteins behave in their native environment. These include: limited observation time due to diffusion (e.g. milliseconds), low signal/noise ratio, unwanted forces acted upon biomolecules, tethering to surfaces (e.g. limiting protein activity, conformation freedom and function [48]), requiring cryogenic temperatures and solid phase, etc. [17]. Therefore, to study single proteins in their native environment, a nanoscale gating system has to be created, where they would be trapped in a small volume, but remain free to diffuse and exist in a variety of conformations. Previously reported nanoscale systems such as junctions and channels were not able to resolve the protein localisation problem [49]. Moreover, nanoscale trapping systems, such as liposomes (or lipid vesicles), for single molecule trapping already exist and could be used in physiological conditions (i.e. native environment) [50]. However, the number of encapsulated biomolecules compared to the liposome total volume is small in practice, the surrounding liquid around the proteins

inside the liposomes is difficult to exchange without destroying the trapping system and molecule loading inside lipid vesicles has relatively poor yield. Another very recent example of trapping single proteins with electro-osmotic traps and allowing label free monitoring of their conformations is shown by Schmid *et al* [51]. Indeed, these traps allow for a single protein conformational change tracking as exemplified with the protein Hsp90. Yet, the throughput is still low (1 protein in one pore per experiment), only one molecule can be trapped per event (no protein interactions can be observed), there are electro-osmotic forces acting upon the trapped protein (possibly reduces degrees of freedom) and the conducted experiments are not under physiological conditions (e.g. too low salt concentration must be used in comparison to the native environment). These reduce the wide applicability of such systems for studying other proteins, such as serum proteins.

Driven by the need to create systems, which would overcome all of the previously mentioned issues, the main topics, which will be addressed in this thesis are:

1. Is it possible to create a platform, which could trap and release proteins in nanosized compartments at will, while ensuring close to physiological conditions?
2. Are surface sensitive effects, such as surface plasmon resonance, sufficient to monitor gating of protein transport?
3. Can polymer functionalized surfaces be used as repellents for proteins and is it possible to observe this by employing surface plasmon resonance?
4. Can functionalization pathways be probed in surface plasmon resonance experiments with platinum and palladium surfaces (e.g. palladium was also shown useful as a zero-mode waveguide [52])?

Consequently, to approach some of these questions one has to consider several requirements for the protein trapping platform:

- The system should contain a very small volume (e.g. one attoliter) and preferably be an array to increase the throughput of single molecule experiments.
- The system cannot perturb, damage, or produce any unwanted forces (e.g. electrostatic traps and field gradients [53–55]) on the studied single molecules.
- It should allow volume exchange, so that other small molecules could be injected and monitored for interaction.
- The proteins must be allowed to freely diffuse inside the nanochambers, so that their activity is not hindered in any way.

- Native environment (or close to), in terms of pH, salt concentration, temperature, etc., should be established, so that information about how the protein behaves in *in vivo*.
- The system could be used in combination with several techniques (e.g. TIRF, FRET, etc.).

Taking into consideration all of the above, we propose gating protein transport with polymer brush functionalized nanoscale chambers [56], e.g. ***nanowells*** (fig. 1.3 (a, b, c top layer and d, left) or ***nanocaves*** (fig. 1.3 (c bottom layer and d, right). In this thesis, only nanowell structures will be used as nanocompartments for trapping proteins.

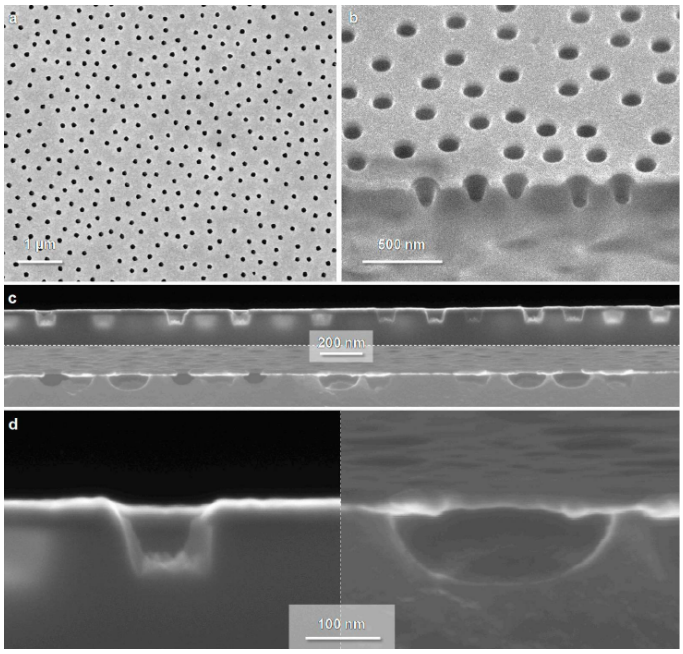

Figure 1.3: Scanning electron microscope images with cross-sections of the nanoscale chambers, nanowells ((a), (b), (c, top), (d, left) and nanocaves ((c, bottom), (d, right); cut with focused ion beam (FIB). Adapted from Malekian *et al.* [56]

Nanowells are functionalized with thermo-responsive polymer brushes of poly(*N*-Isopropylacrylamide) (PNIPAM; fig. 1.4) via Activators Regenerated by Electron Transfer Surface Initiated Atom Transfer Radical Polymerization (ARGET-SI-ATRP). The nanocompartments are composed of silica, gold (30 nm), and a thin (~2 nm) adhesion layer of Cr in between them. PNIPAM polymer brushes, which are end-tethered to the gold surface, allow for protein translocation due to conformational chain collapse when a small change in temperature is induced (fig. 1.5 bottom; from room temperature to ~32 °C in aqueous solutions [57]). When polymer brushes are in the swollen (extended) state, they act as an impenetrable entropic barrier (such as poly(ethylene glycol)(PEG) polymer brushes [58]) and proteins are blocked from entering the nanowell interior (fig. 1.5 top).

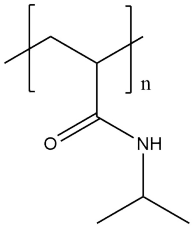

Figure 1.4: Temperature responsive PNIPAM polymer used as an entropic barrier after being grafted on nanochambers.

This artificial system is partially inspired by the nuclear pore complex (NPC), where molecule translocation is governed by intrinsically disordered nucleoporins in the vicinity of the structure

and its intricate pathways [59]. We reviewed up to date artificial systems, which are motivated by the nuclear pore complex, and discussed challenges associated with them in **paper III**. In our case, protein transportation happens by diffusion and further electrostatic attraction to the interior of the nanowells (e.g. silica) at slightly below physiological pH. When pH is tuned to above 7.4, the proteins are repelled from the interior due to their net negative charge, but are blocked from leaving the nanowells by extended and densely grafted polymer chains. In this way, they can diffuse freely without any constrictions on their degrees of freedom and interact with other biomolecules. Further protein analysis (e.g. conformational shape change over time) is out of the scope of this thesis. Nevertheless, this platform, which in part mimics the nuclear pore complex, could become one of the ground establishments for further single molecule studies by techniques mentioned previously.

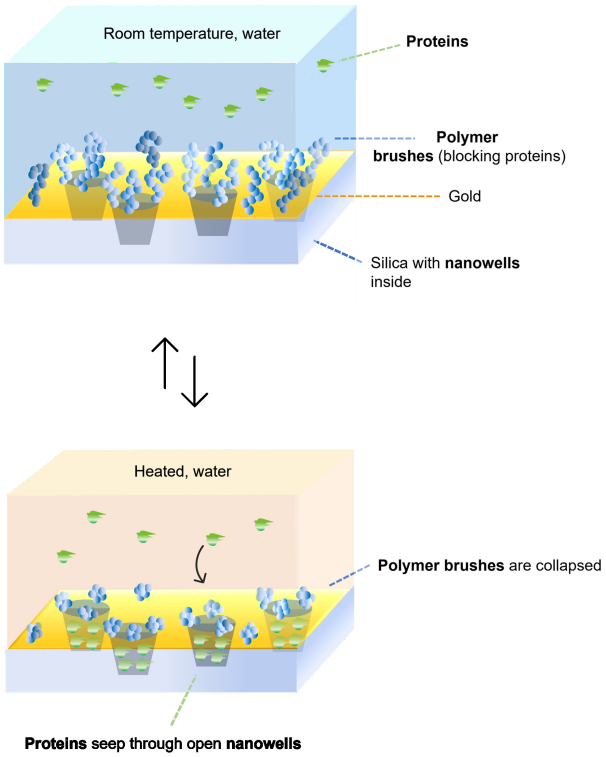

Figure 1.5: Polymer brush functionalized nanostructure gating mechanism for protein transport. The dimensions of items in the figure are not the same as the real objects and are altered for illustrative purposes.

In this thesis, biomolecular interactions and adsorption on surfaces are generally monitored by the surface plasmon resonance (SPR) and quartz crystal microbalance with dissipation monitoring (QCM-D). However, other techniques such as extinction spectroscopy and fluorescence microscopy are utilized as complementary methods to observe protein transport to and from nanowell interior.

Theory 2

Some rewritten sections and figures in this chapter are taken from my licentiate thesis.

2.1 Polymers

In 1920 H. Staudinger proposed that molecules, which have repeat units, or monomers, interconnected with each other via covalent bonds should be called polymers [60]. The main difference between polymers and other molecules is their large size. Throughout history people have been using polymers in their daily life, despite not knowing anything about their structure. A good example of a naturally occurring polymer is caoutchouc. It was used as a material for water proof roofs and containers in more recent ages. Around 3670 years ago it could also have been used in some of the Mesoamerican ball games [61, 62].

In the beginning of the 20^{th} century, scientists were synthesizing polymers without realizing their molecular size. Nevertheless, they noted down the fundamental concepts underlying these reactions, which are still used nowadays. Therefore, the theory, presented in this section, will serve as an overview about some of these fundamental topics. In addition, this part of the chapter will include a short discussion about polymer brush physics, grafting techniques, applications, an example of temperature-responsive polymer brush poly(N-isopropulacrylamide)(PNIPAM) and poly(ethylene glycol)(PEG).

2.1.1 Polymer chains

Assembling monomers into a larger chain (e.g. polymer) via covalent bonds is called a polymerization reaction. The degree of polymerization N is the number of repeat units in a polymeric chain. When polymer's molecular weight M is known, one can determine the degree of polymerization N from this equation:

$$M = NM_{monomer} \tag{2.1}$$

where $M_{monomer}$ is the molar mass of one repeat unit inside the macromolecular chain.

An example of polymeric structure can be seen in figure 2.1. In this case, a polymerization reaction of vinyl monomers is presented,

where R is any chosen functional group. The degree of polymerization N is denoted after brackets to indicate how many monomers exist in the chain. However, sometimes small letters are used to show the number of different monomers in the polymer instead. In the case, where two different types of monomers exist in the polymer chain, N will result in the sum of n and p.

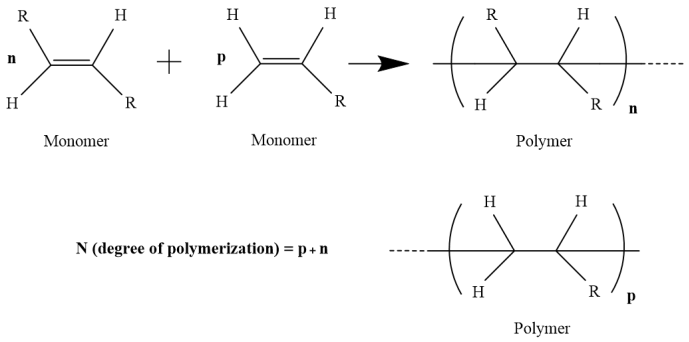

Figure 2.1: An example of a chemical structure of a polymer.

Polymers containing only one type of repeat units are called homopolymers. If linear polymers consist of tens of thousands of monomers, which are interconnected with each other, their physical properties are prone to change. This can cause the application of the polymer to change due to rising melting point with the number of backbone repeat units. [63] Besides the linear form, other shapes, such as dendrimer, ring, etc. exist as well. Also, having different types of monomers in the chain, will result in heteropolymers (e.g. deoxyribonucleic acid (DNA), which may contain 4 different monomers).

Among other important parameters describing polymer chains, are radius of gyration R_g, Kuhn's length b (in the scope of a *freely jointed chain model* (not discussed in detail further) and polydispersity I. Polymer chain size, characterized by radius of gyration, can be written as [63]:

$$R_g^2 = \frac{1}{N}\sum_{i=1}^{N}(R_i - R_{cm})^2 \tag{2.2}$$

It is described by the average squared distance R_i between each monomer in a given environment and the chain's center of mass R_{cm}.

The Kuhn length b is a parameter (within the *random-walk model*), which expresses how stiff the polymer is. One can calculate Kuhn's length by taking the ratio between the mean-square end-to-end distance $\langle R^2 \rangle$ (equal to $[abN]^{1/2}$, where a is the monomer size) and R_{max}, which is the maximum extension of the polymer (eq. 2.3):

$$b = \frac{\langle R^2 \rangle}{R_{max}} \tag{2.3}$$

Finally, the polydispersity index I of polymer chains (eq. 2.4) describes the molecular weight distribution of different lengths of chains existing in the measured sample:

$$I = M_w/M_n \tag{2.4}$$

where M_w and M_n are weight-average and number-average molecular masses. M_n takes into account a fraction of molecules with a specific N, whereas M_w considers the weight fraction of certain molecular weight individual chains [63]. The larger the ratio between these molecular weights is, the wider the distribution of polymer chain molar masses. Polydispersity index can be explained by deviance in polymer chain length due to chain termination, for example.

Now that the important parameters describing the polymer chain have been introduced, polymer chain's free energy relation to the chain conformational entropy, excluded volume entropy and interaction with the solvent will be discussed. These terms give an indication of how polymers behave in a certain medium. First of all, the excluded volume entropy consists of one polymer segment volume, which is denied to be occupied by another. In a good solvent, this results in an increase in free energy by

$$\Delta S_{seg} = -\frac{k_B N \nu}{r^3} \tag{2.5}$$

here k_B is Boltzmann's constant, r is the end-to-end distance of the polymer chain and ν is the excluded volume of a repeat unit. Then, if one still assumes the freely joint chain and random walk model for a polymer chain, the conformational entropy can be expressed as:

$$S = \text{constant} - \frac{3k_B r^2 \nu}{2abN} \tag{2.6}$$

here a - is the size of the monomer and b is the Kuhn's length, which is always larger than a. Taking all of these constituents into account, the total free energy of a polymer chain then is

$$G(r) = \frac{3k_B T r^2}{2abN} + \frac{k_B T \nu N^2}{r^3} - \frac{k_B T \nu X N^2}{r^3} + \text{constant} \tag{2.7}$$

In one of the terms, a dimensionless interaction factor X appears, which contains polymer-polymer, polymer-solvent and solvent-solvent interaction energies [64]. When X is equal to 1,

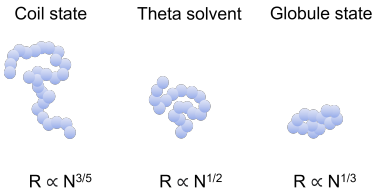

Figure 2.2: Different polymer shapes in solution resulting from dominating interactions.

the *theta solvent condition* is achieved. In this case solvent interaction energies are compensated by the excluded volume effect. If the factor is below 1, the polymer chain becomes a coil, however, when X is higher than 1, the polymer chain turns into a globule-like conformation. Moreover, eq. 2.7 can be further simplified to:

$$G(r) = \frac{3k_BTr^2}{2abN} + \frac{k_BT\nu N^2}{r^3}[1 - X] + \text{constant} \tag{2.8}$$

Lastly, when polymers are in different media, different scaling laws apply in terms of r and N as seen in fig. 2.2.

2.1.2 Polymer brushes

Polymers, tethered to surfaces, have been studied since 1950s and their use as possible anti-flocculants for colloidal particles is well known [65]. There can be various forms of polymers attached on an interface by one end and free on the other (e.g. solid-air or solid-liquid) [66–68]. Some of these include grafted polymers (also copolymers) on solid substrate, micelles, etc (as seen in fig. 2.3). Chain elongation is known as a common property of tethered polymers at interfaces. There are a lot more various types of polymers tethered to surfaces, however, in this thesis only homopolymer end-grafted polymer brushes will be focused on.

Polymer brush conformation refers to tightly packed polymer chains end-grafted on a substrate, which is possible to achieve by using certain grafting techniques discussed later in the thesis. Due to high grafting density of the brushes, a significant osmotic pressure is generated. It can be applied in colloidal system stabilization, for example [65, 68]. When compared to freely random-walking polymer chains in solution, polymer brushes stretch out from the surface into the solution [68]. Therefore, they can be used as coating materials for anti-fouling properties [69], to reduce friction [70] and others.

2.1.3 Polymer brushes in a solvent

The pioneers of surface-tethered polymer chains are Alexander [71], de Gennes [72] and Cantor [73]. They distinctively mentioned the unique characteristics of grafted polymers in the late 1970s - early 1980s. Since then, the structure of end-attached polymer chains remain mainly described by numerical and analytical Self-Consistent Field (SCF) estimations, but some neutron reflectometry measurements exist [74, 75].

To understand how polymer brushes behave in different media, several parameters have to be kept in mind. First of all, due to interface confinement, polymer brushes exhibit configurational free state limitation. Secondly, monomer-monomer interactions are dominating, because the chains are forced to have contact points to each other due to dense packing. This results in chain stretching from the substrate surface into the solution and increasing film thickness L. Also, according to Alexander's model the overall Gibbs free energy G between two segments (from eq. 2.9) in the chain is reduced [71], which is a consequence of this stretching (the interaction energy per coil G_{int} is diminished by the increase in elastic free energy G_{el}). Moreover, the model describes a non-adsorbing and even surface, where monodisperse polymer chains are grafted.

$$G = G_{int} + G_{el} \tag{2.9}$$

In general, it is possible to describe polymer brushes as tethered elongated chains, containing a specific diameter a and a number of monomeric units N. They are grafted at an average length d between each other and this parameter is estimated to be much smaller than the radius of gyration of a free polymer chain. These variables are the main constituents when considering the polymer brush layer equilibrium thickness (solvent contribution is excluded here as was mentioned in subsection 2.1.1). However, it is not so easy to evaluate polymer brush thickness numerically and experimentally and some assumptions have to be made. When monomer units are proposed as steps in the whole chain depth profile, one can consider having a constant segment concentration ϕ in the film (e.g. $\phi \approx Na^3/d^2L$). From this, the free ends of the grafted chains are assumed to be at the same distance, which is perpendicular to the surface they are grafted at [68, 76].

To solve the free energy of an ideal polymer chain (within the random walk model (not discussed in detail further) with reduced configurational entropy, it is possible to make an estimation, known as *Flory approximation*, suggested by Flory [77]. By applying this theory to polymers on the surface, the free energy per unit chain in terms of thermal energy units k_BT can be written as [67, 68]:

$$G/k_BT = \frac{\nu\phi^2 d^2 L}{a^3} + \frac{L^2}{R_0^2} \tag{2.10}$$

here R_0 is the radius of an ideal polymer chain (e.g. $\propto N^{1/2}$) and d is the distance between grafting sites. When G is minimized with respect to L, the equilibrium thickness of the brush film can be calculated by:

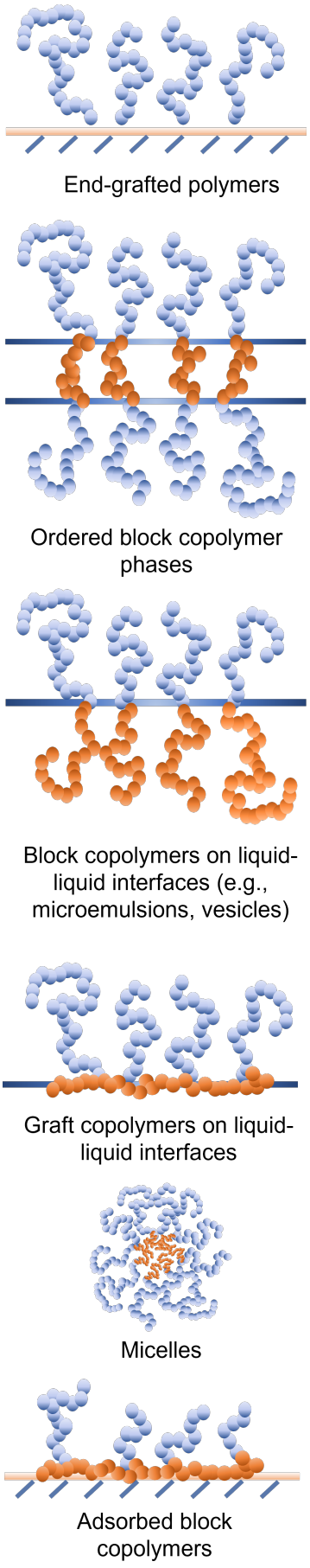

Figure 2.3: Tethered polymer chains in different configurations.

$$L/a = N\left(\frac{a}{d}\right)^{\frac{2}{3}} \tag{2.11}$$

This approximation tells us how polymer brush equilibrium thickness is related to the degree of polymerization when in a good solvent. However, if surface tethered polymers, are in a medium, where the interaction with the environment molecules (e.g. solvent) is less favorable, the relation can differ significantly (also, when compared to free chains) [68, 78, 79]. The scaling relationships are illustrated in table 2.1.

Table 2.1: Polymer chain equilibrium thickness scaling in different media.

Solvent	**Polymer brush**	**Free polymer**
Good solvent	L/a $\sim N(a/d)^{2/3}$	$R \sim N^{3/5}$
Theta solvent	L/a $\sim N(a/d)$	$R \sim N^{1/2}$
Poor solvent	L/a $\sim N(a/d)^2$	$R \sim N^{1/3}$

Alexander's model for polymer brushes is a straightforward way to find the minimum free energy of polymer chains as it is influenced by the balance between chain-chain repulsion and stretching. In addition, the scope of it reaches the hydrodynamic properties of tethered polymer chains as well (e.g. compressibility, permeability and hydrodynamic thickness) [68]. However, there are several issues with the model - it is not known where the free chain ends are at any time point, how the polymer chains interact with each other (e.g. separate or intertwine) and the distribution of the monomeric density cannot be correctly estimated. Nevertheless, in Milner's self-consistent field method, a parabolic profile can be used to approximate the real monomer density within the brush and expressed as:

$$\phi(x) \propto [L^2 - z^2] \tag{2.12}$$

here z is a certain distance from the surface and L is 'the Milner height' [80]. The function shows that the film density is highest when taken at graft points and smallest when the distance is at the boundary of the brushes. However, in this model, it assumed that the free ends of tethered polymer chains may be located at any distance from the surface.

2.1.4 Polymer grafting techniques

There are a few polymer chain tethering methods used nowadays [68, 81, 82]. A representation of the two most common ones - grafting-to and grafting-from can be seen in figure 2.4 [81].

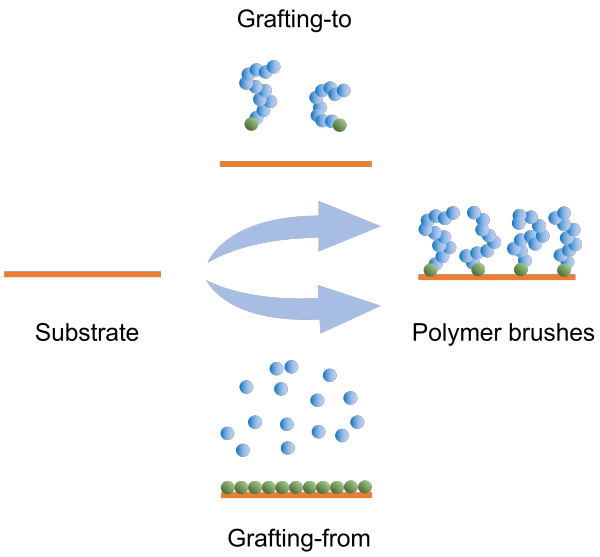

Figure 2.4: The most common polymer chain grafting strategies.

Firstly, the grafting-to technique includes only one step polymer tethering process. The polymers, to be attached, would contain chemically or physically surface favoring end-groups (e.g. thiol), which allows for polymer binding [83]. In a way, this method is more advantageous than grafting-from, where initiator molecules are used as a precursor for the growing polymer chain, because the grafting density of the film can be determined from the known molecular weight, polymer density and thickness of the film. In contrast, the molecular weight of polymers, grafted with grafting-from, is difficult to determine, because the cleaved off brush concentration is too low for instruments to detect [84]. One of the disadvantages of the grafting-to method is that the produced polymer brush layer (e.g. for longer chains) grafting density is usually lower than grafting-from [85–88]. This may result in worse antifouling properties of the functionalized surfaces than expected [89]. Thus, it is important to know what the grafting density Γ (chains/nm^2) on the surface is. However, Γ is usually not known in cases, where polymers are grafted-from the surface [58, 90, 91].

If the polymer molecular weight and thickness are known, Γ can be readily determined by [92]:

$$\Gamma = \frac{h \rho N_A}{M_n} \tag{2.13}$$

here, h is dry polymer layer thickness, ρ is the density of the polymer brushes, N_A is the Avogadro's number and M_n is the polymer number-average molecular weight. In some cases, if the polymer brush film thickness is not known, it is possible to use the mass-based coverage of the cleaved polymer chains to calculate the grafting density [93].

The grafting density and the monomer volume fraction Φ inside the brush are closely related and can be expressed through Alexander-de Gennes solvated brush model (eq. 2.14; [94]):

$$\Phi \sim g_d(a/d)^3 \sim \Gamma^{2/3} \tag{2.14}$$

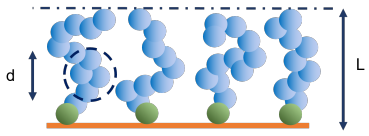

Figure 2.5: Alexander-de Gennes polymer brushes with a blob area marked inside.

here g_d is the number of monomers inside a Alexander-de Gennes blob and d is the size of the blob (fig. 2.5). The blob is a hypothetical region inside a polymer chain, where this segment can be in a certain conformation and occupy a specific volume. Usually, several monomers are included in the blob and its size corresponds to d or $ag_d^{3/5}$. Taking this into account, one can determine the volume per tethered polymer chain, which is Ld^2.

Furthermore, the grafting density plays a huge role in the polymer brush conformational freedom. If the distance between the grafted chains d is smaller than radius of gyration R_g, then the resulting conformation is a polymer brush with tightly packed polymer chains (as seen in fig. 2.6; [83, 84, 95]). In contrast, if d is higher than R_g, then the surface tethered polymers will be in a mushroom-like state.

The grafting-from method has a significantly large advantage over grafting-to method in terms of the thickness of the polymer layer, which can be produced. Also, the thickness can be tuned by terminating and re-initiating the polymerization reaction whenever is necessary [96, 97]. Therefore, each technique should be applied depending on what kind of resulting film is required for a specific application.

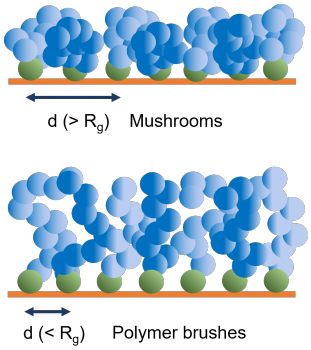

Figure 2.6: Mushroom and brush conformations resulting from different grafting densities of the polymer chains.

One of the most popular ways to manufacture polymer brush films with grafting-from method is Surface Initiated - Atom Transfer Radical Polymerization, or SI-ATRP [95, 98–100]. This type of polymerization has been independently invented by Mitsuo Sawamoto [101] and Krzysztof Matyjaszewski [102] in the mid 90s. There are several directions, in which SI-ATRP can be conducted, including light mediated [103], electrochemical [104], activator regenerated by electron transfer (ARGET) [97] and others. In this thesis, we chose to apply the ARGET version to produce polymer brush layers on nanowell structures as gating systems for protein transport as this method yields fast and relatively controlled reaction for the conditions chosen and explained later on. The reaction scheme is shown in the following figure 2.7 [81, 83].

Here $R-X$ species refer to a self-assembled initiator monolayer on a substrate, containing a halogen moiety (e.g. bromide). This functional group can readily be transformed into a radical and act as initiator molecule for the polymerization reaction. The radical $R\cdot$ is produced when Cu(I) species are present and acts as a catalyst

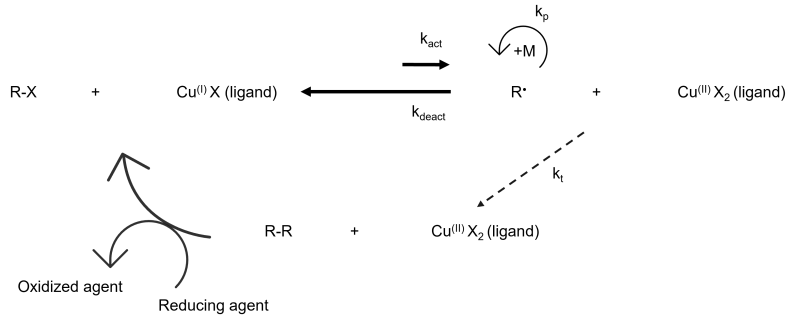

Figure 2.7: ARGET-ATRP reaction scheme.

through a electron transfer process (e.g. oxidation of Cu(I). The rate k_{act}, at which the reaction is activated, is smaller than the reversible reaction rate k_{deact}, thus the number of radicals present is restricted. However, when the propagation of the polymer chain starts at a rate k_p, Cu(I) is converted to Cu(II). In this case, at some point of time the reaction would terminate, but in the presence of a reducing agent (e.g. ascorbic acid; decreases the oxidation state of Cu(II) to the initial), it continues until manually stopped. It is possible to terminate the reaction by exposing it to ambient oxygen or just leave it running until all the monomers are consumed.

Generally, ARGET-ATRP technique is better than others as it is relatively robust, can operate in significantly high oxygen tolerance, and requires small amounts of catalyst [105, 106]. Even so, this SI-ATRP method is still difficult to control due to the factors influencing the kinetics of reaction such as the type of catalyst [107], monomer and ligand [108], and their concentration [97], type of solvent [109], temperature [110] and pressure [111]. This might result in inhomogeneities of the polymer brush film.

In this thesis, the conditions for ARGET-ATRP (grafting-from) to polymerize PNIPAM and attachment of thiolated poly(ethylene glycol)(PEG; grafting-to) were adapted from Emilsson *et al*. [112, 113] as starting points. However, the method was further improved to achieve better reproducibility of the polymer brush layers in terms of uniformity and thickness for necessary applications.

2.1.5 Poly(ethylene glycol) PEG

Poly(ethylene glycol)(PEG, structure seen in fig. 2.8) is a hydrophilic, non-ionic and well-characterized polymer. It is widely used in pharmaceutical industry as a stealth coating (from the detection by the human immune system) for drug delivery vehicles due to its potent biomolecule antifouling properties [114–118]. It is also known to be used for colloidal particle stabilization, because of generated steric repulsion between the polymer chains [119]. However, there have been contradicting discussions on interaction between PEG and various proteins. Some studies report PEG to

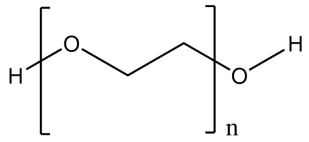

Figure 2.8: Structure of hydrophilic polymer poly(ethylene glycol).

be resistant to proteins on many occasions [118, 120–127]. In fact, Gon *et al*. reported that while PLL(poly(L-lysine)-PEG copolymer tethered to a silica surface repels bigger proteins such as fibrinogen and albumin, an interaction with a small protein lysozyme (LYZ; molecular weight ~14.3 kDa) is observed with increasing PEG amount inside the copolymer brush [122]. The interaction between LYZ and PEG has been postulated to be due to the weak affinity of protein towards the polymer, arising from hydrogen bonding, but is still not clearly understood [121]. Controversely, Ngadi *et al*. have demonstrated in-situ QCM-D experiments, where much less of LYZ mass was adsorbed on PEG functionalized stainless-steel surface compared to the mass of a bigger β-casein protein [128]. Moreover, Furness *et al*. has shown a significantly large dissociation constant of 76 mM at pH 4.0 by nuclear magnetic resonance (NMR) measurements and suggested that hydrophobic interactions are behind this interaction [124]. On the other hand, Wu *et al*. determined substantially higher affinities (dissociation constant in μM region), but also shown similar or even higher BSA protein binding to PEG [129]. The affinity between LYZ and PEG interaction seem to be dependent on polymer molecular weight as well [130].

Most studies argue that the resistance to protein adsorption on PEG and other polymers is mainly promoted by the polymer brush grafting density and polymer chain hydration [131–135]. For example, one comparative study between ethylene oxide (EO) self-assembled monolayers (SAMs) on Au and Ag showed that if the grafting density of the SAM is too high, fibrinogen will adsorb on the surface [136]. Additionally, an alternative reason for the adsorption of proteins, is that the EO layer is too tightly packed to maintain a hydrated shell. All in all, even though some possible explanations exist, there is still a lack of understanding of weak PEG-protein interactions and especially the techniques, which can monitor them accurately.

2.1.6 Thermo-responsive polymer poly(*N*-isopropylacrylamide) (PNIPAM)

Stimuli-responsive polymers have gained significant interest in the last decades. The main reason is that when an external stimulus, e.g. pH [137], temperature [138], mechanical force [139], electric/-magnetic fields [140, 141], etc., is provided, such polymers may change their chemical and physical properties [142, 143]. Thus, the applications span from biosensors [144], drug delivery [145], coatings with self-healing capability [146, 147] to materials for cell cultures [148].

In this thesis, poly(*N*-isopropylacrylamide)(PNIPAM; fig. 1.4) has been selected as a stimuli-responsive polymer as a potential candidate acting as a "smart gate" for protein transport. The temperature-responsive polymer has been studied for around 70 years now since it's first synthesis by Specht *et al*. [149]. In short, PNIPAM polymer chains contract from a coil to a globule shape when local temperature of 32 °C (in water) is reached. This temperature is known as a lower critical solution temperature (LCST) of a polymer, which leads to expulsion of up to 80% of water surrounding the chain [150, 151]. This is because at this temperature PNIPAM chains favor polymer-polymer (e.g. hydrophobic interaction between methyl functional groups) instead of solvent-polymer interaction more. The relatively low LCST paves way for PNIPAM polymers to be used in biotechnological applications, which include cells [152, 153] and proteins [89, 150].

In order to consider using PNIPAM polymer brushes as a possible entropic barrier for protein transport, it is important to review possible fouling or adsorption types of proteins on polymer functionalized surfaces. Proteins adsorb differently on polymer brushes depending on their degree of hydration, protein dimensions, protein-surface interaction, polymer molecular weight and grafting density Γ ($= 1/d^2$) [89, 132]. The degree of hydration is related to the osmotic pressure present in the brushes, which, in turn, can prevent proteins from penetrating into the layer [132]. In addition, higher Γ leads to higher osmotic pressure as well. However, the latter can be reduced if a poor solvent for a specific polymer is chosen [89, 154].

There are 3 suggested protein adsorption possibilities - primary, ternary and secondary - as illustrated by figure 2.9. Primary and ternary protein adsorption happens, when the radius of the protein is much smaller than the distance between polymer chain grafting sites d [89]. In such example, the protein freely penetrates the brush and possibly adsorbs on the substrate, lying underneath the film. The adsorbed protein amount depends on the affinity between the substrate and the protein, and on polymer properties. If the protein of interest is small enough to go through the brush, but not enough to reach the graft surface, such adsorption is known as ternary [155, 156]. However, when the protein dimensions are too big for it to penetrate the brush, it may adsorb on the outer edge of the film. This can be explained by protein-polymer interactions or long-distance attraction with the functionalized surface.

These adsorption modes give some insight in designing polymer brush films (e.g. by controlling Γ) for different types of proteins. Yet the knowledge about the driving force of the reversible interaction, which is sometimes observed between certain polymers and proteins (e.g. between PNIPAM functionalized surfaces and bovine

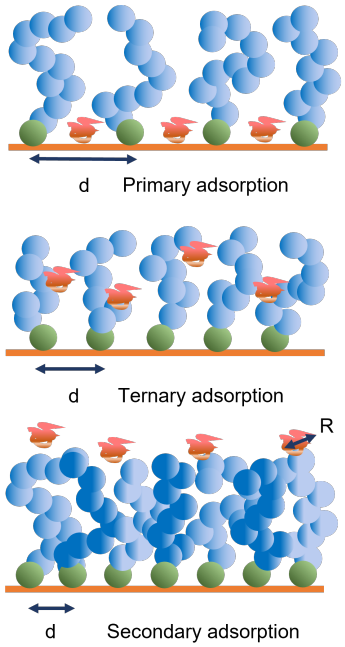

Figure 2.9: Different modes of protein adsorption on polymer brush film depending on chain to chain distance d.

serum albumin), is still lacking [89]. Also, it was seen that proteins can stay adsorbed for many hours (e.g. 6-72 hours) [150] as a possible result of steric exclusion [157], protein-polymer hydrogen bonding [150], protein denaturation [158] or surface topography [159].

2.1.7 The co-nonsolvency effect

Choosing the right type of solvent for polymerization can be challenging in some cases. For example, if a poor solvent (e.g., water and methanol) is used to solvate PNIPAM polymers, the solution can turn turbid [160]. This is known as the co-nonsolvency effect, as explained by Schild *et al*. in 1991. However, when PNIPAM is dissolved in methanol or water separately, the solution is transparent, indicating that the solvent is good. As previously mentioned in subsection 2.1.3, the type of solvent plays a huge role on polymer brush conformation. Therefore, if a good solvent is chosen, the chains will extend into the solution from the graft surface. Otherwise, the polymer chains may be in collapsed, partly collapsed or extended state [160–162]. The most probable explanations for this effect arise from altered hydrophobic functional group hydration [163], cooperative interaction of methanol and water mixture with the polymer segments [164–166] and possible bridges between isopropyl functional groups of PNIPAM generated by methanol [167].

Previously (in subsection 2.1.4), it was mentioned that the solvent composition in ARGET-ATRP reactions is highly significant as it influences how fast the polymers grow. The molar fraction X of a solvent in a two solvent component system, has to be fixed in order to achieve optimized polymer growth conditions [168]. Some researchers suggest that in the case of water and methanol mixtures for relatively controlled PNIPAM polymer brush polymerization, ~0.25 methanol molar fraction should be used [112] while others vouch for a range of 0.16-0.31 [168]. Nevertheless, some reports underline the unevenness of water/methanol distribution around grafted PNIPAM chains in comparison to when they are in solution [169–171]. This happens at almost exactly within the previously mentioned molar fraction region (e.g. $X_{Methanol}$ = 0.17 - 0.5) and is explained by possible water/methanol complexation arising from hydrogen bonding. In contrast, others propose that below 0.13 or above 0.4 $X_{Methanol}$ should be used, as in these regions PNIPAM is most soluble [163].

To sum up, optimizing ARGET-ATRP polymerization conditions for PNIPAM polymer brushes in binary solvent mixtures is still not straightforward as the co-nonsolvency effect might be prominent in a lot of cases. If one would choose to polymerize using a single

solvent, then the reaction kinetics might be uncontrollably fast or considerably slow [168]. Nonetheless, the co-nonsolvency effect is known to be utilized in a variety of applications: tuneable friction of PNIPAM coatings [161], determining the enantiomeric excess of some chiral molecules [172] and adhesion of nanoparticles [173].

2.2 Interaction forces

There are two major long-range forces existing among two macromolecules or surfaces in aqueous solutions [174]. The first is the repulsive "double-layer" (DL) force, which as well as the attractive Van der Waals (VDW) force has been described during the second world war by Derjaguin and Landau (1941) and their work was further expanded by Verwey with Overbeek later on (1948) [174–176]. Usually, they occur together at the same time. However, while VDW force is always present, the DL force requires charges.

It is important to mention, that the continuum models such as described by Lifshitz for VDW forces or Poisson-Boltzmann equation for electrostatic interactions cannot be applied at small separation distances (~1 nm) anymore. This is because other dominating forces take place, but they will not be discussed any further.

In the framework of interactions involving proteins, there are secondary factors, influencing how they fold, as well. However, only VDW, DL, hydrophobic interaction and hydrogen bonding will be briefly discussed [177–179].

2.2.1 Electrostatic interactions (DLVO theory)

The long-range electrostatic interaction potential *U(D)* is known as exponentially decaying function between two similarly charged molecules/surfaces (expressed by eq. 2.15) [174]. It is repulsive for same charged surfaces and found at a specific separation distance D.

$$U(D) \approx +C_{ES} e^{-\kappa D} \tag{2.15}$$

here C_{ES} (units in V) is a constant, which is influenced by the morphology of the interacting surfaces, surface charge density and solution conditions. Parameter κ^{-1} (calculated by eq. 2.17) is the Debye length, indicating the decay length of the interaction (i.e. diminishes with increasing salt concentration or the valence of ions). There are many ways to approximate C_{ES}, some of which include the surface charge density or surface potential ψ_0. The latter term has contributions from bound surface charges and ions

in the diffuse layer or the slipping plane (ψ_ζ) as depicted in fig. 2.10 [180]. Furthermore, sometimes, C_{ES} is calculated by assuming that neither the surface charge density nor the surface potential ψ_0 are constant (e.g. 'charge-regulation' effects) [174].

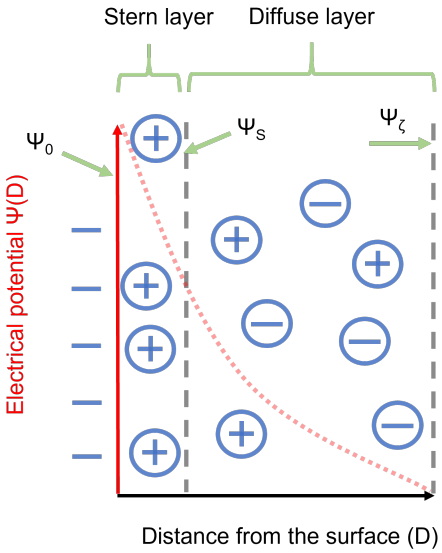

Figure 2.10: Electric potential as a function of distance from the surface (double layer). The circles denote opposite charge ions, residing either in Stern or diffuse layer on a particle of interest. ψ_S is the Stern potential. [181]

If a macromolecule of a radius R is close to a flat surface (i.e. $D \ll R$), the electrostatic interaction energy can be expressed as:

$$E(D) = RZe^{-\kappa D} \tag{2.16}$$

where Z is a constant proportional to surface potential ψ_0 (analogous to Hamaker constant in Van der Waals force). Moreover, κ can be estimated by

$$\kappa = \left(\frac{2e^2 z^2}{\epsilon_0 \epsilon k_B T} C_{el} \right)^{1/2} \tag{2.17}$$

here C_{el} is the concentration of the electrolyte, z is number of salt ion charges, ϵ is dielectric permittivity of the solvent and ϵ_0 - dielectric constant of vacuum [182].

In the case of two macromolecules of radii R_1 and R_2 interacting with each other (in this case D is much smaller than R_1 and R_2 as well), the interaction energy becomes:

$$E(D) = \left(\frac{R_1 R_2}{R_1 + R_2} \right) Ze^{-\kappa D} \tag{2.18}$$

2.2.2 Van der Waals (VDW)

The net interaction curve (involving VDW and DL forces) as a function of separation distance between two surfaces with high surface charge density is illustrated in fig. 2.11.

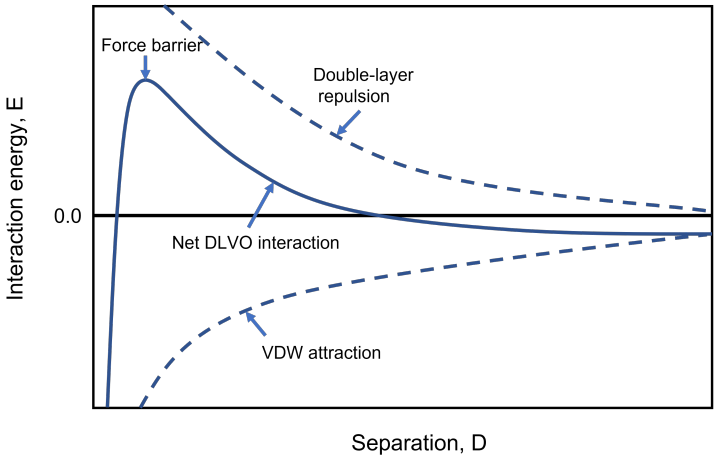

Figure 2.11: An illustration of DLVO interaction energy E as a function of separation distance D between two charged surfaces. Dashed lines represent Double-layer repulsion and Van der Waals force, and the solid line shows a total interaction potential of both forces at high surface charge density.

VDW forces arise from the variations in the molecule electric dipole moments when they come close. In the case of an attraction between two atoms (can be repulsive in some other cases), which scales with separation distance D, the interaction energy can be shown as:

$$E(D) = \frac{-C_{VDW}}{D^6} \tag{2.19}$$

here, C_{VDW} is influenced by the geometry and optical characteristics of the interacting objects.

On the macroscopic scale, VDW force is explained by taking into account the Hamaker constant A. The parameter can be calculated by the 'Lifshitz theory' (eq. 2.20).

$$A = \frac{3}{4} k_B T \left(\frac{\epsilon_1 - \epsilon_2}{\epsilon_1 + \epsilon_2}\right)^2 + \frac{3I}{16\sqrt{2}} \frac{(n_1^2 - n_2^2)^2}{(n_1^2 + n_2^2)^{\frac{3}{2}}} \tag{2.20}$$

here, ϵ_1, ϵ_2 and n_1, n_2 are the dielectric constants and refractive indexes of the two materials, and I is their ionization potential (roughly on the order of $k_B T$ [183–186]). Even though the model was created for continuous materials (no defined structure), it seems to apply for small particles and molecules when in contact as well. Therefore, the adhesion force and binding energies of a vesicle or a protein are calculated to compare to the thermal energy $k_B T$, which dictates how long a molecule is adhered on a flat surface (in water) [174].

For the two cases, where a sphere with a radius R is near a flat surface (e.g. $R \gg D$) and two spheres with radii R_1 and R_2 are at separation D, VDW interaction energy (with the Hamaker constant) can be calculated with equations 2.21 and 2.22, accordingly.

$$E(D) = \frac{-AR}{6D} \tag{2.21}$$

$$E(D) = \frac{-A}{6D}\frac{R_1 R_2}{R_1 + R_2} \tag{2.22}$$

here the negative signs in front of equations represent the attractive force.

Overall, VDW forces are highly dictated by the cut-off separation D (e.g. stronger at small distances), which is determined by experiments on crystals [187, 188]. However, when two biological molecules come in contact, it becomes more difficult to estimate as other repulsive forces often come into play. Additional forces arise from molecule hydration shells, which are strongly bound around them, thermal fluctuations and steric hindrance due to dynamic nature of the biomolecules (i.e. intrinsic disorder as mentioned previously in Chapter 1). For example, these could possibly prevent two proteins from coming as close as 0.5 - 2 nm towards each other and significantly diminish the possibility for adhesion/binding [174].

2.2.3 Hydrophobic interaction

A hydrophobic surface or a surface containing hydrophobic patches is such that is inert to water (i.e. cannot bind to water via ionic or hydrogen bonding). Some direct measurements have resolved that the hydrophobic interaction, arising from non-polar molecules or surfaces, is much higher than the theoretically estimated VDW force (e.g. between hydrocarbon functionalized surfaces). Also, it is long-ranged and an attractive force [174, 189, 190]. The extent of this force depends on surface 'hydrophobicity' or diminishing 'hydrophilicity' (i.e. self-interactions of water molecules are dominating compared to interactions with water and the surface of interest), which can be measured by contact angle measurements. The higher the contact angle θ, the more hydrophobic the surface is (e.g. contact angles of 100 - 115°are considered strongly hydrophobic).

The origin of hydrophobic interaction remains undetermined still and the extent of it has mainly been studied in macroscopic scales [174]. Nevertheless, it is well established, that at small separations (<10 nm) the hydrophobic interaction is not influenced by the

type and concentration of electrolyte or not significantly at least. However, at larger spacings (>20 nm), some studies indicate that electrolyte dependence is observable (e.g. for divalent ions) [191, 192].

There is no question of hydrophobic interaction importance for biological environments. For example, the fundamental nature of how proteins assemble in solution is that their hydrophobic moieties are hidden inside a core, resulting in a folding event [178, 193, 194]. If, in certain conditions, proteins expose their hydrophobic core to surfaces and adsorb, they might be subject to denaturation or unfolding, possibly inhibiting their function permanently [195–198]. Some hydrophobic amino acid functional groups in proteins, are not completely hidden inside, so can be a driving force for protein-surface interaction [196, 197]. Therefore, one of possible solutions to avoid irreversible protein adsorption and unfolding, is to manufacture antifouling surfaces, which act as good entropic barriers.

2.2.4 Hydrogen bonding

Hydrogen bonding (e.g. between backbone amide functional groups in the amino acids) is known to be one of the main reasons why proteins fold [177, 178, 199, 200]. The bond constitutes a proton within a donor group with a partial positive charge, which interacts with an acceptor atom or its electron density (fig. 2.12). The strength of protein hydrogen bonds highly depends on competitive interactions with water molecules, which act as alternative binding partners for hydrogen bonding moieties. Even though plenty of arguments still exist on this competition, it is also possible that water prefers to hydrogen bond to itself rather than solute molecules [200, 201]. Also, 'buried water' molecules, which occupy small spaces within proteins, make a significant impact on their structure [200]. Nevertheless, it is known that proteins establish ~1.1 hydrogen bonds per functional group (e.g. amide) within themselves [202]. Moreover, ~31% of polar sidechains, residing at protein's surface, hydrogen bond strictly with water. This is comparable to polypeptide backbone carbonyl and amine groups not hydrogen bonding to other protein atoms (e.g. ~30-40% for myoglobin and erythrocruorin) [200].

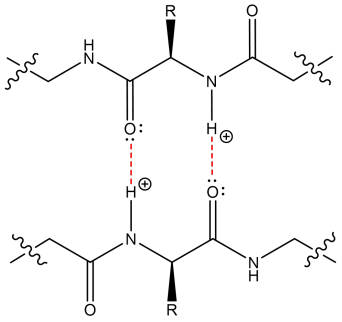

Hydrogen bonding

Figure 2.12: An illustration of hydrogen bonding between a proton with a partial positive charge and an electron rich oxygen for two amino acids.

To generate a hydrogen bond during the folding of a protein, a high number of polar moieties become dehydrated fully or to a certain extent. However, there is a trade-off as proteins gain stability from the new formulation, but at the same time lose it from hiding the polar moieties within the core [201]. Therefore, the whole process of protein structure establishment is an interplay of water-water,

water-amino acid, amino acid - amino acid hydrogen bonding and hydrophobic interaction.

2.3 Surface plasmon resonance (SPR)

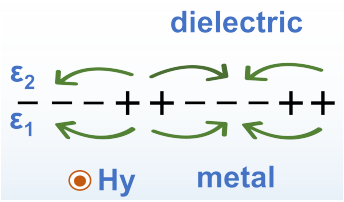

Figure 2.13: Charge fluctuations on the metal/dielectric (with dielectric permittivity constants ϵ_1 and ϵ_2, respectively) interface. H_y shows in which direction the magnetic field is facing (y axis or 'in the surface plane').

Surface plasmon oscillations take place when localized electron charges on the metal surface start moving coherently (as seen in fig. 2.13) [203]. These longitudinal oscillations can be expressed by a dispersion relation ωk_x (ω is their frequency and k_x is the propagating wave's vector; also further developed in eq. 2.24). Ritchie talked about these waves first in 1957 [204] and the experimental proof by Powell and Swan followed soon after [205]. Later, Otto [206] and Kretschmann [207] proposed a possibility to excite surface plasmons (SPs) by attenuated total reflection (ATR). Further on, SPs gained significant attention by many research groups and today the ever increasing application span for surface plasmon resonance (SPR) is vividly huge [203, 208–214]. The main aim of SPR technique is to monitor local deviations in bulk and surface refractive indexes due to addition of molecules/films/solvents. Consequently, by doing this, it is possible to follow molecule binding/desorption events with a sensitivity of ~0.01 pg · mm^{-2} for proteins [215].

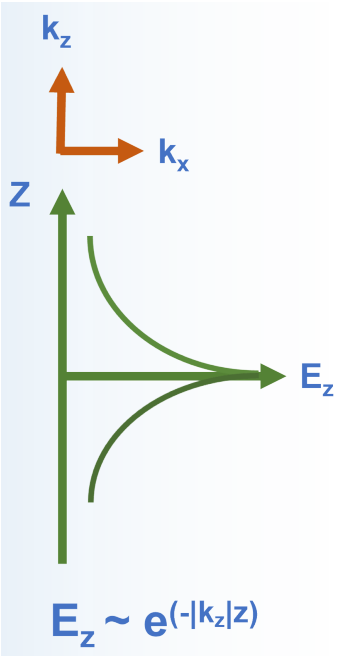

Figure 2.14: Eletrical field exponential decay of SPs in the direction of z.

SPs may be localized in z direction, which spans up to 1 Å(also known as Thomas-Fermi screening length). Furthermore, the transversal and longitudinal electromagnetic field E (together with this fluctuating electron cloud) on the metal surface is at its maximum when z is zero and completely decays when $|z|$ reaches infinity (as seen in eq. 2.23 and fig. 2.14). This is why the electromagnetic field and charge fluctuations on the metal boundary can be used to track changes on the surface. [203]

$$E = E_0^{\pm} \exp[+i(k_x x \pm k_z z - \omega t)] \tag{2.23}$$

here, E_0 is incident electric field, "+" is when $z \geq 0$ and "-" when $z \leq 0$, and k_z is the electromagnetic field vector, indicating the direction of E_z decay. Moreover, the wave vector k_x is facing in the same direction as x axis and is equivalent to $2\pi/\lambda_p$ (λ_p is the wavelength of SPs). If a certain medium is taken into respect, k becomes $\omega n/c$, where n is the refractive index of the medium. Furthermore, if the imaginary part is not considered in the wave vector (such as $k = Re(k) + iIm(k)$), it would propagate forever.

Dispersion relations can be simplified through Maxwell's equations (eq. 2.25 and 2.26):

$$k_x = \frac{\omega}{c}\left(\frac{\epsilon_1\epsilon_2}{\epsilon_1+\epsilon_2}\right)^{1/2} \tag{2.24}$$

$$\frac{k_{z1}}{\epsilon_1} + \frac{k_{z2}}{\epsilon_2} = 0 \tag{2.25}$$

$$\epsilon_i\left(\frac{\omega}{c}\right)^2 = k_x^2 + k_{zi}^2 \tag{2.26}$$

In this case, we can consider a semi-infinite metal of planar geometry with the following dielectric function $\epsilon_1 = \epsilon_1^{'} + i\epsilon_1^{''}$ ($\epsilon_1^{'}$ and $\epsilon_1^{''}$ are the real and imaginary parts of the function) parallel to a vacuum or air (ϵ_2).

SPs cannot be excited directly as there is a lack of energy and momentum of incident light. When k_x is small, the dispersion relation comes close to the incoming light (i.e. $\sqrt{\epsilon_2}\omega/c$), but still larger, thus, the SPs cannot turn into "radiative" light [203, 214]. To put it in another way, photons can be turned into SPs only when $\hbar\omega/c$ (or the wave vector) of the incident light is increased by Δk_x to match the dispersion relation of longitudinal oscillations on the metal surface [203]. This lack of momentum and energy can be compensated by coupling the metal with a higher dielectric constant material such as an optical prism or a waveguide [213]. Then, ω can be shown as:

$$\omega_{sp} = \frac{\omega_p}{\sqrt{1+\epsilon_2}} \tag{2.27}$$

here k_x is large or $\epsilon_1' \rightarrow$ - ϵ_2, and ω_p is the plasma (i.e. bulk metal) frequency (which is equal to $\sqrt{4\pi ne^2/m^*}$, where n is the bulk electron density and m^* is the effective mass, accordingly [216]).

In our experiments an SPR instrument with a prism coupler was used, therefore in the following subsection attenuated total reflection (ATR) will be briefly overviewed.

2.3.1 Excitation of Surface Plasmons by Attenuated Total Reflection (ATR) coupling

In order to meet the excitation requirement for the surface plasmons, a material with a higher dielectric constant than 1 (in the case that the medium at the surface is air) has to be coupled to the metal layer. In this case, the projection of light on the interface can be written as:

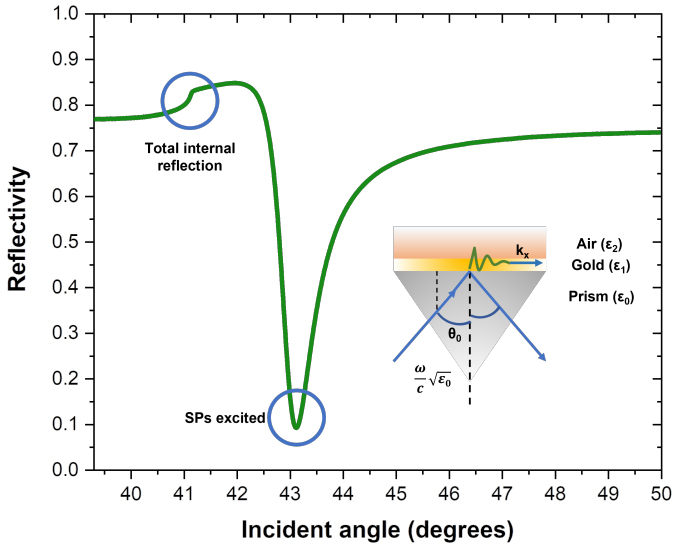

Figure 2.15: SPR angular spectrum in air (Kretschmann-Raether configuration). SPs are excited at an angle of ~43 degrees and TIR occurs at ~41 degrees angle.

$$k_x = \sqrt{\epsilon_0}\frac{\omega}{c}\sin(\theta_0) \tag{2.28}$$

here, ϵ_0 is the dielectric permittivity of the dielectric material (e.g. prism; not to be confused with denotation for dielectric permittivity of vacuum) and θ_0 is the incident light angle. The consequent excitation of coherent charge fluctuations is observed as a dip in a reflectivity spectrum in SPR software when an angular scan is taken (fig. 2.15). Therefore, the angle, at which SPs are excited, is considered as the SPR angle. This kind of setup is referred as the Kretschmann-Raether configuration [207].

In figure 2.15, a total internal reflection (TIR) event is shown, which is evident when light with a momentum $\omega/c\ \sqrt{\epsilon_0}$ goes through a dielectric material with a larger refractive index n_1 than the adjacent metal layer refractive index n_2. When the incident angle is higher than θ_c (as seen in equation 2.29), the light is completely reflected from the metal [209].

$$\theta_c = \arcsin\left(\frac{n_2}{n_1}\right) \tag{2.29}$$

Moreover, the light can also be refracted through the interface of two different media and in this situation, the refracted and incident angles can be related through Snell's law:

$$n_1\sin(\theta_i) = n_2\sin(\theta_t) \tag{2.30}$$

TIR and SPR angle shifts in the angular spectrum (fig. 2.15) refer to the refractive index changes either in the bulk (e.g. air or solution) or on the metal surface, accordingly.

In SPR, angular response R (from eq. 2.31) shifts when there are local changes in bulk or surface refractive index [217]. This allows to determine if a binding event occurs within or on the sensor coated film.

$$R = S(n_f - n_b)(1 - \exp(-2d/\delta)) \tag{2.31}$$

here, S is SPR response sensitivity, n_f and n_b are coated film's and bulk solution refractive indexes, d is adsorbed layer's thickness, and δ is the evanescent field length. Eq. 2.31 can only be applied when these two refractive indexes do not significantly differ from each other [212, 218]. In addition, this estimation can be used to determine decay length, for example, by coating the dielectric with thicker and thicker metal, and applying the transfer matrix, described later in the thesis.

A possible alternative for the previously suggested approach are the *Fresnel coefficients*, which quantitatively describe the dip in ATR minimum for a single or a few interfaces. These will be discussed in the next subsection.

2.3.2 Fresnel coefficients and modelling

Fresnel models are used to evaluate the amount of transmitted or reflected light (in relative intensities) for single or multiple interfaces. Four Fresnel coefficients exist and each represent s and p polarization as well as transmitted and reflected light. The numerical range is between 0 and 1. P-polarization is particularly interesting for SPR as one of the electrical field terms is facing perpendicular to the surface (E_z; fig. 2.14). In addition, by estimating the bulk and film refractive indexes with Snell's law (eq. 2.30), transmission and reflection Fresnel coefficients for p-polarized light and a single interface can be calculated with these equations [209]:

$$F_{rp} = \frac{n_1\sqrt{1 - \left[\frac{n_1}{n_2}\sin(\theta_i)\right]^2} - n_2\cos(\theta_i)}{n_1\sqrt{1 - \left[\frac{n_1}{n_2}\sin(\theta_i)\right]^2} + n_2\cos(\theta_i)} \tag{2.32}$$

$$F_{tp} = \frac{2n_1\cos(\theta_i)}{n_2\cos(\theta_i) + n_1\sqrt{1 - \left[\frac{n_1}{n_2}\sin(\theta_i)\right]^2}} \tag{2.33}$$

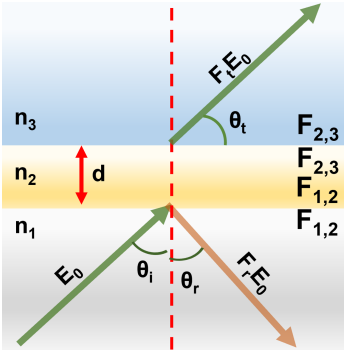

Figure 2.16: A representation of transmitted and reflected light paths in the case when the coherence length of incident light is bigger than layer thickness d.

When a two interface system is considered (e.g. prism (1), metal (2) and air (3), upon illumination, the resulting reflected light brings a phase shift in accordance to the incident light (as seen in fig. 2.16). This happens when the width of light and its coherence length is bigger than metal thickness d. Moreover, because the light is coherent, the interference component has to be included in the Fresnel coefficient calculations (as described in eq. 2.34 and eq. 2.35) [209].

$$F_r = \frac{F_{r,12} + F_{r,23} e^{i2k_0 d n_2 \cos(\theta_2)}}{1 + F_{r,12} F_{r,23} e^{i2k_0 d n_2 \cos(\theta_2)}} \tag{2.34}$$

$$F_t = \frac{F_{t,12} + F_{t,23} e^{ik_0 d n_2 \cos(\theta_2)}}{1 + F_{r,12} F_{r,23} e^{i2k_0 d n_2 \cos(\theta_2)}} \tag{2.35}$$

In eq. 2.34 and eq. 2.35, k_0 is the wave vector, which is equal to $2\pi/\lambda_0$. The new transmitted light angle, due to phase shift, can be evaluated with the following equation:

$$\begin{aligned} \theta_{j+1} = \mathrm{Re}\left(\arcsin\left(\frac{n_j}{n_{j+1}}\sin(\theta_j)\right)\right) \\ - i\left|\mathrm{Im}\left(\arcsin\left(\frac{n_j}{n_{j+1}}\sin(\theta_j)\right)\right)\right| \end{aligned} \tag{2.36}$$

Here, j is the number of materials. The new transmission angle estimation comes as a continuation from the Snell's law (eq. 2.30) and is used to model several interface systems [209]. In addition, the eq. 2.36 may be applied for multilayer systems as a negative imaginary part is ensured for each angle (requirement to implement Fresnel models in the computer software).

In SPR experiments, planar sensors contain more than one interface (e.g. Cr as an adhesion layer between silica and gold), so the common alternative to avoid previously mentioned issue is the *matrix transfer* analytical approach (eq. 2.37) [90, 112, 113, 219].

$$\begin{aligned} \Phi = \prod_{j=2}^{m-1} \left(\frac{1}{F_{t,[j-1]j}} \begin{bmatrix} 1 & F_{r,[j-1]j} \\ F_{r,[j-1]j} & 1 \end{bmatrix} \right. \\ \left. \times \begin{bmatrix} e^{-ik_0 d_j n_j \cos(\theta_j)} & 0 \\ 0 & e^{-ik_0 d_j n_j \cos(\theta_j)} \end{bmatrix} \right) \\ \times \frac{1}{F_{t,[m-1]m}} \begin{bmatrix} 1 & F_{r,[m-1]m} \\ F_{r,[m-1]m} & 1 \end{bmatrix} \end{aligned} \tag{2.37}$$

here m is a number of materials of interest ($m-1$ is a number of interfaces and $m-2$ number of films). The matrices are multiplied with each other until the last matrix is obtained (i.e. the last interface between medium $m-1$ and m). However, eq. 2.37 does not include the backwards reflected light term (i.e. at the last layer there is no more reflection). The final estimations for reflection and transmission Fresnel coefficients of the whole system can be deducted from the parameters in Φ (i.e. from this last 2x2 matrix) [209]:

$$F_{rp} = \frac{\Phi(2,1)}{\Phi(1,1)} \tag{2.38}$$

$$F_{tp} = \frac{1}{\Phi(1,1)} \tag{2.39}$$

It is important to mention, that the transfer matrix takes into account transmission and reflection intensities through/from individual boundaries (generated from equations 2.40 and 2.41), and is used to directly model SPR spectra.

$$F_R = |F_r|^2 \tag{2.40}$$

$$F_T = \frac{Re\left(n_2\sqrt{1-\left[\frac{n_1}{n_2}sin(\theta_i)\right]^2}\right)}{Re(n_1 cos(\theta_i))}|F_t|^2 \tag{2.41}$$

here the capital letters in the Fresnel coefficient indexes mark the reflection and transmission of intensity I instead of electric field amplitude, which was described before.

2.3.3 Non-interacting molecules method for polymer brush height determination

The non-interacting probe technique was first proposed by Schoch *et al*. [218] and further developed by Emilsson *et al*. [112]. Together with Fresnel models, this method can be used to determine polymer film heights in dry and solvated forms (i.e. exclusion height, where probe molecules cannot penetrate anymore). However, determining the wet thickness of polymer brush films solely with Fresnel models has been an issue beforehand. This is because polymer-solvent interactions complicate the resulting refractive index of the swollen film (i.e. refractive index and film thickness cannot be separated in the fitting) [220, 221]. In addition, one would have

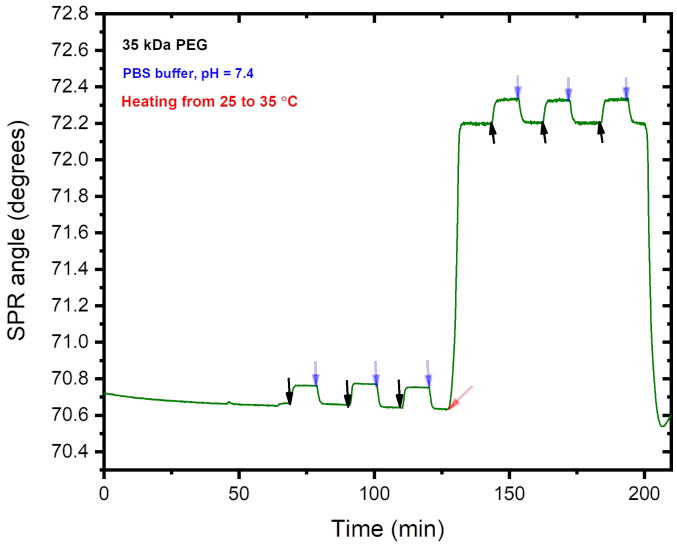

Figure 2.17: An SPR sensogram is shown, where 35 kDa PEG is injected over PNIPAM polymer brushes (below and above LCST) in phosphate buffer saline buffer (PBS, pH = 7.4). 670 nm laser illumination is used for this experiment.

to determine either the wet thickness of the layer or its refractive index independently (from eq. 2.31).

In practice, the non-interactive probe method includes injection of molecules, which do not interact with the layer of interest (as seen in fig. 2.17 with injections of poly(ethylene glycol)(PEG). Figure 2.17 shows that upon rinsing with running buffer after each injection, SPR angle shift comes back to the baseline value. This indicates no irreversible binding between PEG and PNIPAM polymer brush layer. Moreover, it is possible to qualitatively track if there is no interaction between the film of interest and injected molecules by plotting SPR angle shift as a function of TIR angle shift (fig. 2.18) for a particular injection. If a linear correlation is observed, then there is a good indication that no interaction between film and probes is evident. On the other hand, if a wide hysteresis is achieved, then both are reversibly interacting and an alternative to the injected molecules has to be found.

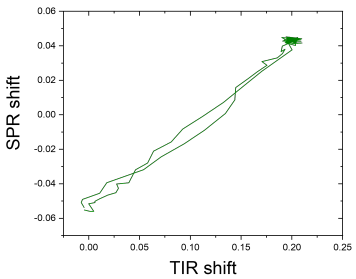

Figure 2.18: SPR angle shift as a function of TIR angle shift for the injection of non-interacting 35 kDa PEG over PNIPAM polymer brush film at 25 °C is shown.

After running the non-interactive probe injections, the refractive index of the solvated film with and without the non-interacting molecules was calculated according to Snell's law (eq. 2.30). Then, the SPR angular spectra (i.e. for both cases) was fitted with full Fresnel models over a variety of refractive indexes and heights [90, 112, 113]. The bulk refractive index was determined from the shift in TIR angle upon injecting molecules.

Finally, when the fitted values (i.e. with and without probe molecules) of the wet thickness against the refractive index are plotted, a unique intersect is achieved. This pair represents the exclusion height d of the coating and its refractive index n (as shown in the case with PNIPAM film and PEG in fig. 2.19).

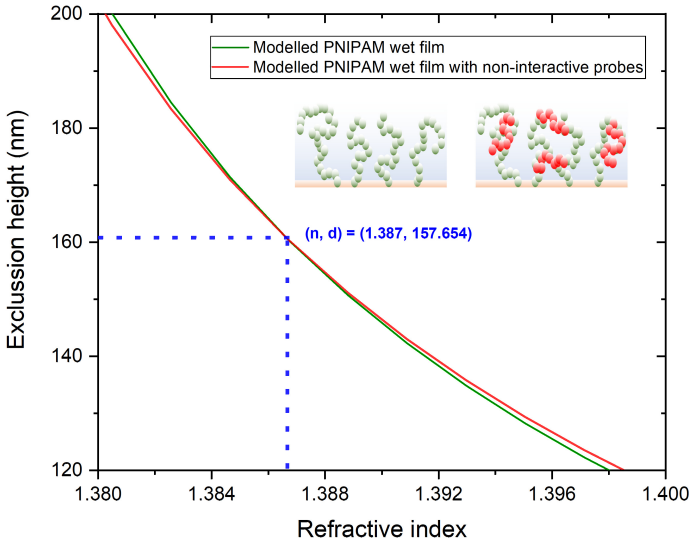

Figure 2.19: Swollen PNIPAM film and non-interactive 35 kDa PEG solution fits over a variety of thicknesses and refractive indexes. A unique pair of n and d is generated, which represents the refractive index and exclusion height of hydrated PNIPAM polymer brushes, respectively.

2.3.4 "Bulk effect" contribution in SPR sensograms

One of the main issues found in SPR, is the “bulk refractive index (RI) effect” contribution [222]. Generally speaking, the “bulk RI effect” comes from the fact that SPR evanescent field sensing range is greater (i.e. hundreds of nm) than most of the sensor adhered film thicknesses (e.g. ~2 - 10 nm for proteins), thus, the changes in both surface and bulk solution RI will be detected [223]. This means that even if the molecules in the bulk solution are not adsorbing on the surface, they will contribute to the SPR angle shift as well (especially important when high concentrations of analytes are used). Such contribution is detrimental for monitoring, e.g. weak interactions or complex samples, or anything else that comes with a big change in bulk refractive index. This is because it gives a significant false error in bulk refractive index and is difficult to distinguish from the "real" signal coming from the surface adsorption alone.

A previously proposed way of possibly solving this problem is to use two (or more) separated sensor channels, where one part of the sensor is functionalized and the other is used as a reference (i.e. not functionalized) [224]. However, it cannot be guaranteed, that the reference channel is perfectly antifouling for the injected molecules and that the layer thicknesses on both channels are equal. Another method, as suggested by Chinowsky *et al.*, is to separate the surface RI from the bulk RI, which is done by employing a specifically designed analyte handling apparatus, calibration procedure and linear data analysis [223]. The work correctly shows the significance of using the TIR angle to retrieve the bulk RI.

However, the major drawbacks of this method are: the design of such a system is complex, a reference channel is needed, and the technique is limited to thick layers or analytes, which do not reach chemical/physical saturation/equilibrium on the surface.

In the Result and Discussion subsection 4.2, a correct analytical approach to remove the "bulk effect" contribution from the SPR angle shift, which avoids all of these issues, will be presented in detail.

2.3.5 Plasmonic nanostructured surfaces

Nanowells, which are functionalized with PNIPAM polymer brushes, can be used as a foundation for building a sensing device for biomolecules. This device is based on the surface plasmon grating coupling mechanism, which was reported earlier by Raether and Junesch *et al.* [203, 225]. Surface plasmon effect, in this case, is either localized in individual nanowells or the whole periodic array, where distances between nanopores reach up to ~300 nm [211, 226, 227]. The condition to excite surface plasmons (here light of incidence is perpendicular to the surface) for an array can be shown as:

$$Re(k_x) = ksin(\Theta) \pm j\frac{2\pi}{P} \tag{2.42}$$

where k is the photon wave vector, $sin(\Theta)$ is the incident angle to the surface normal, j is a positive integer, describing diffraction order of the grating, and P is a characteristic spacing between the nanowells (i.e. periodicity).

2.4 Extinction Spectroscopy

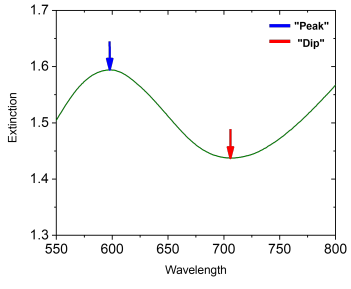

Figure 2.20: Asymmetric "Peak" and "Dip" seen in extinction spectra.

Optical extinction spectrum is often described by a graph, where transmittance of a sample of interest is plotted against the wavelength of incident light [228–230]. In our experiments, we define extinction $E(\lambda)$ as a sum of absorption and scattering, which happens when incident light comes into contact with nanowells (calculated by eq. 2.43). This seems to be typical for small apertures in periodic distances for thin gold films (e.g. smaller than used colloid radius) and results in an asymmetric resonance shown as maximum and minimum in the spectra ("Peak" and "Dip", respectively; fig. 2.20) [56, 210, 231].

$$E(\lambda) = -log_{10}\left(\frac{I_{sample}(\lambda) - I_{dark}(\lambda)}{I_{ref}(\lambda) - I_{dark}(\lambda)}\right) \tag{2.43}$$

here, $I_{sample}(\lambda)$ is the spectrum of a sample surface, $I_{dark}(\lambda)$ is non-illuminated surface spectrum and $I_{ref}(\lambda)$ is a spectrum of a reference without any nanowells.

The resonance centroid (i.e. center of mass) positions of maximum and minimum from the extinction spectra can be monitored for biomolecule adsorption/desorption events (i.e. as red or blue shifts in the spectra) as described before [209, 232]. The "Peak" is more sensitive to the planar surface refractive index changes as it is Bloch wave coupled to the propagating plasmons in the film (i.e. charge fluctuations are symmetrically distributed on both sides of gold layer). In addition, the wavelength of this surface sensitive asymmetric mode is influenced by the characteristic periodic distances between the nanowells and the thickness of the metal layer, but not the nanostructure diameter [210]. Moreover, the plasmonic field of "Peak" extends to ~50 nm from the gold layer [233]. On the other hand, the "Dip" resonance exhibits field enhancement towards the interior of the nanowells (fig. 2.21) [211, 225, 231, 232]. The extinction minimum can be seen at ~700 nm wavelength in fig. 2.20. The position, where the "Dip" will appear depends on the geometry of the nanowell. "Peak" asymmetric resonance (marked at ~600 nm in the spectrum in fig. 2.20) is sensitive to refractive index changes within the interior of nanowells as well, but less than the "Dip".

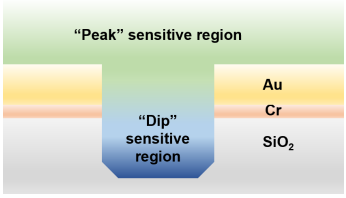

Figure 2.21: An illustrative demonstration for "Peak" and "Dip" field extensions. The "Peak" (marked in gradient green) is more sensitive to surface local refractive index changes while the "Dip" (marked in gradient blue) is for the interior of nanowells.

Even if noisier, the extinction minimum is more sensitive to the bulk RI than the maximum (estimated sensitivites of ~278 nm/RI unit and ~147 nm/RI unit, respectively) [56]. The plasmonic field sensitivity is influenced by the local volume in the nanostructure environment. For example, a higher variation in refractive index is created when more liquid volume is exposed around the nanowells in the presence of generated plasmonic fields [56, 210, 211].

2.4.1 Real-time plasmon resonance shift monitoring

As briefly mentioned in the previous subsection - the asymmetric mode resonance shifts as a function of time can be tracked for molecular binding events occurring on the metal surface or in the interior of the nanowells. An example is presented in fig. 2.22, where the gold surface is functionalized with 2 kDa thiolated PEG chains and bovine serum albumin (BSA) is adsorbed on silica inside the nanowells afterwards. The adsorption of these molecules is "sensed" by the appropriate plasmonic fields on the surface and inside the nanowells, leading to subsequent red shift of the "Peak" and "Dip".

In this specific case (fig. 2.22), BSA was not adsorbed on the gold regions of the nanowells, because the antifouling, tightly packed

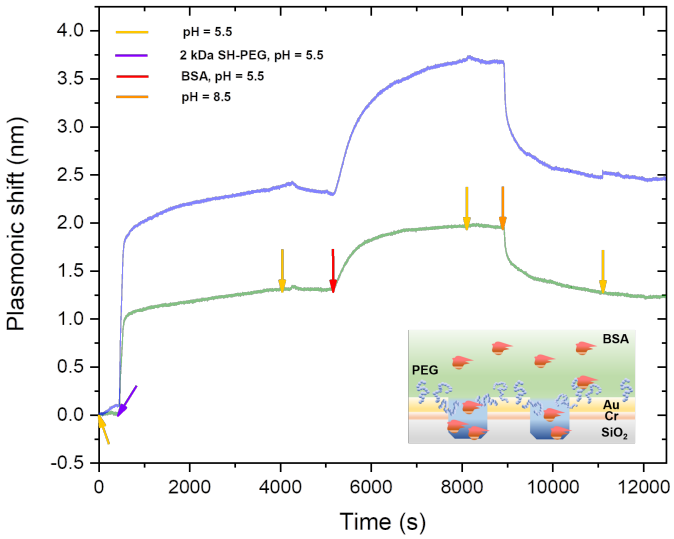

Figure 2.22: Plasmonic shift monitoring of centroid positions of asymmetric resonances "Peak" and "Dip" when 2 kDa SH-PEG and BSA are injected over the illuminated nanowell surface. The blue solid line represents "Dip" and the green is for "Peak" shifts, respectively.

PEG polymer chains are preventing them to diffuse through and bind to gold. This was indicated by reversible plasmonic shift for "Peak" at ~8900 seconds as it was before the protein injection. In addition, when the "Dip" and "Peak" ratio upon PEG film assembly (~5000 s) is taken from the experiment shown in fig. 2.22 and compared to the same ratio when BSA is adsorbed (~8800 s), it is noticed that the former one is smaller (1.716 and 2.082, accordingly), which indicates protein binding in the interior of the nanowells. This showed a convenient way of monitoring such biomolecular adsorption/desorption events as mentioned before.

2.5 Quartz Crystal Microbalance with Dissipation Monitoring (QCM-D)

Quartz Crystal Microbalance with Dissipation Monitoring (QCM-D) is an alternative technique to monitor biomolecule interactions or chemical and/or physical changes that are happening on the surface of a sensor in real time [234]. In addition, it can be applied to retrieve the information about the adhered layer's structure, thickness and solvent, which is coupled to the film [234–237]. In general, the applications span from food processing [238], marine technologies [239] to biosensors [240].

The sensing of molecule adsorption in QCM-D is based upon acoustic wave, generated by oscillating piezoelectric crystal [234]. When a certain frequency f AC voltage is applied on the sensor crystal (e.g. AT-cut shear oscillating quartz crystal [236]; fig. 2.23

a) with a similar resonance frequency f_n, a lattice deformation is induced (shown in fig. 2.23 b) [235].

The piezoelectric sensor oscillates at near resonance frequency f_n (n indicates a certain multiplier) as long as the AC voltage is applied. The resulting acoustic wave from the crystal oscillations (i.e. gold electrodes on top and below the crystal are dragged back and forth) along the sensor surface, with an amplitude A is achieved. A can be expressed by the following formulation (eq. 2.44):

$$A(t) = A_0 \sin(2\pi f_n t) exp(-D_n f_n t) \tag{2.44}$$

here, f_n is the resonance frequency and D_n is a dimensionless wave dissipation constant (i.e. energy loss per oscillation cycle) [209, 241]. The acoustic wave amplitude A starts to decay when AC voltage is turned off (as seen in fig. 2.23 c). Furthermore, f_n can be calculated by:

$$f_n = \frac{v}{\lambda} = n\frac{\nu}{2d_0} \tag{2.45}$$

here, λ is the wavelength of a standing wave between the sensor electrodes, ν is the speed of sound in the crystal sensor, n is a multiplier (i.e. an overtone), which is an odd number, and d_0 is the thickness of the crystal. In the case of 330 µm thick quartz crystal, ~5 MHz resonance frequency is obtained.

When the molecules from bulk solution adsorb on the sensor crystal, their mass is included in the collective oscillation. The generated acoustic wave, in this case, is attenuated according to the adsorbed layer's mass per area (or adlayer) m_f, thus, the resulting change in f_n (i.e. Δf_n) is expressed via Sauerbrey's equation [234, 236]:

$$\Delta f_n = -\frac{n}{C} m_f = -\frac{n}{C} \rho_f h_f \tag{2.46}$$

here, C is a material specific constant (e.g. at room temperature for 5 MHz AT-cut quartz, C is 17.7 ng·cm^{-2}·Hz^{-1} [242]), which depends on the thickness of the crystal. Parameters ρ_f and h_f are the density and height of the adfilm, accordingly.

A significant number of experiments in QCM-D are run in solutions, therefore the solvent contribution, which is coupled to the adhered film, has to be subtracted.

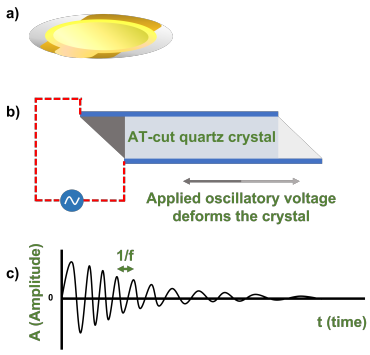

Figure 2.23: a) A gold coated QCM-D quartz sensor. b) Laterally oscillating sensor crystal when a matching frequency AC voltage is used. c) The crystal oscillates for a short period of time at resonance frequency f_n after AC voltage is shut off. Then f_n is post-processed with Fourier Transform into time domain later on.

The following formulation shows a close relationship between f_n/dissipation of a crystal, density ρ_1 and viscosity η_1 in liquids when exposed to a shear quartz resonator [234]:

$$\Delta f_n = -\frac{f_n}{2}\Delta D_n = -\frac{1}{C}\sqrt{\frac{n\rho_1\eta_1}{2\omega_F}} \tag{2.47}$$

here ω_F (=$2\pi f_F$) is the angular fundamental resonance frequency.

It is important to mention that the Sauerbrey equation (eq. 2.46) mainly applies for adlayers, which are relatively rigid films. On the other hand, if the film of interest is rather viscoelastic, more complex modelling, such as from Voigt-Kelvin, should be applied [234, 243–245].

In Voigt-Kelvin model, the shifts in dissipation and frequency (ΔD and Δf, respectively) are proportional to the viscoelastic properties of the adfilm and obtained through the β parameter in the following equations [241, 244, 246]:

$$\beta = (1-i)\eta_f\delta^{-1}tan[(1-i)d_f/\delta] \tag{2.48}$$

$$\Delta f = Im\left(\frac{\beta}{2\pi d_0\rho_q}\right) \tag{2.49}$$

$$\Delta D = -Re\left(\frac{\beta}{\pi f d_0\rho_q}\right) \tag{2.50}$$

here i is the imaginary unit, d_0 and ρ_q is the thickness and density of the quartz sensor, and d_f and ρ_f are the same variables for the adfilm. The decay length of the fluid shear wave δ is equal to $(2\eta_f/\omega\rho_f)^{1/2}$.

The sums of stresses, present on the adsorbed material due to its viscosity and elasticity, are included in the model as well and described by the complex shear modulus μ^*:

$$\mu^* = \mu_f + i2\pi f\eta_f = \mu_f(1 + i2\pi f\tau_f) \tag{2.51}$$

here, μ_f and η_f is the elastic shear modulus and shear viscosity of the film, accordingly and τ_f is the specific relaxation time, related to the deposited material ($\tau_f = \eta_f/\mu_f$).

Finally, the changes in frequency and dissipation for a viscoelastic ultrathin film in liquid, such as water, are shown by [243–245]:

$$\Delta f = -\frac{1}{2\pi\rho_q t_q}\left(d_f\rho_f\omega - 2d_f\frac{\eta_f\omega^2}{\mu_f + \omega^2\eta_f^2}\left(\frac{\eta_b}{\delta}\right)^2\right) \tag{2.52}$$

$$\Delta D = \frac{1}{2f\pi\rho_q t_q}\left(2d_f\frac{\mu_f\omega}{\mu_f^2 + \omega^2\eta_f^2}\left(\frac{\eta_b}{\delta}\right)^2\right) \tag{2.53}$$

2.6 Fluorescence microscopy techniques

In this segment, fluorescence fundamental principles and alternative microscopic techniques to study proteins will be discussed in brief.

To begin with, in order to study objects in fluorescence microscopy, an intrinsic property for a molecule to fluoresce is needed. These molecules are called fluorophores. Fluorescence or a radiative transition (fig. 2.25), can happen within a few nanoseconds when a molecule is excited with higher energy photons compared to the emitted light [247]. Emitted and absorbed light differ from one another by a certain wavelength increment, which is known as the *Stokes shift* (shown in fig. 2.24 for Alexa Fluor 488^{TM} fluorescent dye [248]). Also, the wavelengths, at which a fluorophore is excited or emits light, is mainly dependent on its outermost electron orbital.

If the excitation light is filtered out using an emission filter, only the molecules, which emit light at a higher wavelength (i.e. 'red shift') can be seen. This makes fluorescence microscopy a powerful technique to study fluorescent dye labelled proteins, even single ones [249], if a high contrast and a sensitive enough detection are achieved [250–252].

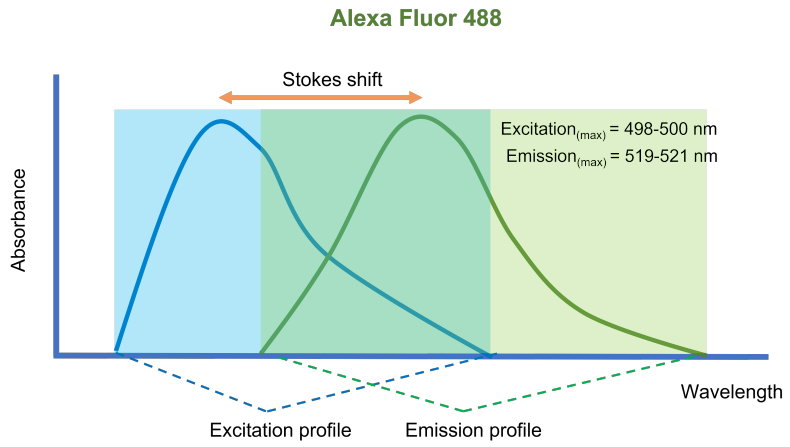

Figure 2.24: Excitation and Emission profiles for Alexa Fluor 488^{TM} fluorescent dye molecule.

Typically, when a fluorophore absorbs photon energy in its 'ground state' (a singlet S_0 with a sum angular momentum equal to 0), changes in its vibrational, rotational and electronic states may take

place. For example, an electron in S_0 can move to a higher orbital S_1 or S_2 when high enough energy is absorbed. This is termed transitioning to an 'excited state' and is seen in Jablonski's diagram (the lowest vibrational energy states are marked in bold black lines in fig. 2.25) [253–256]. In addition, the excitation induces molecular vibrations, where the distances between the nuclei start fluctuating over time. However, in the end, the absorbed photon energy is diminished when vibrational relaxation (i.e. a non-radiative transition to a lower energy level in the same electronic state) and/or fluorescence occur, returning the fluorescent molecule to its ground energy level S_0.

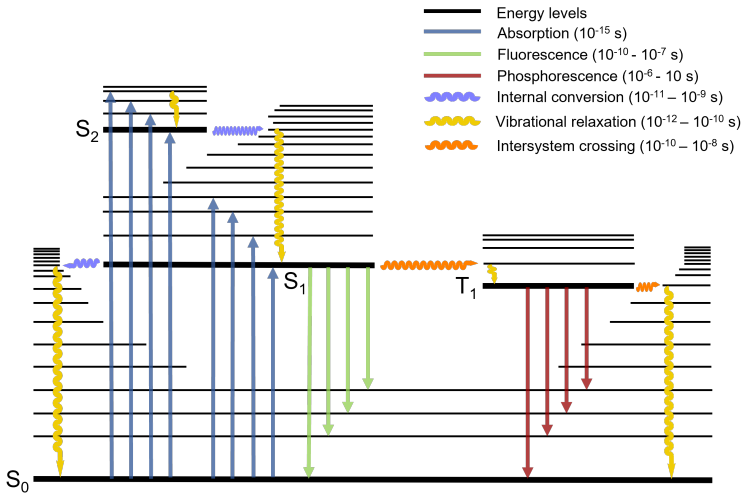

Figure 2.25: Jablonski diagram, displaying ground S_0, excited singlet S_1, S_2 and triplet T_1 electronic states and radiative with non-radiative transitions.

Figure 2.25 shows a subset of different vibrational energy levels (black lines) found between the orbitals in a fluorescent molecule. In addition, the energy increases going up vertically along the diagram and the levels eventually form a continuum (the spacings between the black lines become infinitely small) [247, 256].

Besides absorption, fluorescence and phosphorescence, which are radiative transitions, non-radiative transitions occur as well. As stated in the name, these transitions, found in between or the same orbital, do not absorb or emit any photons. Firstly, the internal conversion is a transition, which happens between two same spin multiplicity electronic states [247, 256]. It is mediated between a higher and a lower electronic state, which are in a relatively close distance from one another (i.e. from a low vibrational energy electronic state to a higher vibrational energy of a lower electronic state). During this transition, the system does not change its energy. However, if the gap between these states (e.g. S_0 and S_1) is large enough, internal conversion competes with fluorescence and intersystem crossing. The latter, is also a non-radiative transition between two energy levels, but these belong to electronic states with different spin multiplicity (e.g. between a singlet (S_1) and a triplet (T_1) excited states) [247, 255, 256].

To sum up, these are the basic principles of different transitions, including fluorescence, occurring when a molecule absorbs light with high enough energy.

In the next subsection, the differences of two most commonly used microscopy setups and further application of fluorescence in them will be overviewed.

2.6.1 Components of setups and differences between wide-field and confocal microscopy

In wide-field fluorescence microscopy setup, the fundamental components involve a light source (e.g. LED lasers), excitation and emission filters (or beam splitters), a dichroic mirror and a microscope with objectives. If fluorescent molecules are excited, the emitted light is monitored through the microscope eye piece or a connected camera, accompanied by computer digitization. The dichroic mirror separates the shorter wavelength light from the emitted photons, by reflecting it and transmitting the emitted fluorescence at longer wavelengths (fig. 2.26, left). In addition, the excitation filter, coupled to the dichroic mirror, acts as a pre-selection component for the exciting light whereas the emission filter, also coupled to the dichroic mirror, blocks the unwanted emitted light.

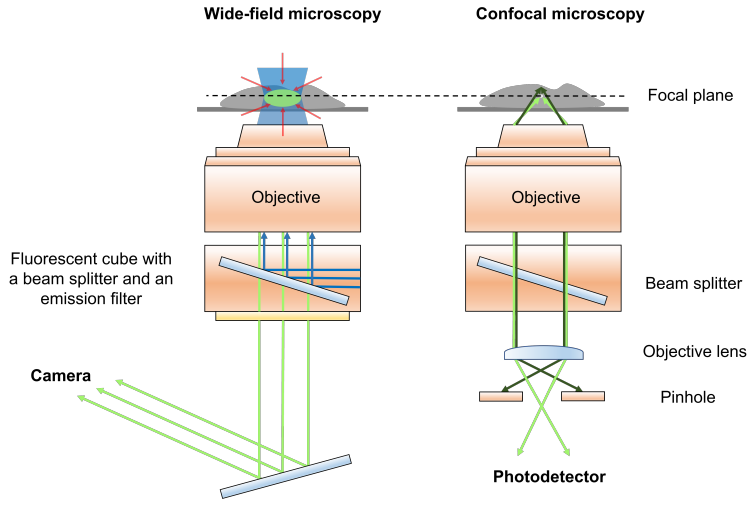

Figure 2.26: Differences in illuminated spots in samples for wide-field and confocal microscopies. The focal plane is visualized in one dimension and some components for both setups are excluded for illustration purposes. In wide-field microscopy cameras are used to take images, whereas in confocal microscopy photodetectors collect photons from scanned pixels.

In modern wide-field microscopes, filter sets are constructed in a sophisticated way that allows 1 in 10000 photon, of the incorrect excitation wavelength, to reach the sample. Due to this ratio, single molecule imaging is possible [247]. Also, a high temporal resolution can be achieved, especially with the recent development of low-noise electron multiplied charged-coupled device (EMCCD) cameras [257]. However, a few significant issues arise, when attempting high resolution imaging, and involve the diffraction limit (dictates the observable separation between two points of light)

and the detection of emitted light from several focal planes (or the observation volume). Firstly, the diffraction limit (or the limit of resolution), as described by Ernst Abbe in 1873, depends on the sample and the optics of the microscope [258]. In this case, a single point which emits light will not be visible as a dot, but rather like a blurry circle (with diffraction rings around) in the focal plane. When looked at in 3 dimensions, this blurriness is defined as the point spread function (PSF). Also, in lateral view, an Airy pattern is generated, where the center is known as the Airy disk [259]. The radius of the Airy disk (calculated by eq. 2.54) is affected by the numerical aperture (NA) and the wavelength of the excitation light ($\lambda_{ex.}$) [257, 260].

$$r_{Airy} = \frac{0.61\lambda_{ex.}}{NA} \tag{2.54}$$

It is possible to resolve two point objects when they are at a spacing between each other greater than r_{Airy} (also known as the Rayleigh rule) [261]. For example, two Alexa fluor 488^{TM} fluorescently labelled BSA molecules, should be spaced by at least 233 nm if imaged with a 1.3 NA objective. If not, they would appear to be convoluted in one diffraction limited dot.

A possible solution to overcome this limitation is to use confocal microscopy (the basics first explained by Marvin Minsky in 1957 [262]), which employs pinholes to reduce the out-of-plane illumination and focus the excitation beam in a small spot (fig. 2.26, right). This alone almost doubles XY resolution compared to a wide-field microscope (from eq. 2.55), because the emitted light from out-of-focus planes is not detected anymore (in contrast to wide-field microscopy setups, where emitted light is detected from many focal planes) [263, 264].

$$r_{Airy} = \frac{0.4\lambda_{ex.}}{NA} \tag{2.55}$$

On the other hand, the downside of confocal microscopy is that it is not always the best way of imaging dynamic processes (e.g. the budding of yeast). These require a relatively long imaging time (i.e. many images), fast image acquisition speed, high resolution in vertical dimension and signal to noise ratio [257]. Consequently, this microscopy technique calls for a high intensity light as an illumination source to achieve similar photon count in comparison to wide-field microscopy [257, 263]. Nevertheless, the optical sectioning, which is offered by confocal microscopy, allows to reconstruct a full structure of a specimen in all three dimensions and may deem useful in imaging cells and proteins [265, 266].

In the following subsections, fluorescence methods to observe single protein interactions or their conformational state variations, will be discussed in short.

2.6.2 Förster resonance energy transfer (FRET)

Förster resonance energy transfer (FRET) is a well-known, non-radiative event, where a donor, or an excited fluorophore, transfers its absorbed excess photon energy to an acceptor and excites it [267–269]. Also, the event occurs at relatively small distances (between 1 - 10 nm) and is based on oscillating dipole-dipole interactions (fig. 2.27).

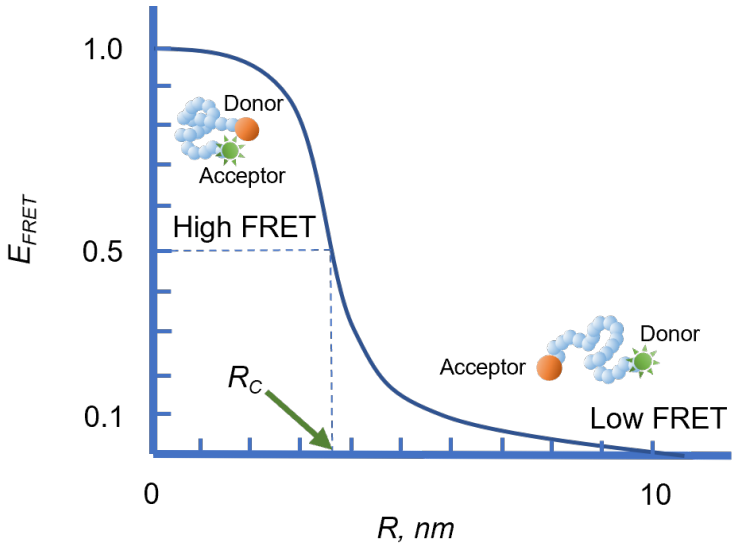

Figure 2.27: An illustration of common "FRET" and "no FRET" event between and acceptor and a donor fluorophores. The higher the distance between the donor and acceptor, the lower FRET efficiency becomes [267].

When the excited molecule is about to return to the ground energy level, it is expected to emit photons or fluoresce. The efficiency of this process E_{FRET} is inversely proportional to the sixth power of the spacing R between the two fluorophores (eq. 2.56) [267–269].

$$E_{FRET} = \frac{R_c^6}{R_c^6 + R^6} \tag{2.56}$$

here, R_c is the critical distance, where the FRET efficiency is at 50% and is known as a characteristic parameter, different for each FRET pair (fig. 2.27) [267]. When the spacing between two FRET fluorophores is less than R_c (calculated with eq. 2.58), the FRET efficiency is almost at maximum, which is in contrast to lowest efficiency, when the distance is higher than R_c value. E_{FRET} can also be estimated from the fluorescence intensity (based on donor's intensity I_{DA} when an acceptor is in its vicinity and the donor's intensity I_D without the acceptor):

$$E_{FRET} = 1 - \frac{I_{DA}}{I_D} \tag{2.57}$$

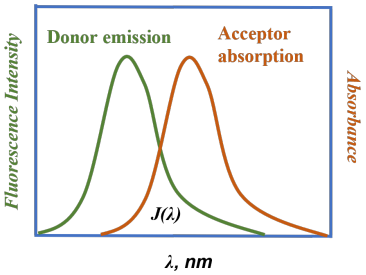

Figure 2.28: A spectral overlap J_λ, shown between donor emission and acceptor absorption.

In general, FRET may only happen when the emission profile of the donor fluorophore overlaps significantly with the excitation profile of the acceptor (i.e. acceptor absorption; fig. 2.28).

The overlap integral ($J(\lambda)$) is directly related to the critical distance R_c [267]:

$$R_C = (8.79 \cdot 10^{-5}(\kappa^2 n^{-4} Q_D J(\lambda)))^{\frac{1}{6}} \tag{2.58}$$

here κ^2 is the angle between two FRET molecule dipole moments, Q_D is the quantum yield (i.e. for the donor molecule) and n represents the medium's refractive index [267, 269]. Furthermore, $J(\lambda)$ can be determined with the following equation:

$$J(\lambda) = \frac{\int F_D(\lambda)\epsilon_A(\lambda)\lambda^4 \, d\lambda}{\int F_D(\lambda) \, d\lambda} \tag{2.59}$$

where $F_D(\lambda)$ is the normalized donor fluorescence, λ is the wavelength in the spectrum and $\epsilon_A(\lambda)$ is the molar extinction coefficient of the acceptor.

To sum up, FRET is highly advantageous and can be used to study single biomolecules. This is because it can be applied to monitor dynamic processes such as conformational changes in proteins or intracellular signalling as a function of time [267, 270–272]. In addition, when coupled to photodetectors and pulsed sources it can be used to track observation times of nanosecond scale (i.e. timescale over which most biomolecular events happen) and the use of highly dilute solutions [253, 256, 273]. Also, FRET is often combined with Fluorescence correlation spectroscopy (FCS) to probe kinetics, photophysical properties and dynamics [271, 274–276].

Experimental 3

All of the sections in this chapter were rewritten from my licentiate thesis. They include details about applied methods and protocols for sensor cleaning, polymer brush grafting and experimental setups.

3.1 Materials and chemicals

Materials and chemicals, used in this thesis, are listed in appendix A (table A.1).

3.2 Experimental

3.2.1 Nanostructure fabrication protocol

Nanostructures and nanopore arrays (membranes) were manufactured with a protocol reported by Malekian et. al [56] previously. The process of nanostructure fabrication is depicted in fig. 3.1.

Firstly, fused and amorphous silica was employed as a substrate for polystyrene colloid adsorption, which were used for nanowell or nanocave patterning. Then, once the colloids were adsorbed on silica, oxygen plasma follows with the etching of the colloids to the required size (i.e. will result in certain diameter pores later on). After the colloids were shrunk, chromium (adhesion layer), gold and aluminum oxide layers were deposited by physical vapor deposition (PVD) with ~2 nm, 30 nm and 20 nm thicknesses, respectively. Alumina layer was coated on due to the fact, that it acts as a shield for gold from possible contamination and prevents from scratching the surface when rubbing off the colloids. Moreover, colloids were carefully rubbed off and "dry" or "wet" etching was used to achieve either nanowells or nanocaves (i.e. by oxygen and carbon tetrafluoride mixture (1:4) or hydrogen fluoride, accordingly; as seen in fig. 3.1). In the case of "wet" etching, alumina film was specifically removed without affecting the gold, whereas for "dry" etching, it has to be gotten rid of by introducing a dilute base solution (e.g. sodium hydroxide). Finally, the surfaces were annealed at 250 °C for ~1 hour and stored for further functionalization.

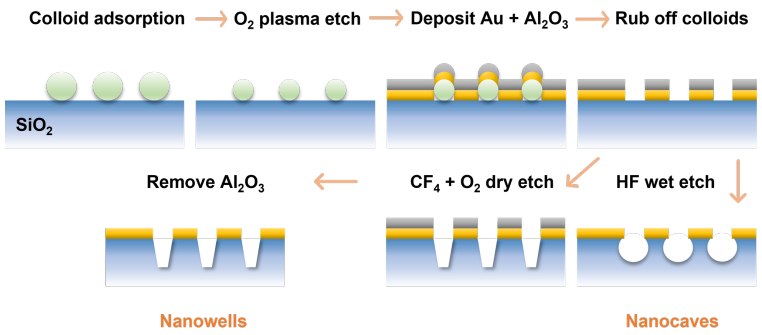

Figure 3.1: Step by step procedure for nanowell and nanocave fabrication.

3.2.2 Nanopore (membrane) fabrication

To begin with, SiN_x was deposited on both sides of 4-inch Si wafer by low pressure physical vapor deposition (LPCVD). Membrane windows with an area of ~10000 μm^2 were defined in SiN_x film with photolithography followed by reactive ion etching (RIE). Afterwards, they were directed towards the 100 Si substrate by the isotropic KOH wet etching, which results in a freestanding SiN_x membrane on the Si substrate [227].

When SiN_x membranes were prepared, the nanopore arrays (in ~300 nm periodicity) were fabricated on with Electron Beam Lithography (EBL). In this approach, the 4-inch Si wafer with SiN_x membranes was first spin-coated with a Ti prime (2-methoxy-1-methyl ethyl acetate and 2-methoxypropylacetate) at 3000 RPM for 20 seconds as an adhesion layer, followed by a negative resist ma-N 2403 (cyclopentanone and anisole). The nanopore array pattern was dictated by a focused electron beam on the e-beam sensitive resist using 100 kV electron beam machine (JEOL JBX 9300FS). Afterwards, the regions, which were not exposed to the e-beam were dissolved in Ma-D 525 solvent (containing tetramethylammonium hydroxide) and the arrays of 'pillars' were produced. Furthermore, the arrays of pillars were coated by a 1 nm layer of Cr, followed by a 30 nm layer of Au and a 20 nm layer of Al_2O_3 using e-beam PVD. After the deposition, the pillars coated with metal were removed by a chemical lift-off process, leaving nanopores in the Au film. During the fabrication process only an area of ~100 x 100 μm^2 was exposed.

In this thesis, only ~150 nm diameter membranes were fabricated (with a variation of ~10 nm on the same side, but also on the back side of the pore (i.e. the pore was slightly conically shaped) and can be seen in fig. 3.2. These sample surfaces consist of 9 membranes, where each has ~136900 pores (pore distribution was calculated from SEM images and multiplied by the area of the membrane, which is 110 x 110 μm^2).

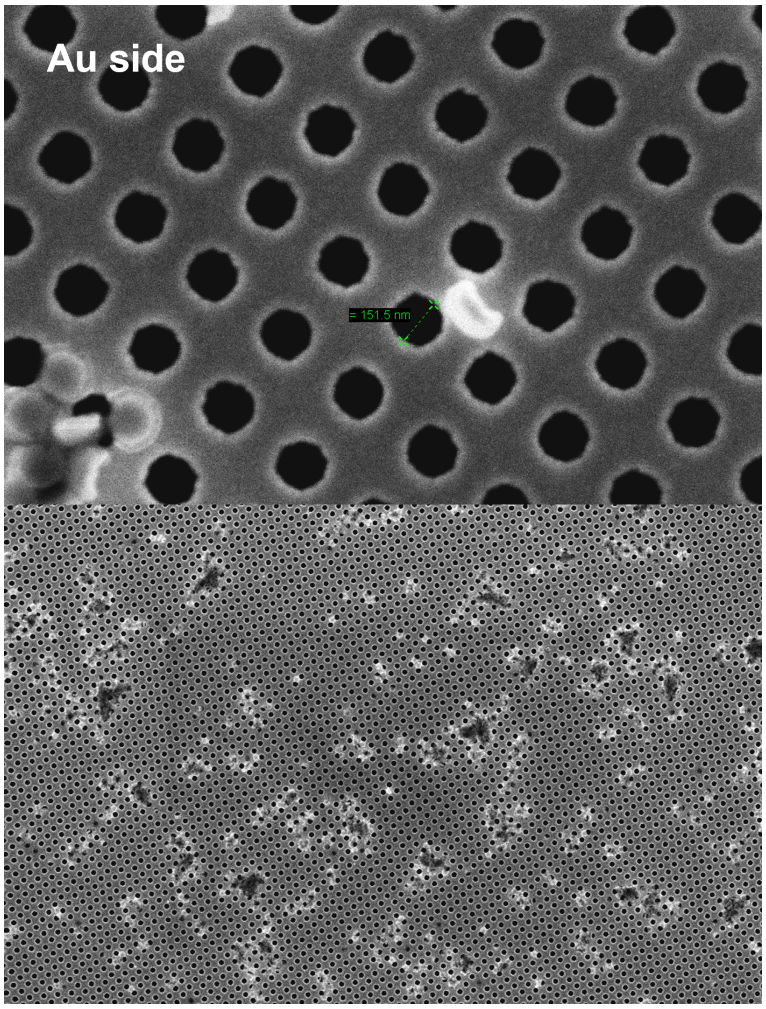

Figure 3.2: SEM images of ~150 nm nanopores, taken from the top (i.e. Au film) side.

3.2.3 Surface plasmon resonance sensor fabrication

Au SPR chips with a 2 nm layer of Cr and a 50 nm layer of Au were prepared by electron beam heated physical vapor deposition (Lesker PVD 225; same for Pt and Pd layers, but 20 nm thickness) on glass substrates (Bionavis), which were cleaned beforehand with RCA-2 (1:1:5 volume of conc. HCl : H_2O_2 (30%) : H_2O at 80 °C) and 50 W O_2 plasma at 250 mTorr. Moreover, if SPR chips were required to have silica as a top layer on gold, silica was deposited with atomic layer deposition (Oxford FlexAL) at 300 °C by using a bis(t-butylamino)silane (BTBAS) as a precursor and oxygen as processing gas. This results in a thin layer of Si with ~12-15 nm thickness.

3.2.4 Sample cleaning procedures

RCA-1 sample cleaning protocol - a sample surface (e.g. SPR chips or nanowells) was placed into a mixture of milliQ water (MQ; ultra-filtered water with resistivity of 18.2 MΩ·cm at 25 °C), ammonium

hydroxide and hydrogen peroxide solution in a volumetric ratio of 5:1:1 for 20 minutes at 75 °C. After RCA-1 cleaning was done, samples were thoroughly rinsed with MQ water and dipped in ethanol (99.5%) for 10 minutes. After, the surfaces were dried with nitrogen and further functionalized or stored for later use.

Piranha sample cleaning protocol - only planar surfaces (e.g. SPR or gold coated QCM-D chips) were cleaned with this method due to the chromium adherent layer for nanowells dissolving and thus detaching the gold film from the silica. The samples were submerged in a solution of sulfuric acid (H_2SO_4) and H_2O_2 at a ratio of 3:1 for 30 minutes.

UV-ozone - a sample surface (e.g. silica coated SPR chips or QCM-D chips) was placed in a UV-ozone chamber (in-house; no oxygen supply, just ambient air) for 30-60 minutes and blown with nitrogen before use.

Alumina layer removal - nanowell surfaces were placed in a 10 mM sodium hydroxide solution for 1 hour, followed by rinsing with MQ water and drying with nitrogen.

3.2.5 Molecular sieve drying

Molecular sieves were used to keep methanol (one of the solvent mixture components for the ARGET-ATRP reaction) dry from water.

1. 3Åmolecular sieves were vacuum dried (at ~100-200 mBar) overnight at at 300 °C.
2. Afterwards, the sieves were directly placed in a desiccator until further use.

3.2.6 Self-assembled monolayer (SAM) assembly

1. Sample surfaces were placed either in 1.5 mM HS-C_{11}-OC(O)-IzoButyrate-Br (TBU) or Bis[2-(2-bromoisobutyryloxy)undecyl] disulfide (DTBU) dissolved in (99.5%) and left to stir at 100 RPM overnight.
2. When the self-assembly was done, the sample surfaces were sonicated in 99.5% ethanol in a sonication bath (35 kHz) for 1 minute, rinsed with ethanol and dried with nitrogen.

3.2.7 ARGET-ATRP reaction

ARGET-ATRP for PNIPAM polymer brushes on gold coated nanowells (i.e. alumina layer removed beforehand) follows a scheme shown in previous subsection 2.1.4. The total volume of the solvent mixture (i.e. methanol and MQ water in varying volume %) was 49 mL in a closed cap jar. The monomer, reduction agent, ligand and catalyst were kept at these concentrations in the final volume of the reaction solution:

Chemical	Molar concentration, M
N-isopropylacrylamide	0.48
N, N, N′, N″, N″- -Pentamethyldiethylenetriamine	0.0064
Ascorbic acid	0.010
$CuBr_2$	0.0006

Table 3.1: Chemicals utilized in ARGET-ATRP reaction and their molar concentrations.

The reaction was performed in a laboratory fume hood and not in the glove box, hence extra care in order to avoid oxygen during the reaction was needed. Consequently, the polymerization setup includes a running nitrogen line, which was attached to a gas flow meter, the reaction jar and degassing flask with a transfer needle in between, and a dry compressing vacuum pump (DIVAC 1.4HV3C) as seen in figure 3.3.

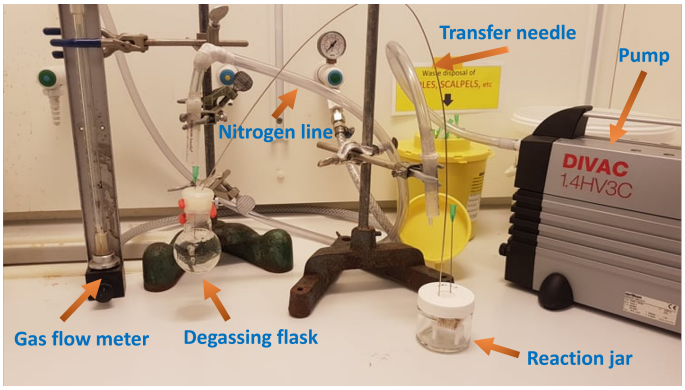

Figure 3.3: ARGET-ATRP reaction setup for PNIPAM polymer brushes on gold coated nanowell or planar SPR surfaces.

Step-by-step protocol for PNIPAM polymer brush polymerization:

1. $CuBr_2$ was weighed on anti-electrostatic weighing paper and added to a round bottom flask (previously rinsed with methanol and dried with nitrogen). Afterwards, an appropriate solvent volume mixture of methanol (filtered through 0.2 µm syringe filter) and MQ water was added and N, N, N′, N″, N″-Pentamethyldiethylenetriamine (PMDETA) was injected. A rubber septum was placed around the neck and on the top of the flask and everything was mixed well until homogeneous blue solution color was observed.

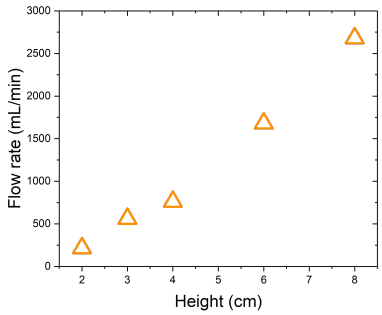

Figure 3.4: Flow rate of nitrogen gas plotted against the 'height' level on the gas flow meter.

2. The solution was transferred into a degassing flask containing desired weight of N-isopropylacrylamide (NIPAM), a rubber septum was covered around it and two needles were pierced through the septum. One syringe needle was to be attached to a running nitrogen line, connected to a gas flow meter, and another was a transfer needle, which connects the degassing flask and reaction jar (as seen in fig. 3.3).
3. Nitrogen gas was flowed through the solution with reactants for 30 minutes at a flow rate of ~560 mL/min (at height of ~3.5 cm; gas flow meter calibrated with Agilent ADM flow meter; see fig.3.4).
4. 10 minutes before the degassing was done, the vacuum pump was attached to the reaction jar (containing sample surfaces placed on a teflon stand), the needle from the nitrogen line needle was taken above the reaction solution (still inside the degassing flask) and the transfer needle was dipped instead. The reaction mixture will start flowing through the transfer needle and fill the capped jar with the sample surfaces when the pump was turned on.
5. When the reaction solution was transferred to a reaction jar, inject 200 µL of ascorbic acid dissolved in MQ water beforehand to initiate the polymerization.
6. The reaction was run for the required amount of time and stopped by opening up the jar and dipping the teflon stand into ethanol. Afterwards, polymer brushes coated surfaces were dried with nitrogen and stored in covered sample holders for further experiments.

3.2.8 PEG grafting on gold surfaces

20 kg/mol thiol-terminated PEG was grafted on planar gold SPR sensors at 0.12 g/L concentration in filtered 0.9 M Na_2SO_4 solution for 2 hours under 50 RPM stirring. When the grafting finished, the sensors were thoroughly rinsed with MQ water and dried with N_2. Consequently, functionalized SPR sensors were immersed in MQ water on a teflon stand overnight.

2 kg/mol thiol-terminated PEG was grafted on planar gold/platinum/palladium surfaces at 1 g/L concentration in real-time, e.g. SPR, measurements in PBS buffer (pH = 7.4) until saturation of signal was reached. After this, rinsing with PBS buffer followed, which washes away the excess molecules from the surface.

3.2.9 Silica surface functionalization with 3-aminopropylsilatrane (APS)

The silica interior of the nanowells can be functionalized with 3-aminopropylsilatrane (APS) molecules to contain primary amine moieties with the following steps:

1. Dip the nanowell surface (coated or without a polymer film) in 460 μM APS solution in 99.5% EtOH solution for 10 minutes.
2. Rinse with 99.5% EtOH after incubation.
3. Anneal the surface on a hotplate for 1 hour at 70 °C.

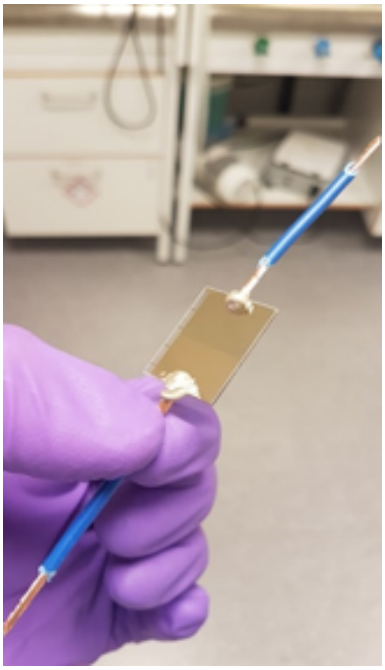

Figure 3.5: A photo of a half planar gold, half nanowell covered sample surface.

3.2.10 Wide-field fluorescence microscopy experiments

Fluorescence experiments have been conducted on half-half nanowell surfaces (half of the surface was planar gold while the other contains nanowells; fig. 3.5) with a custom made flow cell (see fig. 3.6; detailed blueprints can be found in Appendix B) and an optical Axio Observer microscope, equipped with an EMCCD Andor IXon Life camera (pixel size 13.00 x 13.00 μm). As shown in fig. 3.5, insulated copper wires were attached onto the sample surface with conductive glue to facilitate local resistive heating when voltage was applied (with Gamry potentiostat interface 1000).

Alexa Fluor 488^{TM} (AF488) fluorescently labelled BSA proteins were used for fluorescence experiments. The illumination was done in epi-mode with a 475 nm LED (100% intensity). In short, the light passes through a beam splitter, which reflects 452 - 486 nm wavelength towards the sample (other wavelengths pass through) and then the emitted light passes through the emission filter (transmits 500 - 528 nm wavelength, others were blocked) and was detected by the camera, as indicated in fig. 3.7.

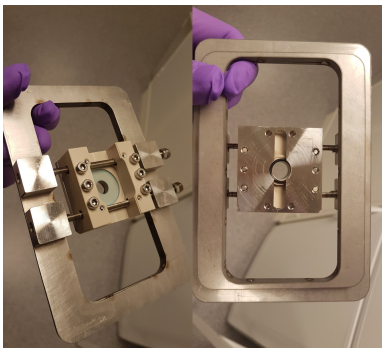

Figure 3.6: A photo of a flow cell, which was used for protein transport gating experiments

During the experiments, images were taken through a 50x air objective (LD EC EPN 50x/0.55 BD DIC WD=9 mm) from the silica side, whereas the opposite side with planar gold and nanowells was exposed to the liquid within the flow cell. 100 ms exposure time was used for multi-nanowell (images taken every 60 seconds) and 5000 ms for single nanowell experiments. In addition, an EM gain of 250 was utilized for image acquisition during the fluorescent BSA protein transport gating. Once the pictures were gathered in ZVI format (from the zen software), they were converted to TIFF with ImageJ software. Afterwards, a matlab program was run (can be found in https://pastebin.com/MvDPnvr4, password: 0NN4E1xPPG), where fluorescence intensities between planar gold and nanowell covered side were retrieved from the TIFF files.

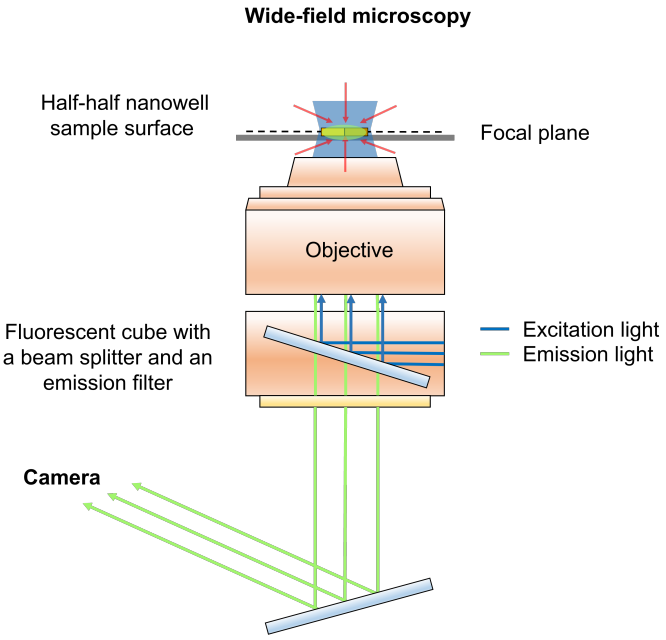

Figure 3.7: Sample illumination pathway during fluorescence microscopy measurements.

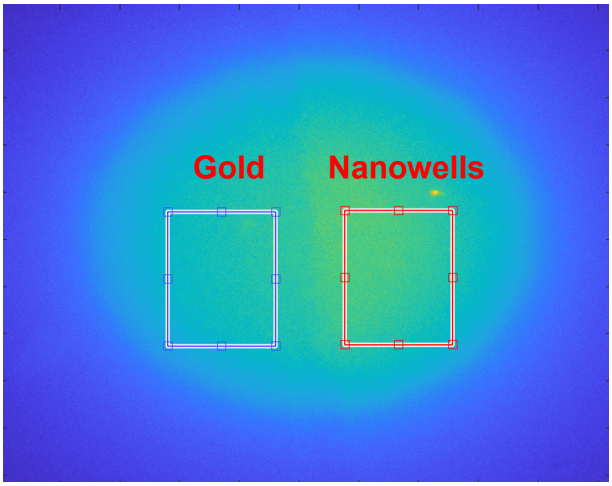

Figure 3.8: A picture, indicating planar gold (left) and nanowell (right) same area regions under microscope.

The difference (fig. 3.8) between the fluorescence intensity on the nanowell and gold sides (i.e. same sized areas) was assumed to be the fluorescence arising from the fluorescently labelled proteins in the interior of the nanowells.

3.2.11 Extinction spectroscopy experiments

Real-time extinction spectroscopy experiments were run in transmission mode, where a lamp (B&WTek BPS2.0) and spectrometer (Cypher^{TM} H (B&WTek) for visible/near-infrared light were employed.

These buffers were used for most of the real-time experiments (including SPR, QCM-D, etc.): 1x phosphate buffered saline (PBS; 10 mM phosphate, 137 mM NaCl and 2.7 mM KCl) and 1x borate

buffered saline (BBS; 10 mM borate and 150 mM NaCl). The pH was adjusted as required per experiment.

Nanowell containing surfaces were mounted in a custom made flow cell (same as in fig. 3.6) and flow of buffers or dissolved proteins (at a concentration of ~116 μg/mL unless stated otherwise) was facilitated over the sample by a peristaltic pump (Ismatec^{TM} MS-2/6 Reglo Analog Pump). Moreover, the local heating on the sample surface was induced by resistive heating upon applying voltage on surface attached copper wires with Gamry potentiostat interface 1000.

The centroid position shifts of the asymmetric plasmonic modes (like mentioned previously in subsection 2.4.1) were tracked with a custom designed Labview software and plotted as a function of time.

3.2.12 Surface plasmon resonance experiments

SPR sensors chips were fabricated in the clean room as described before and afterwards cleaned with appropriate protocols.

SPR Navi^{TM} 220A instrument (BioNavis) was equipped with three lasers (785 nm, 670 nm and 980 nm), which induce different decay lengths of sensing fields. The SPR spectra were taken from 2 flow channels, which were exposed to the metal side of the same chip, but different areas in parallel. This allows to estimate of how uniform the coated layer on the sensor was.

The running buffer was chosen to be either PBS or MQ water and flows at ~10 - 50 μL/min during the experiments. Once the stable baseline was established, injections may be automated by using an autosampler and a 96-well plate. Temperature control allows going up to 40 °C, however, unless stated otherwise, 25 °C temperature was utilized in all of the experiments.

Dry and exclusion heights of layers, functionalized on metals, were calculated in the same manner as described before [90, 219]. In short, the refractive indexes and thicknesses of metal layers were independently determined with Fresnel modelling before grafting polymers on the surfaces. Once, the correct parameters were found, they were used again when another layer was introduced (e.g. PEG with a refractive index of 1.46). Likewise, the hydrated polymer brush thickness was determined with Fresnel models when a non-interactive probe (e.g. 35 kDa PEG for PNIPAM polymer brushes) was present and absent in the bulk liquid [90]. Also, a linear baseline correction was sometimes done if the drift in SPR angle was the same through the whole experiment. A custom matlab script has been written in order to fit the acquired spectra.

In regards to Pt and Pd measurements in liquid, a second-degree polynomial around the angle was applied to improve signal-to-noise (includes 200-400 points). A moving average algorithm was used to smoothen the spectra, because the TIR angle cannot be tracked with the Bionavis instrument software for Pd and Pt. In this case, the TIR angle was defined as the maximum of a third degree polynomial fit around the peak in the first derivative of the spectrum [1].

3.2.13 Quartz Crystal Microbalance with Dissipation Monitoring measurements

Experiments were run with a Q-Sense E4 instrument (from Biolin Scientific) equipped with a sensing chamber with 4 available flow cells and a peristaltic pump (from Ismatec) as demonstrated in figure 3.9. Clean QCM-D gold or silica crystals (with or without PNIPAM polymer brushes) were placed into a flow cell (or more than one, depending on the quantity of necessary experiments) and a buffer (e.g. PBS) was injected at ~50 - 100 μL/min until a stable baseline was seen. Protein concentration was ~116 μg/mL unless stated otherwise. The data was acquired over 6 overtones (e.g. 1st, 3rd, etc.), but only the 5th overtone was taken to represent an experiment.

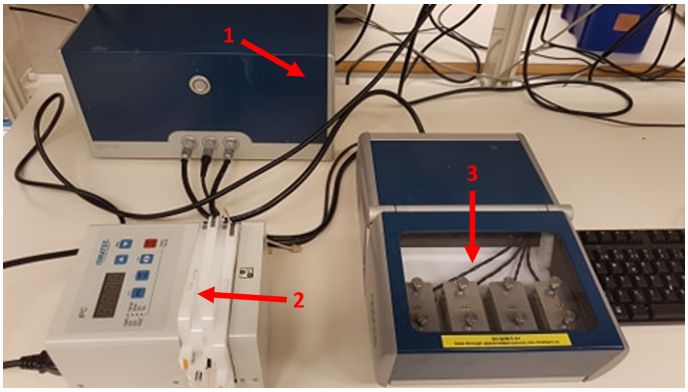

Figure 3.9: QCM-D components. 1 - q-sense analyzer, 2 - peristaltic pump, 3 - a sensing chamber with 4 flow cells.

Summary of results in publications

4

4.1 SPR sensing with thin platinum (Pt) and palladium films (Pd)

SPR being a tremendously useful optical technique to study biomolecules and films lacks diversity in the sensors, which are used in the experiments. Nowadays, most measurements are conducted on gold coated silica surfaces [277–279], which takes away the possibility to monitor chemical modifications done on other metals. For example, Pt and Pd are highly significant in various applications, including heterogeneous catalysis [280, 281], zero mode waveguides (Pd) [52] and electrochemical cells (Pt) [282]. In addition, these metals are particularly interesting as they provide high chemical stability, which compared to some past attempts to use silver metal instead of gold proved to be an issue as it oxidizes in ambient conditions [283–285].

In the work presented further on, we show that thin (20 nm; fabricated as described in subsection 3.2.3) Pt and Pd films in water can be used for real-time SPR measurements (Kretschmann configuration) of molecular binding events. In addition, when SPR spectra are taken in air - quantification of surface coverage by Fresnel modelling is possible. Unfortunately, these metals absorb light to a rather high extent, for example, compared to gold, therefore the plasmon resonances are very broad. Nevertheless, obvious intensity changes found close to the TIR angle can be observed and used to quantify the amount of molecules on the modified surfaces.

To begin with, we estimated the optimal thicknesses of Pt and Pd, which are deposited on silica (with a ~1 nm Cr adhesion layer in between) for SPR experiments. The reflectivity spectra (fig. 4.1) for these metals were simulated with Fresnel models by using the transfer matrix method [90]. In fig. 4.1 a), a tendency to show reflectivity minima for the thinnest films (i.e. 10 and 20 nm) is seen even if they are significantly broadened due to the characteristic property of Pt and Pd to absorb light. In addition, a steep change in reflectivity between the SPR angle (the minimum in the reflectivity spectra) and TIR angle at 41.14 degrees is recognized. Notably, the higher angle region in gold reflectivity spectra rises [225], forming a narrow dip [286], but this happens only slightly for Pt/Pd reflectivity spectra and no distinguishable dip is formed for spectra in air.

The optimal layer thickness for both Pd and Pt was determined to be as low as 10 nm (based on the sharpness of the reflectivity minimum). Also, it is known that for thin films, the wave propagation length increases depending on a coupled mode in Kretschmann configuration. Nevertheless, 20 nm film thickness was chosen for further experiments, because fabricating a continuous metal film of 10 nm or less with vacuum deposition methods could be a challenge.

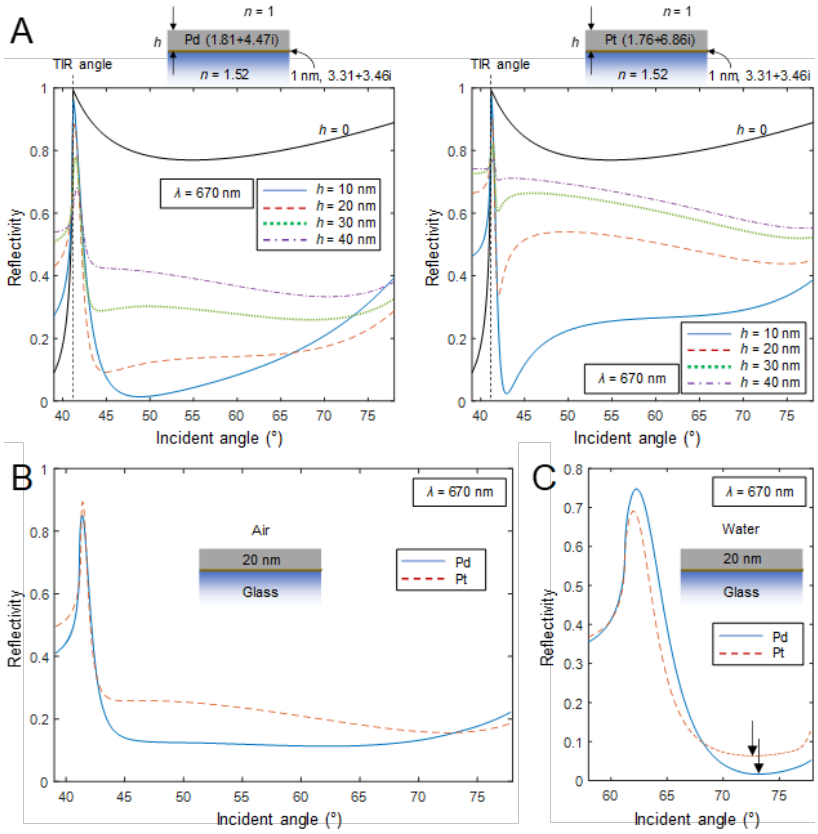

Figure 4.1: In a), simulated reflectivity spectra of Pt and Pt films with 670 nm incident light can be seen (Kretschmann configuration). Pt and Pd SPR angular spectra in air (b) and water (c). The black arrows in c) show reflectivity minima (SPR angle).

In fig. 4.1 b) experimental spectra of Pt and Pd in air are seen, where no clear reflectivity minima can be identified. Still, the spectra are similar to the ones predicted with Fresnel models (fig. 4.1 a). When Pd and Pt surfaces are exposed to water, the reflectivity minima are detected and indicated with the black arrows in fig. 4.1 c). The refractive indexes of Pt and Pd were obtained by Fresnel models by letting the complex refractive index to vary and keeping the metal film thicknesses constant (20 nm) as measured from the deposition instrument. Consequently, n for Pd and Pt are calculated to be 2.25 + 4.60i and 2.47 + 5.28i, respectively (at 670 nm vacuum wavelength). While being slightly different from some studies (2.43 + 4.36i for Pt and 1.81 + 4.48i for Pd [287, 288]), the values are similar to others (2.45 + 5.51i for Pt and 2.12 + 4.77i for Pd [289, 290]). Therefore, we conclude that the differences may arise from how the layers are originally formed (e.g., depending on the grain size, etc.).

To illustrate how Pt and Pd surfaces may be used to monitor organic layer adsorption, measurements in air were performed before and after binding PEG. The quantification of adsorbed film was done with Fresnel models just as before (when non-functionalized Pt and Pd surface reflectivities were simulated), but with an addition of one more layer (n is set, but the film thickness is allowed to vary). The reflectivity measurements of deposited polymer films in air are advantageous in a way, because n and material density can be found in literature [219], thus, the film thickness and surface coverage can be estimated.

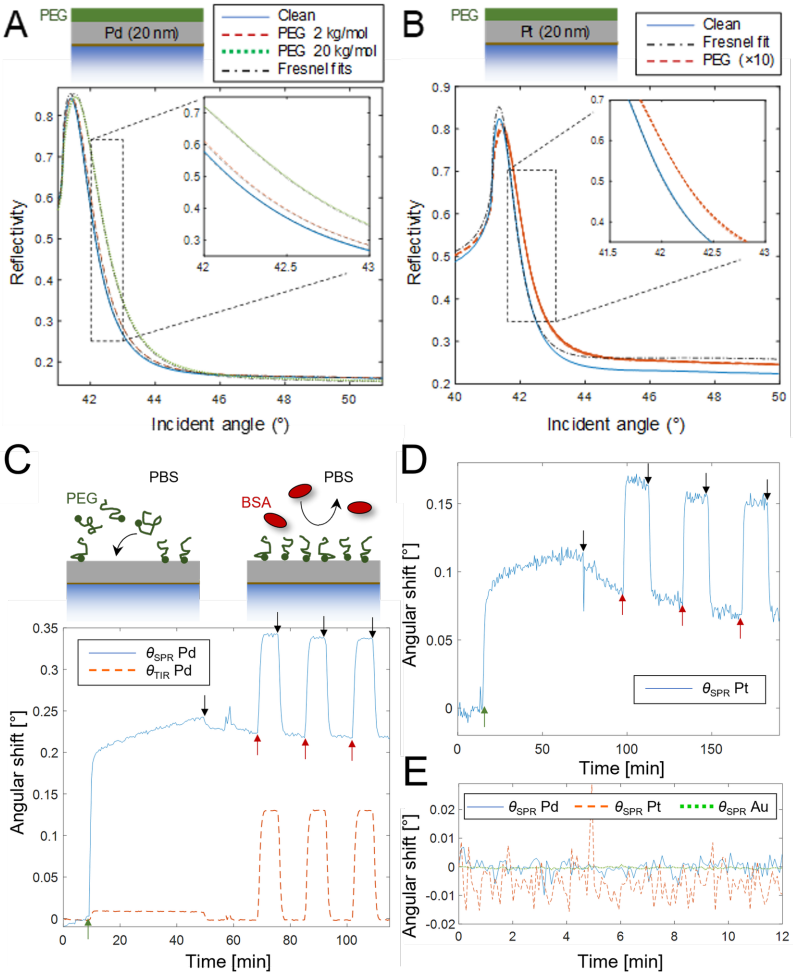

Figure 4.2: Pt and Pd surfaces with grafted PEG films. a) Reflectivity spectra measured in air before and after coating of PEG-SH (2 and 20 kDa mol. weights) to Pd sensors. A Fresnel model fitted for each case. In b) Same as in a), but for Pt (only 2 kDa PEG-SH is shown), the measurement is repeated 10 times to indicate variation. c) and d) show real-time acquisitions of 2 kDa PEG-SH (1 g/L) adsorption on Pt and Pd, followed by BSA protein injections (red arrows; 10 g/L). The black arrows indicate rinsing with the running buffer, whereas the red ones are BSA protein injections. e) Noise levels in PBS running buffer for Pd, Pt and Au films.

Subfigures a) and b) in fig. 4.2, show Fresnel model fitting of Pd and Pt surfaces before and after coating with thiolated PEG (PEG-SH) films, respectively. In a), two different molecular weight (2 and 20 kDa) PEG-SH films are grafted and in b), only 2 kDa PEG-SH layer is coated on the sensor. To quantify the dry thicknesses of PEG on Pt and Pd sensors, we assumed that the water uptake for PEG is negligible at ambient air humidity [291]. The steep region found between the TIR and SPR angle signifies intensity changes after grafting PEG films both for Pd and Pt (fig. 4.2 a) and b). In addition, as previously proposed [286], this part of the spectrum

should be used for analysis in order to get the most accurate results. To show the possible uncertainty of the measurements, we have fitted Fresnel models into multiple spectra seen in fig. 4.2 b) (10 repeats) and estimated an average PEG dry thickness of 2.23 nm with 0.02 nm standard deviation. Other wavelengths, e.g. 785 and 980 nm, can be used for spectral analysis as well with little variation in the results. For example, by calculating the surface coverage of PEG on Pd surface of 6 independent measurements with another wavelength, the change in the result was on average 11.8%. Similarly, when the measurements (PEG grafted on different surfaces) were carried out for the same wavelength, the deviation was 11.4%.

Real-time monitoring of SPR angle change due to molecule adsorption is shown in subfigures c) and d) for Pd and Pt in water, respectively. 2 kDa PEG-SH was injected in both cases to form an antifouling layer for BSA protein (injected multiple times afterwards). The injections of the protein raise the bulk refractive index as seen by reversible complementary TIR signal changes. On the other hand, when Pt and Pd are not coated with PEG, BSA adsorbs irreversibly, but it is not shown here. Furthermore, the baseline noise level for Pt is higher than for Pd and the change in SPR angle is almost twice as small. Finally, Pt, Pd and Au (50 nm film thickness, in this case) baseline noise levels can be seen in subfigure e), where Pt baseline is clearly the noisiest in terms of SPR angle shift.

In conclusion, with these results we extend the applicability of SPR for real-time molecular adsorption/desorption event tracking in water to other metals besides most commonly used Au. Also, we show that quantitative analysis may be carried out fairly straightforwardly if full angular spectra are acquired.

4.2 Accurate "bulk response" correction in SPR

As briefly described in subsection 2.3.4, the "bulk response" issue in SPR has been evident for decades (seen for planar and other geometries [219, 292]) and is one of the reasons why many SPR papers published each year have doubtful interpretations [293]. Herein, we present a correct analytical solution to separate the "bulk response" from the SPR signal, indicating interactions happening on the surface of interest. We note that it is extremely important to do this especially when weak interactions in highly concentrated samples are monitored and the bulk signal (coming from molecules, which do not bind to the surface) dominates the SPR angle shift.

Firsly, the theroretical framework for our proposed analytical solution comes from the effective field decay method in SPR signal quantification for hydrated layers such as polymer films (e.g. PEG polymer brushes) on sensors [294]. The formulation, which relates the SPR signal and the change in the refractive index can be expressed as:

$$\Delta\Theta_{SPR} = \frac{2S_{SPR}}{\delta}\int_0^{\infty} exp\left(-\frac{2z}{\delta}\right)\Delta n(z)dz \tag{4.1}$$

where S_{SPR} is the bulk sensitivity parameter in deg per refractive index unit, z is a distance from the surface and δ indicates a distance from the surface where the evanescent field decreases by a factor of exp(-1). Eq. 4.1 holds true as long as the changes in the refractive index are not too large (e.g. use of aqueous solutions). The integral can be split into two parts (for surface binding and "bulk response", respectively) if we assume that a molecule binds somewhere in the region between $z = 0$ and $z = d$ (denotes the thickness of the film) and a significant "bulk response" exists where $z > d$:

$$\begin{aligned}\Delta\Theta_{SPR} = &\frac{2S_{SPR}}{\delta}\left[\Delta n\int_0^{d} exp\left(-\frac{2z}{\delta}\right)dz\right.\\ &\left.+\Delta n_0\int_d^{\infty} exp\left(-\frac{2z}{\delta}\right)dz\right]\end{aligned} \tag{4.2}$$

where Δn is the change in refractive index within the film due to molecule binding and Δn_0 is the change in refractive index due to injection of bulk molecules. The parameter Δn_0 can be estimated through the TIR angle as shown in the following equation:

$$\Delta n_0 = \frac{\Delta\Theta_{TIR}}{S_{TIR}} \tag{4.3}$$

where S_{TIR} is the TIR angle sensitivity (similarly to the SPR angle). If eq. 4.3 is inserted in eq. 4.2, the edited SPR signal ("bulk effect" is subtracted) is then formulated as:

$$\Delta\Theta^{*}_{SPR} = \Delta\Theta_{SPR} - \Delta\Theta_{TIR}\frac{S_{SPR}}{S_{TIR}}exp\left(-\frac{2d}{\delta}\right) \tag{4.4}$$

4.3 PEG interactions with Lysozyme

As previously mentioned in subsection 2.1.5, disagreements whether PEG is truly antifouling for proteins exist. While possibly being

resistant to proteins such as albumin, PEG might not be as resistant to other proteins such as lysozyme (LYZ) [122, 130]. To test whether an interaction with PEG and LYZ exists (and if yes, how strong it is), we employed multi parameter SPR and previously described "bulk effect" subtraction method (section 4.2).

To verify the PEG and LYZ interaction we measured the shifts in SPR and TIR angle upon protein injection and compared them with the signals achieved from the injections of BSA, which should not interact with the brush [58, 113, 295]. On the right hand side of fig. 4.3 it can be seen that the SPR and TIR angle shifts for BSA are basically the same and happen due to non-interacting bulk proteins. This can be explained by the fact that the PEG brush with thickness d is impenetrable for that protein, making a certain volume unavailable for it. However, for LYZ, the SPR signal is larger than TIR because it is interacting with the film (note that the concentration of BSA and LYZ are the same, thus the TIR angles are almost identical due to similar molar refractivities [296]).

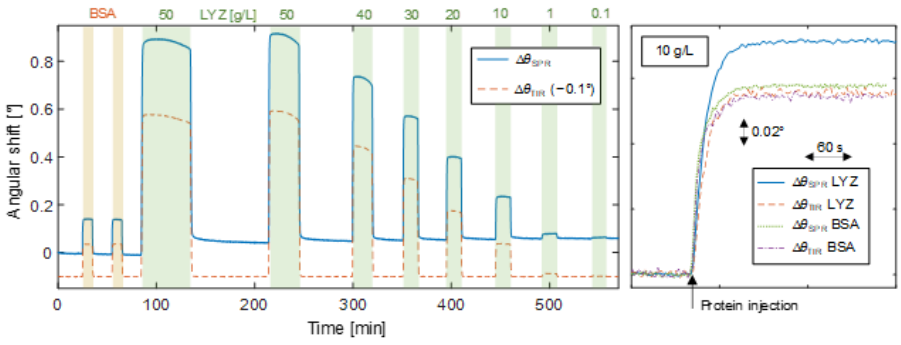

Figure 4.3: An SPR sensogram showing BSA (10 g/L) and LYZ (different concentrations) protein injections over PEG film, where the "bulk effect" is still present. An offset TIR angle shift is also included in the sensogram. To the right, TIR and SPR signals are compared upon BSA and LYZ (10 g/L for both) injections. (Irreversibly bound LYZ was already saturated after the first 50 g/L injection as seen in the sensogram.)

The "bulk effect" significantly contributes to the SPR angle as shown in fig. 4.3, therefore the affinity analysis of the reversible binding of LYZ to PEG may become inaccurate.

The equilibrium affinity between the PEG film and LYZ was estimated by using a Langmuir model, where the SPR signal from bound protein molecules is proportional to the surface coverage Γ. The equilibrium formulation is expressed by:

$$\Gamma = \Gamma_{max} \frac{C}{C + K_D} \tag{4.5}$$

where Γ_{max} is the saturated LYZ coverage on the PEG brush and C is the concentration of solute molecules. As noticed in fig. 4.3, the injection of 50 g/L LYZ resulted in an irreversible signal. To avoid contribution from this, we have only taken the SPR angle shifts from the injections, which are fully reversible (i.e. the dissociation phase upon rinsing the surface with the running buffer).

Three different techniques, which account for the "bulk effect", have been investigated: no subtraction, the commercially available software method made for the instrument and our analytically described formulation (eq. 4.4). All the necessary components found in our analytical solution were determined independently and can be found described more in detail in the paper [2].

As can be seen in fig. 4.4, our "bulk contribution" correction technique yields SPR angle shifts upon injecting LYZ (different concentrations), which can be reasonably fitted with the Langmuir isotherm. If no correction in the SPR angle shifts is applied, they keep on increasing to unacceptable values. Moreover, if the commercial correction tool made for the instrument is used (which subtracts the SPR angle shift with $\Delta\Theta_{TIR} \cdot S_{SPR}/S_{TIR}$), the shifts become negative, which are even more untrustworthy. This is because the film thickness factor is not included in the subtraction, rendering the method fitting only for very thin layers or protein adsorption on non-functionalized surfaces.

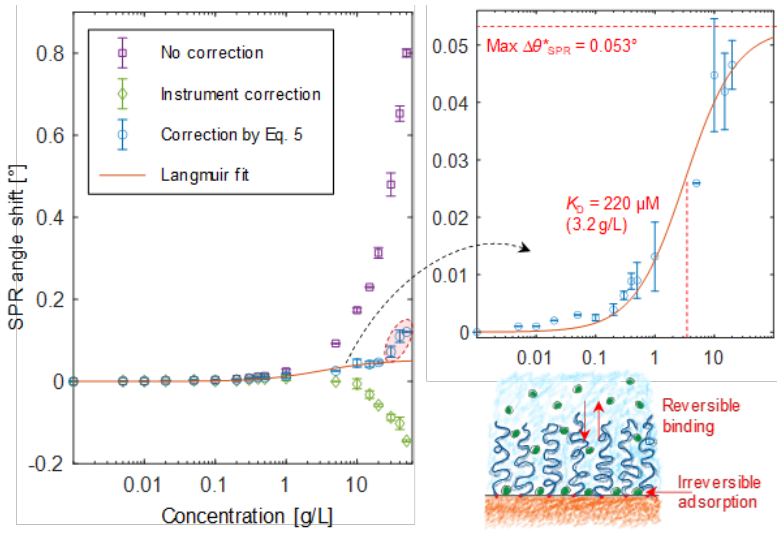

Figure 4.4: Equilibrium analysis of PEG and lysozyme interaction. The SPR angle shifts are extracted from reversible protein interactions with the film. The graph also indicates different techniques and the consequences of using each to subtract the "bulk effect". A Langmuir isotherm is shown in the graph to the right, indicating a correct way to remove the "bulk effect" and determine the dissociation constant for the interaction of interest (30 - 50 g/L lysozyme concentrations are excluded from this plot). The error bars stand for two standard deviations.

For high concentrations (>20 g/L), some deviation from the Langmuir model is observed and attributed to possible LYZ cluster formation [297, 298]. This is also indicated by the slow change in TIR angle shifts during the high concentration protein injections with time, suggesting some processes taking place in the bulk (fig. 4.3). Indeed, if LYZ proteins are not present in monomeric form, the Langmuir model is not expected to apply anymore, therefore the protein concentrations above 20 g/L are excluded from the calculations.

After fitting the data with Langmuir model (fig. 4.4), we deducted the affinity constant K_D (=k_{off}/k_{on}) equal to 220 μM (~200 μM if LYZ purity is taken into consideration) for these 20 kDa PEG-SH grafted brushes.

In order to evaluate if the applied model describes the LYZ binding rate to PEG, first-order Langmuir differential equation for reaction kinetics can be used:

$$\frac{\delta\Gamma}{\delta t} = k_{on}C(t)[\Gamma_{max} - \Gamma(t)] - k_{off}\Gamma(t) \tag{4.6}$$

C can be determined by employing the TIR angle shift (in this case it has to be assumed that there is no concentration gradient perpendicular to the surface) with the following equation:

$$C(t) = C_0 \frac{\Delta\Theta_{TIR}(t)}{\Delta\Theta_{TIR}(t) \rightarrow \infty} \tag{4.7}$$

where C_0 is the injected protein concentration in solution. Eq. 4.7 may be used to solve eq. 4.6 if the equilibrium is achieved significantly faster than the bulk concentration changes (i.e. represents the liquid exchange process). Pseudo-kinetics are established in the system according to eq. 4.5:

$$\frac{\Gamma(t)}{\Gamma_{max}} = \frac{\Delta\Theta^*_{SPR}(t)}{max(\Delta\Theta^*_{SPR}(t))} = \frac{C(t)}{C(t) + K_D} \tag{4.8}$$

By applying this, we have concluded that equations 4.7 and 4.8 fit the reaction kinetics well (i.e. by correctly removing the "bulk contribution" and then estimating $C(t)$. However, it was found that the determined k_{on} and k_{off} are too high to cause a delay in the LYZ binding/unbinding events. Thus, $\Gamma(t)$ is dependent on the system's liquid exchange mechanism (takes ~30 seconds for relatively small flow rates), leading to inaccurate kinetic process analysis when fitting the Langmuir model to sensograms with $\Delta\Theta^*_{SPR}$. Nevertheless, the valid interpretation of $(k_{on}C + k_{off})^{-1}$ and k^{-1}_{off} is that they are faster than the liquid exchange time inside the SPR instrument flow cell (~30 seconds), which means that k_{off} > 0.033 s^{-1}.

4.4 Protein transport gating with PNIPAM polymer brush functionalized nanowells

In these results, we report an innovative concept of controlled gating of protein transport and trapping with solid state nanowells, which are functionalized with thermo-responsive PNIPAM polymer brushes acting as molecular gates. The polymer brush conformational change from swollen to collapsed is facilitated with a local application of electrical current, which induces temperature increase on the surface. When the polymers are collapsed (i.e. the

gate is open), the proteins diffuse to the interior of the nanowells and adsorb on silica. Consequently, the nanowell opening can be closed when the local temperature reaches below PNIPAM LCST and the proteins may be repelled from the interior walls via change in pH, yet still stay trapped inside. When compared to other systems used for biomolecule confinement (mentioned in the chapter 1), our method offers significant advantages, which are - hundreds (or a few, if needed) of proteins can be trapped at once in a tiny volume (attoliter range) and the liquid inside the nanocompartments may be easily exchanged while the proteins are still trapped. In addition, the time proteins spend trapped inside the nanowells is way higher than the time until the fluorophore bleaches (~1 minute [299] with respect to illumination needed for single molecule detection), the experiments can be run at physiological conditions and no forces are acting upon the proteins, which means that the method is not invasive.

In order to prove that PNIPAM polymer brushes block proteins below the LCST and allow translocation into the interior of the NWs above LCST, BSA protein adsorption to silica (i.e. the interior of the nanocompartments) was investigated. The running buffer pH was lowered to pH = 5.5 - 6.0, which results in less negatively charged BSA (isoelectric point is 4.5 - 5.4 [300–302]) and a smaller repulsion between the protein and silica. Supporting control experiments showing BSA adsorption and desorption with pH changes on a non-coated silica surface and PEG coated nanowells (monitored by QCM-D and real-time plasmonic shift tracking, respectively) may be found in the attached preprint (**paper IV**).

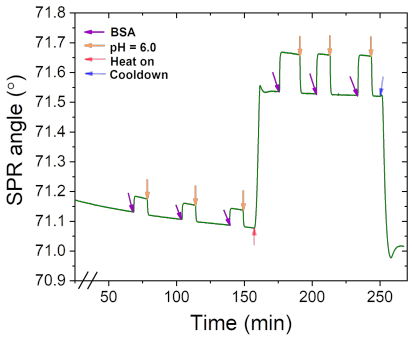

Figure 4.5: BSA protein injections on PNIPAM coated gold sensor below and above PNIPAM LCST measured by SPR.

We emphasize that we have not observed BSA adsorption on collapsed PNIPAM polymer brushes as reported in some previous studies [134, 303]. An evidence for this is the SPR experiment (fig. 4.5), where BSA is injected below and above PNIPAM LCST and the SPR angle shift is reversible upon rinsing with the running buffer. The reason for the high protein repelling properties could be related to the grafting density of the PNIPAM film, which we assume to be equal or higher than for similar thickness PEG grafted films mentioned before (i.e. ~0.25 nm^{-2}) [219].

In figure 4.6, a full gating procedure of BSA transport with PNIPAM functionalized nanowells is shown as Dip plasmonic shift is tracked in time (neutravidin protein trapping was performed as well, but will not be presented). BSA is injected below and above PNIPAM LCST (i.e. the polymer brushes are in the extended or collapsed states, accordingly) and as seen, no protein adsorption happens when the polymer brushes are in the swollen state as the plasmonic shift does not increase. This is because the polymer brush extended height is high enough to block the opening of the nanocompartments (diameter ~120 nm). In contrast, when the temperature on

the surface is raised by applying resistive heating and PNIPAM collapses, BSA proteins adsorb in the interior of the nanowells shown by an increased Dip plasmonic shift.

When the pH is raised to pH = 8.5 at RT, a plasmonic shift decrease is observed, which possibly indicates protein desorption from silica. However, the signal does not reach the baseline value before collapsing the polymer brush at ~5000 seconds, meaning that the biomolecules stay inside the interior of the nanowells. Further on, when PNIPAM brushes are collapsed again at high pH, proteins are released from the nanocompartments as indicated by the diminished plasmonic shift to the baseline (or at least comparable due to baseline drift of ~0.1 nm in 1800 seconds).

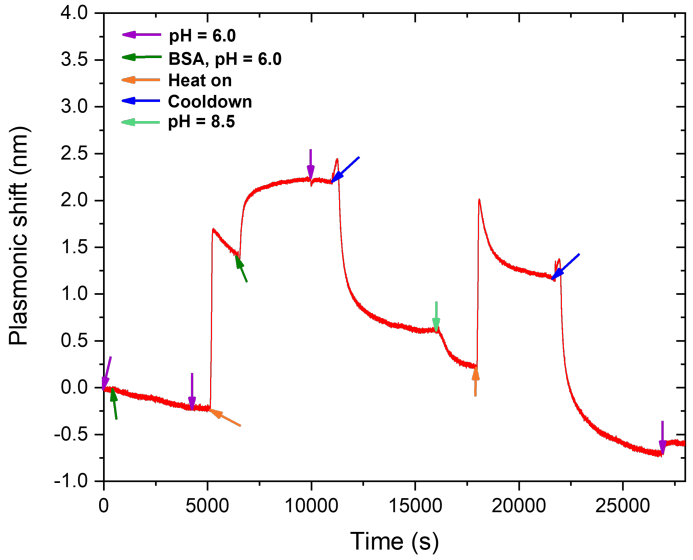

Figure 4.6: BSA transport gating with PNIPAM coated NWs monitored with real-time plasmonic shifts in the Dip.

Additional fluorescence experiments under an optical microscope were carried out to further support BSA transport gating and trapping with PNIPAM functionalized nanowells, and can be seen in figures 4.7 (many nanowells) and 4.8 (single nanowells). Similarly to real-time plasmonic shift experiment (fig. 4.6), the local temperature increase to collapse PNIPAM polymer brushes was facilitated by applying voltage through the glued copper wires on the nanowell surface (fig. 4.7 a). A sample with half-nanowell, half-gold covered surface was used in order to retrieve the fluorescence intensity coming directly from Alexa Fluor 488^{TM} - BSA (AF488-BSA) proteins trapped in the interior of the nanowells (fig. 4.7 b). Therefore, the signal intensity coming from the gold side was subtracted from the nanowell side during all experiment events (described more in detail in subsection 3.2.10).

In fig. 4.7 c), the difference in fluorescence intensity between the two sides on the PNIPAM functionalized surface is shown. After injecting AF488-BSA at pH = 6.0 at RT (step II), small fluorescence signal is retained after the bulk molecules are rinse away, possibly

indicating that some nanowells might not have thick enough brush at the pore opening to prevent proteins from adsorbing in the interior. A much larger fluorescence intensity is achieved (step III) after the fluorescently tagged BSA is injected while heating the surface (i.e. PNIPAM polymer brush is collapsed). The intensity stays roughly the same when the polymer brush is swollen again and the pH is raised to pH = 8.5 (step IV; i.e. the protein desorbs from the silica due to increased negative charge), suggesting that AF488-BSA proteins are trapped inside the nanowells. At the last step of the experiment (step V), when the proteins have been released from the interior of the nanowells due to collapsed PNIPAM polymer brushes at high pH, the small fluorescence signal is left and comparable to the intensity in step II. The reason for this could be that some AF488-BSA proteins adsorbed irreversibly on some gold regions on both sides or because the transmission of light is higher through the nanowells. Nevertheless, the fluorescence experiment complements the extinction measurement and proves that the designed system for protein transport gating and trapping works as expected.

To study single or a few protein conformational changes or interactions with others, the system had to be reduced to individual nanowell coverage (i.e. separate nanowells may be seen on the surface compared to the case in fig. 4.7 b) and monitored by fluorescence readout. Additionally, performing experiments with single nanowells is advantageous as they provide information about differences in the nanostructure trapping ability individually (i.e. some deviation in the nanowell diameter and polymer brush thickness may result in trapping/non-trapping of biomolecules). To illustrate this, we performed fluorescence gating experiments with AF488-BSA and sparsely covered nanowell surfaces, and compared the positions of nanowells with fluorescent readout (when AF488-BSA is trapped in the interior of the nanostructures) with nanowell spots observed by dark field imaging.

In fig. 4.8 such an experiment is demonstrated, where the gating and trapping of fluorescently labelled BSA molecules are done in the same manner as described in the previous full nanowell coverage fluorescence and real-time plasmonic shift monitoring experiments. Around 99% of the spots correlate to the ones seen in the dark field image when AF488-BSA is injected above PNIPAM LCST and ~93% are left after increasing the pH to 8.85 at RT. This suggests that most of the proteins are prevented from leaving the interior of the nanowells by the extended PNIPAM polymer brushes. However, some proteins (~14% of all bright spots observed, which correlate with the spots in the dark field image) "leak into" nanowells when injected at room temperature meaning that a fraction of nanowells might not have thick enough brushes in their

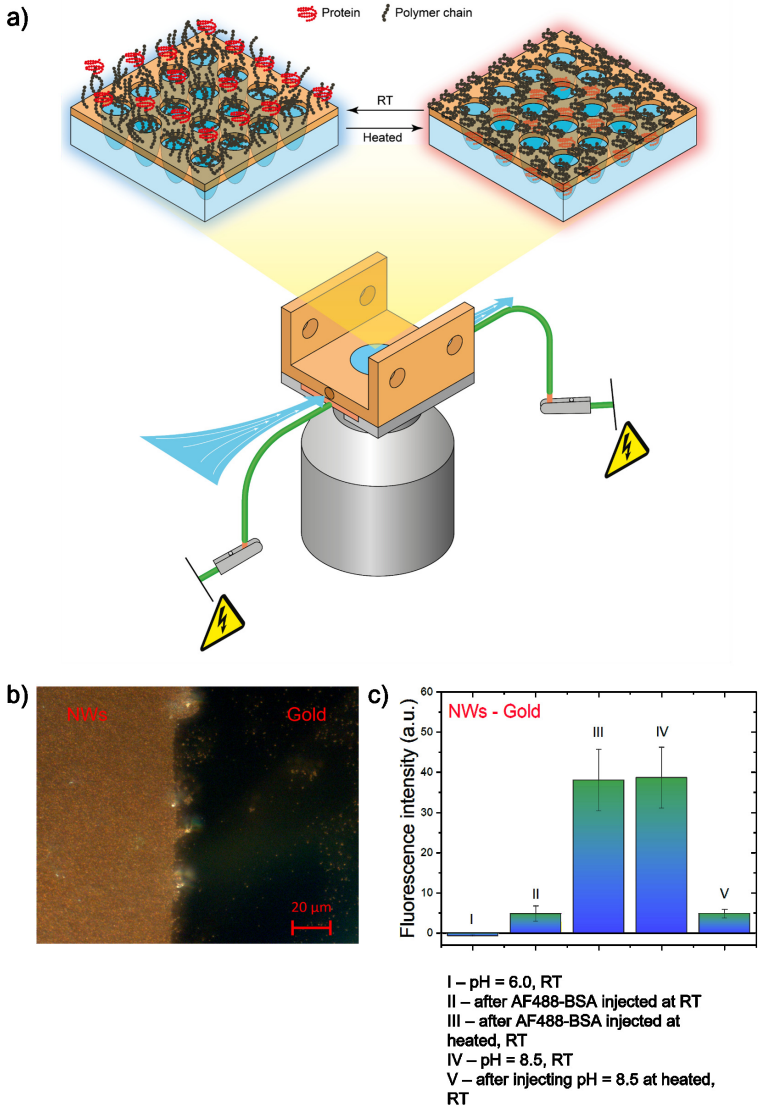

Figure 4.7: Alexa Fluor 488^{TM} labelled BSA transport gating with PNIPAM coated NWs monitored by optical microscopy. a) An illustration of fluorescently tagged BSA transport gating experiment. The sample surface is heated by resistive heating via attached electrodes on conductive glued wires and the introduction of protein is facilitated by a peristaltic pump through the flow cell. b) A dark field image of half nanowell - half gold surface (taken with Axiocam). c) Subtracted fluorescence intensity (gold side from the NWs), resulting in BSA trapping in the interior of the nanowells.

vicinity (i.e. the uniformity of the film is not ideal over large sample areas). Another possible explanation is that these AF488-BSA molecules adsorb irreversibly on defects or contaminations on the surface due to some of the bright spots in the fluorescent images do not correlate with the nanowell positions in the dark field figure. Nevertheless, we show that the trapping time of AF488-BSA proteins is significantly higher than for most tether-free techniques such as optical or electrokinetic traps. Also, it is much longer than the photobleaching of the fluorescent dye, which was investigated by raising the exposure to light (not shown here). Finally, even though more detailed study of the trapping time is challenging due to photobleaching, the nanowells coated with sufficiently thick PNIPAM polymer brushes show great protein trapping capability with a controlled gating mechanism.

After it was shown that BSA proteins can be trapped and released on demand as a proof of concept, it was necessary to investigate

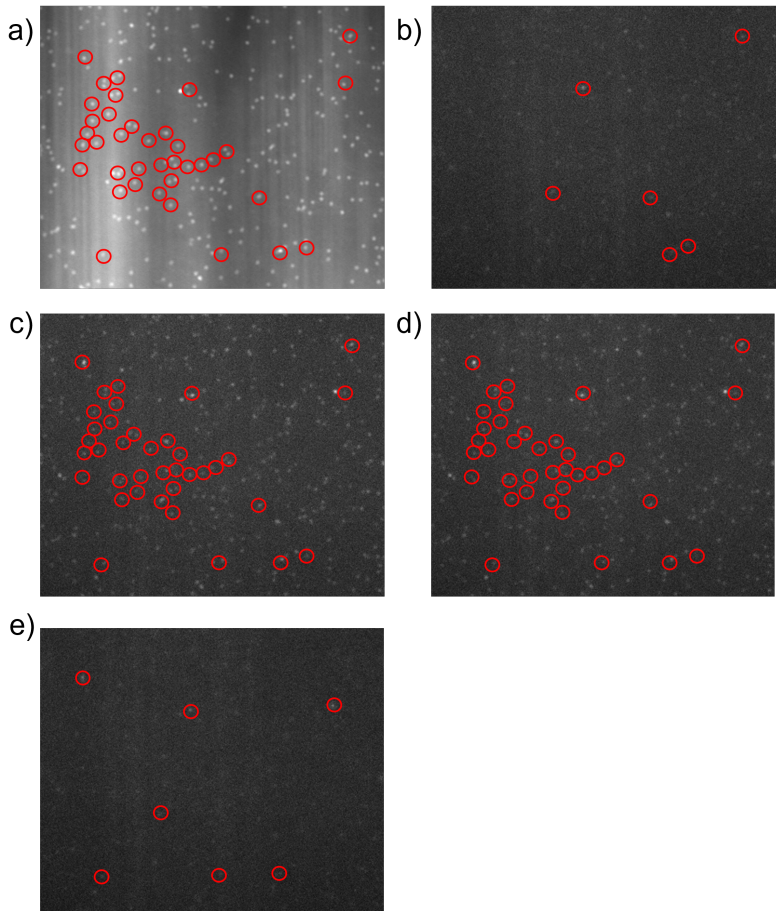

Figure 4.8: Optical microscopy images of Alexa Fluor 488^{TM} - BSA transport gating events in PNIPAM coated NWs. a) A dark field images with an Andor CCD camera, indicating single NWs. b) After injecting AF488-BSA at below PNIPAM LCST, pH = 5.92. c) After BSA was injected at PNIPAM collapsed state, pH = 5.92. d) pH is raised to 8.85 at room temperature. e) An image taken after AF488-BSA is released by collapsing the polymer brushes again, pH = 5.92. Red circles indicate some of the correlating spots between the nanowells imaged in fluorescence mode and dark field image of nanostructures.

whether smaller molecules (<1 kDa) may enter the interior of the nanowells through the extended state polymer brush freely. In fig. 4.9 a fluorescence experiment is presented, where nanowells with or without 3-aminopropylsilatrane (APS) molecules in the interior (functionalization protocol may be found in section 3.2.9) are exposed to sulfo-cyanine 3 nhs-ester, which binds to primary amine moieties. When the dye is exposed to swollen state PNIPAM polymer brush nanowells without the APS molecules in the interior, no retained fluorescence signal is observed after rinsing. However, when APS molecules are present inside the nanowells, sulfo-cyanine 3 nhs-ester molecules diffuse through the hydrated brush and bind to them as indicated by the retained fluorescence intensity. This shows that the designed nanostructure platform could be used as a potential filter for molecules of various sizes as well.

Later on, we have hypothesized that the dye molecules might not penetrate the collapsed PNIPAM polymer brush barrier on the nanowells as it is hydrated to a much lesser extent, thus a similar experiment was performed (preliminary result, therefore not shown here). However, it was observed that sulfo-cyanine 3 nhs-ester binds to the APS molecule functionalized nanowell interior when the polymer brushes are collapsed as seen from the fluorescence readout. This indicates that either the polymer brush

film was too thin or the hydration extent was sufficient for the dye molecules to diffuse through (due to time constraints, we did not investigate this event further).

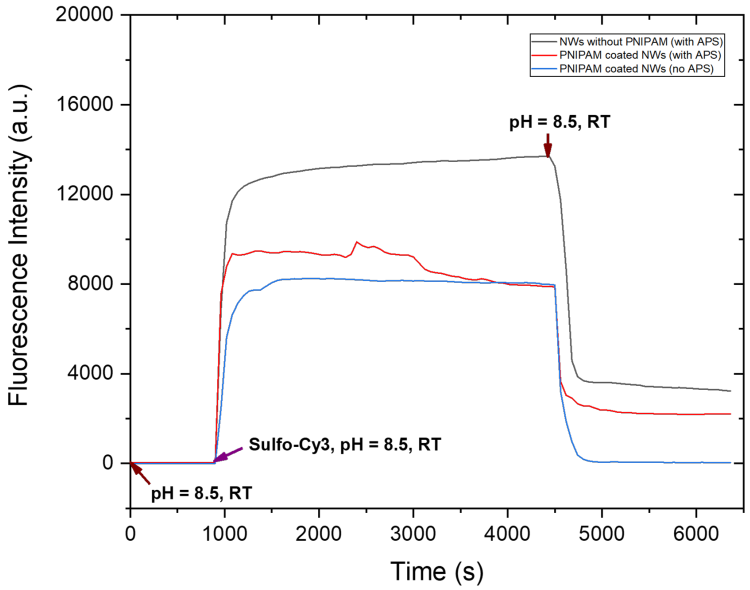

Figure 4.9: Sulfo-cyanine 3 nhs-ester dye adsorption in the interior of non-coated or PNIPAM polymer brush functionalized nanowells. (511 nm illumination, 100 ms exp. time, 250 EM gain; excitation bandpass filter = 511/44 and emission bandpass filter = 555/25)

An overview of unpublished results

5

In this section, results, which do not appear in the publication list, will be presented and discussed. They include plasmonic shifts above PNIPAM LCST from polymerizations with DTBU and TBU initiators, BSA adsorption and/or desorption experiments with QCM-D and real-time plasmonic shift monitoring, and MQ water flow tests through non-functionalized and PNIPAM coated nanopores (or membranes).

5.1 PNIPAM polymer brush collapse plasmonic shifts of DTBU and TBU initiated surfaces

As mentioned previously in the section 2.4, it is possible to track Peak and Dip plasmonic shifts for biomolecular adsorption/desorption events due to refractive index changes in the local plasmonic field. In addition, plasmonic shifts may give an understanding about a relative film thickness if the required parameters are known.

In the case of PNIPAM polymer brush collapse above its LCST, the plasmonic shift increases, because the water is expelled from the vicinity of the film, consequently increasing the local refractive index. From this, an approximate PNIPAM polymer brush extended/collapsed thickness (i.e. if either one is determined independently by other methods) may be estimated from an expanded version of equation 2.31. It takes into account the surface plasmon sensitivity S, plasmonic field decay length δ, film thickness d (in this case H_{ext} and H_{col} the height of extended and collapsed state brush), refractive index changes in extended and collapsed states of polymer brush film n_{ext} and n_{col} and plasmonic shift upon collapsing the brush (denoted as $\Delta\lambda_{col}$ - $\Delta\lambda_{ext}$; delta symbol indicates comparison with an empty surface) [233]:

$$(\lambda_{col}-\lambda_{ext})/S = n_{col}-n_{ext}+\Delta n_{ext}e^{(-H_{ext}/\delta)}-\Delta n_{col}e^{(-H_{col}/\delta)} \quad (5.1)$$

here Δn_{ext} and Δn_{col} are the differences between bulk and polymer brush film refractive indexes in extended or collapsed conformation, accordingly (delta symbol denotes the RI difference from the solution). For 120 nm diameter nanowells (with 30 nm gold thickness and $\sim$ 100 nm in depth), the sensitivity parameter S is

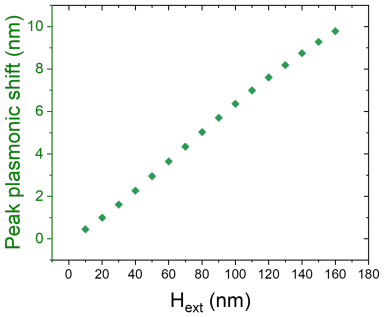

Figure 5.1: Peak plasmonic shift plotted as a function of polymer brush extended state height

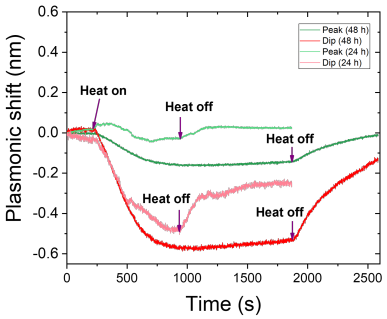

Figure 5.2: Peak and Dip plasmonic shift upon heating PNIPAM coated nanowell surface (polymerized in pure MeOH).

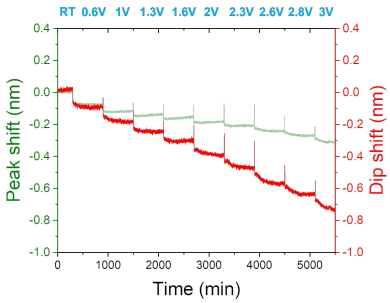

Figure 5.3: Real-time tracking of Peak and Dip plasmonic shifts of heating cycles on an empty nanowell surface.

reported to be ~147 and ~278 nm per RI unit for Peak and Dip, accordingly, [56], and the decay length is ~50 nm [233].

Even though, H_{col}, H_{ext} and the refractive indexes of the film in the extended or collapsed states are unknown, and the other parameters might vary slightly between nanowell surfaces, it can be approximated that the higher the plasmonic shift is, the thicker the polymer brush film is grafted (assuming the grafting density of the coating is constant). As an example of this, in figure 5.1, it can be seen that the Peak plasmonic shift is increasing with higher polymer brush swollen height values. In this case, H_{ext} is chosen as a variable and H_{col} is assumed to be ~ 1/3 of H_{ext} (n_{col}, n_{ext} and n_{bulk} (i.e. RI of solution) are chosen to be 1.5, 1.38 and 1.34, respectively).

Due to the fact that plasmonic shifts allow to roughly estimate how thick the polymer brushes are, the following results will include some Peak and Dip plasmonic shifts upon collapsing PNIPAM polymer brushes (produced by varying either the polymerization time or MQ water v%) on nanowell surfaces. Also, all the plasmonic shifts, which were acquired with different polymerization conditions throughout the thesis can be found in the Appendix C.

As mentioned in subsection 3.2.6, two initiator molecules have been used to synthesize PNIPAM via ARGET-ATRP on surfaces - HS-C_{11}-OC(O)-IzoButyrate-Br (TBU) or Bis[2-(2-bromoisobutyryloxy)undecyl] disulfide (DTBU). Both of these molecules are similar, except TBU is a thiol and DTBU is a disulfide.

Firstly, PNIPAM polymerization on nanowells, was attempted in pure MeOH, which is a good solvent for PNIPAM. Upon heating the surfaces above PNIPAM LCST (fig. 5.2) at ~300 seconds in a real-time plasmonic shift monitoring eperiment, plasmonic shifts in Peak and Dip turned to negative values instead of an expected increase. The blue shift upon heating can be explained by the fact that water decreases its RI upon heating (fig. 5.3). Therefore, it was concluded that for PNIPAM polymerizations in MeOH there is either no polymer brush layer at all or it is very thin (i.e. not suitable to be an entropic barrier for proteins).

To promote polymer brush growth, MQ water was included in the following polymerizations [112, 304, 305]. As seen in fig. 5.4 a), by increasing MQ v% and keeping the polymerization time 24 hours (with DTBU initiated surfaces), the plasmonic shift in Peak and Dip upon collapsing PNIPAM polymer brushes generally increase as well, possibly resulting in a thicker brush film (note that in this plot several green and red circles for the same v% indicate different polymerization batches). However, even though the plasmonic shifts increase with higher v% for 24 hours polymerization, the

brush layer might be too thin to block (i.e, the plasmonic shift in Peak and Dip are too small), e.g. BSA, from translocating in the swollen state to the interior of the nanowells.

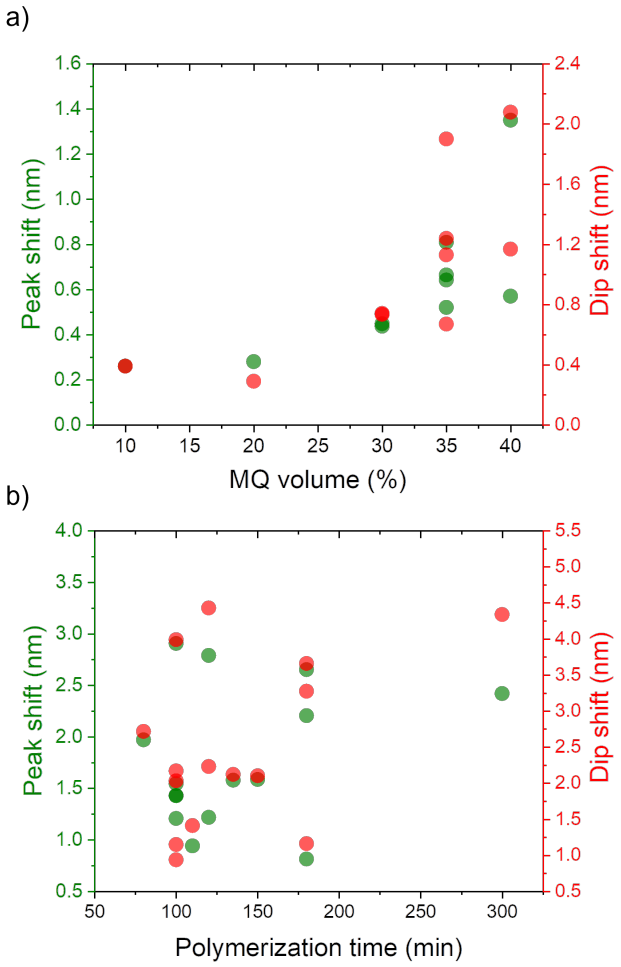

Figure 5.4: Peak and Dip plasmonic shifts upon increasing PNIPAM functionalized surface temperature above polymer LCST against polymerization time (b) and MQ water v% (a). a) DTBU initiated PNIPAM (polymerized for 24 hours) coated NWs. b) DTBU initiated PNIPAM functionalized NWs with 45v% MQ water (rest is MeOH). Green and red circles are for Peak and Dip shifts, respectively.

Similar Peak plasmonic shift (~1.2 nm upon collapse) is achieved with TBU (thiol) initiated PNIPAM polymer brushes (fig. 5.5) and when BSA is injected at RT at ~2000 seconds, translocation of the protein to the interior of the nanowells follows (i.e, Peak and Dip plasmonic shifts increase).

It is known that 24 hour polymerization time is rather long when compared to typical ARGET-ATRP reactions, which take minutes or hours [112, 304, 305]. Therefore, the MQ v% was increased further in order to reduce the polymerization time and have a thicker brush layer at the same time (fig. 5.4 b). However, the trend here is not as clear as one could expect as even for the same polymerization time, say 100 minutes, the Peak plasmonic shift ranges from 1.207 nm to 2.907 nm for different batches, probably indicating a high irreproducibility of polymer brush thickness (the same is for Dip plasmonic shift). In addition, it was noticed that when MeOH and MQ water ratio is close to 1:1 (v/v%; like with 45v% MQ water), the polymerization solution during the

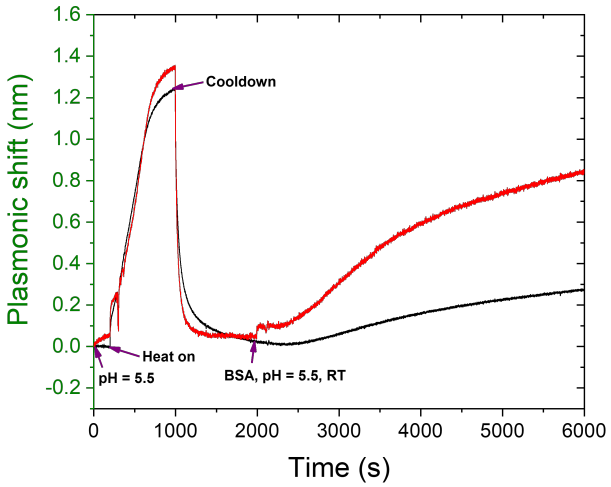

Figure 5.5: Peak and Dip plasmonic shift upon polymer collapse tracking in real-time with TBU initiated 45v%MQ PNIPAM polymer brush functionalized nanowells (20 min polymerization time).

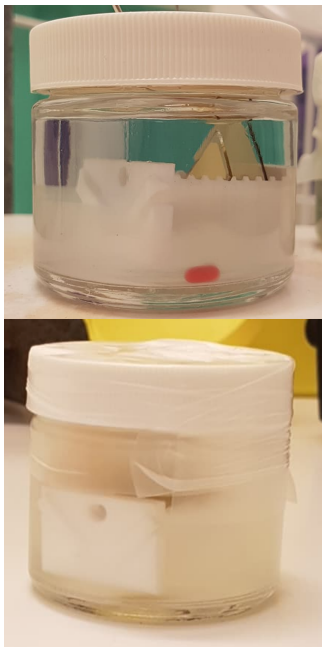

Figure 5.6: Turbid PNIPAM polymerizations solutions during ARGET-ATRP. MeOH volume fractions are between 0.25 and 0.5 in this case.

reaction becomes turbid (fig. 5.6). This can be explained by the phase diagram of PNIPAM bulk solutions, where at 21 °C and having MeOH volume fraction between 0.25 and 0.6, the solution with PNIPAM, water and methanol is expected to be turbid (i.e. a solvent mixture of water and methanol together is a poor solvent for PNIPAM) [160]. Indeed, if the polymerization mixture contains a fraction of initiator molecules, even during ARGET-ATRP on surfaces this effect cannot be avoided. One of the possible reasons why there might be some bulk DTBU initiator molecules is because disulfides can form multilayers on gold, which could partially disintegrate during the reaction and produce bulk entities [306].

A solution for solving the polymerization phase separation issue was to introduce TBU (thiol) initiated ARGET-ATRP reactions (i.e. make the polymerization mixture during the reaction transparent instead). Even though it was successful, the Peak and Dip plasmonic shift deviation for the same polymerization time did not improve significantly as seen fig. 5.7 a) and b) when compared to fig. 5.4. For example, in plot b) it is shown that for 30 minute polymerization time (45v%MQ) Peak plasmonic shift varies from 0.936 to 3.315 nm. In addition, in graph c) for 70v% MQ water the decreased plasmonic shift for Peak instead of an expected increase suggests that due to poor solvent conditions for PNIPAM during the reaction the brushes are not growing as fast as compared to the reaction with MQ water content below 45v%.

For future reactions, 39v% MQ water content was chosen in the solvent mixture as a candidate as at least it produces an increasing trend of Peak plasmonic shifts with increasing polymerization time. Also, as shown in previous results (**paper IV**, supplementary information), SPR height probing results demonstrate that 39v%MQ water in the solvent mixture with different polymerization times

yield brush thicknesses, which are within good margin of deviation for gating protein transport experiments.

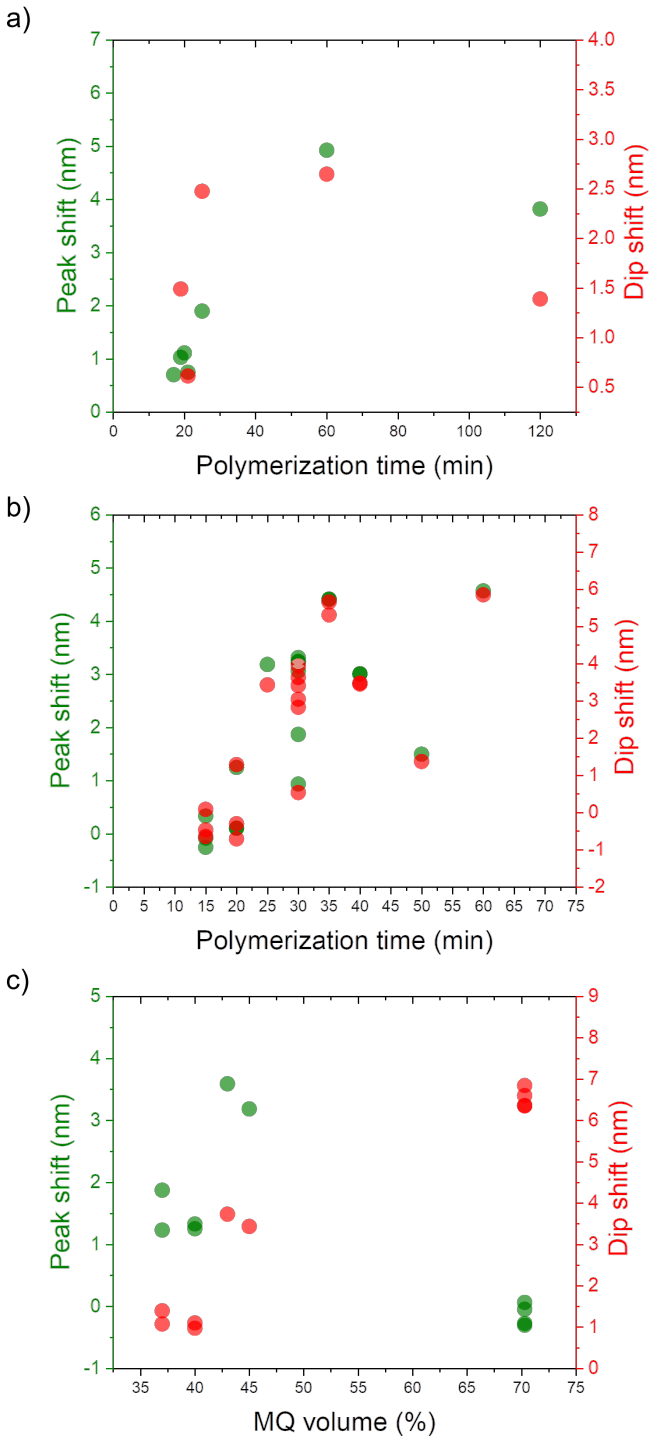

Figure 5.7: Peak and Dip plasmonic shifts upon increasing PNIPAM functionalized surface temperature above polymer LCST against polymerization time (a) and b) and MQ water v% (c). a) TBU initiated PNIPAM coated NWs with 39v% MQ water (rest is MeOH). b) TBU initiated PNIPAM functionalized NWs with 45v% MQ water. c) TBU initiated PNIPAM (25 min polym. time) functionalized NWs. Green and red circles are for Peak and Dip shifts, respectively.

5.2 BSA adsorption/desorption experiments with QCM-D and real-time plasmonic shift monitoring

In this section, BSA reversible and irreversible adsorption will be presented on planar silica QCM-D sensors and on nanowells.

First of all, it is well known that BSA and other proteins may non-specifically bind to gold surfaces, possibly denaturing them [307, 308]. Therefore, to avoid this, a densely grafted polymer brush layer is a prerequisite in order to gate protein transportation as discussed in Chapter 1.

To facilitate protein adsorption within the interior of the nanowells, it was decided to employ BSA protein isoelectric point (IEP), which is reported to be in the range of pH = 4.5 - 5.4 [300–302]. In this case, the proteins should adsorb better at lower pH to the silica surface (i.e. interior of the nanowell), which is negatively charged. Moreover, because BSA aggregates at pH below its IEP [300, 302, 309], the pH during the protein adsorption was in the range of pH = 5.5 - 6.0. Also, to desorb the electrostatically bound BSA, a pH range of 8.1 - 8.5 was chosen, in which the protein should not be denatured or aggregated and still retain its native structure [310].

To illustrate all of the above, figures 5.8 and 5.9 of QCM-D experiments show BSA adsorption. However, an irreversible adsorption is sometimes evident even with respect to pH changes. For example, in fig. 5.8 a), BSA adsorption at pH = 5.5 (at 445 s) happens as the frequency shift decreases by -26.55 Hz (i.e. within the margin of a single protein monolayer [311]), but upon increasing the pH to either 8.3 (BBS buffer) or pH = 8.0 or 8.5 (PBS buffer), no desorption occurs, possibly indicating protein some structural change.

While possible denaturation or aggregation of BSA (purchased from *Sigma Aldrich*) was not studied any further, another batch of BSA from a different supplier (*Thermo Fisher Scientific*) was chosen to check if it behaves any different. In subfigures b) of plots 5.8 and 5.9, BSA (from a different supplier) adsorption at pH 5.5 and pH 6.0, and desorption at pH = 8.1 (at 5000 seconds; PBS buffer) occurs. For example, upon injecting BSA at pH = 6.0 at 300 s (fig. 5.9 b); frequency change upon protein layer saturation -23.05 Hz), followed by a rinse step at same pH (4154 s) and injection of pH = 8.1 (4870 s) proves that the IEP of BSA can be used to electrostatically desorb the protein (same for the case of adsorption at pH = 5.5, fig. 5.8 b). The reason, why the signal did not return to the baseline after the last pH = 6.0 wash step at 8726 s is possibly because of the

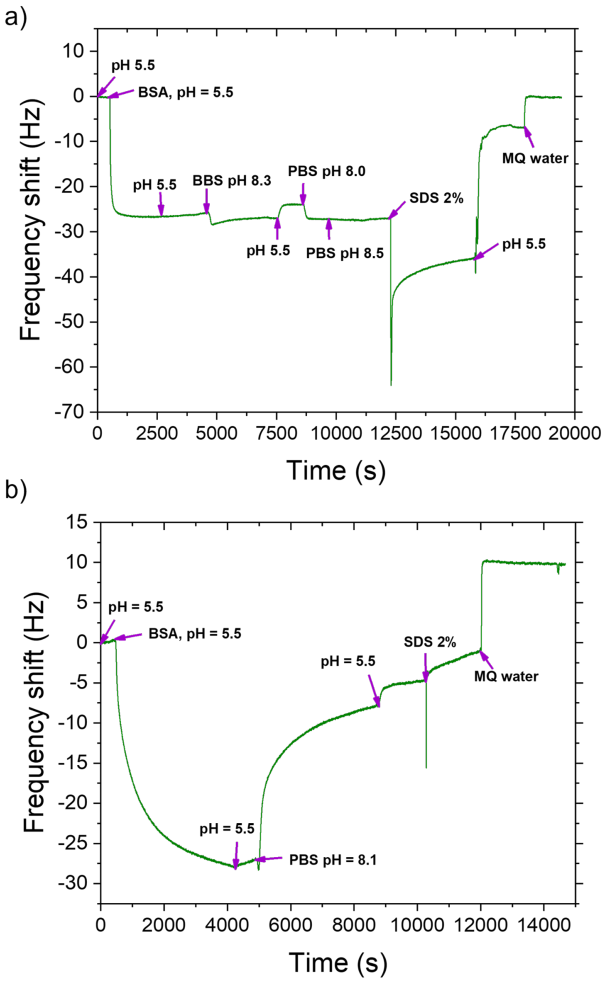

Figure 5.8: QCM-D experiments on irreversible (a) and reversible (b) BSA adsorption (5th overtone) at pH = 5.5 on SiO_2 chips.

impurities in the protein batch (the purity of the protein is 96%, in this case).

As a complementary experiment, real-time plasmonic shift monitoring of gating different supplier (from Sigma Aldrich (BSA (1) and from Thermo Fisher Scientific (BSA (2) BSA proteins was carried out (fig. 5.10). BSA (1) is injected below and above LCST of PNIPAM at 684 s and 3516 s, accordingly. While no plasmonic shift increase is noticeable for Peak in both cases, the Dip increases slightly (0.161 nm) when PNIPAM is in the collapsed state at 5342 s, indicating protein adsorption within the interior of some nanowells. Then, when BSA (2) is injected above LCST of PNIPAM at 12497 s, a much higher increase in plasmonic shift is noticed (0.389 nm and 1.225 nm for Peak and Dip, respectively), which means that BSA is adsorbed inside most of the nanowells (signal comparable to the control experiment in fig. 2.22; same measurement as BSA (1) was injected). Afterwards, when BSA (2) is injected again below LCST of PNIPAM at 28146 s, the protein adsorbs inside the nanostructures again (which also means that the polymer brush layer is not thick enough). The Dip plasmonic shift does not reach an equilibrium value after injecting high pH at above LCST as compared to the

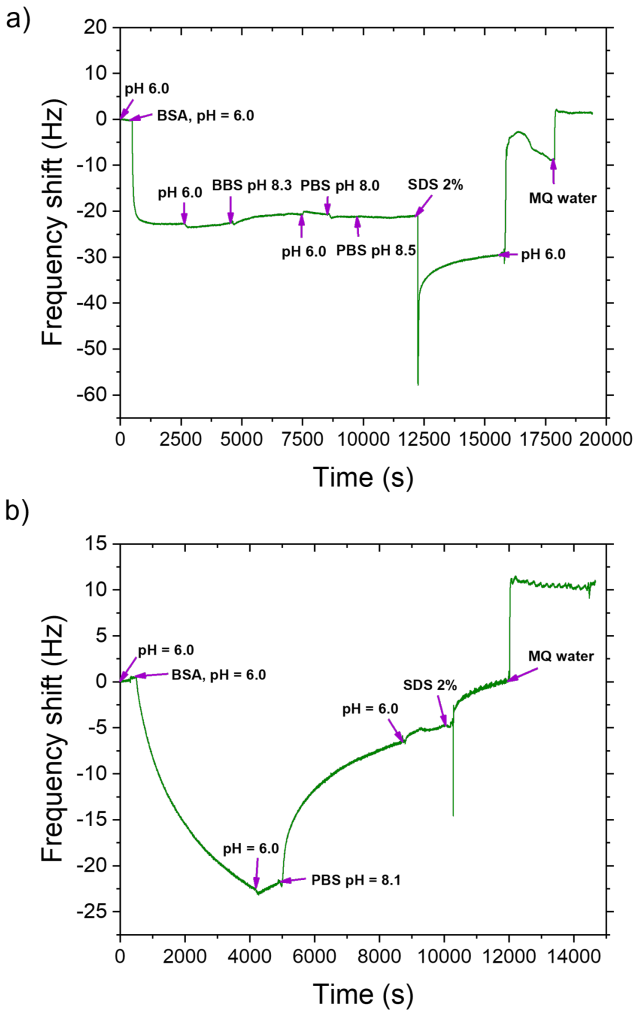

Figure 5.9: QCM-D experiments on irreversible (a) and reversible (b) BSA adsorption (5th overtone) at pH = 6.0 on SiO_2 chips.

Peak plasmonic shift (at ~25000 seconds), which results in a higher baseline value than before BSA (2) was injected.

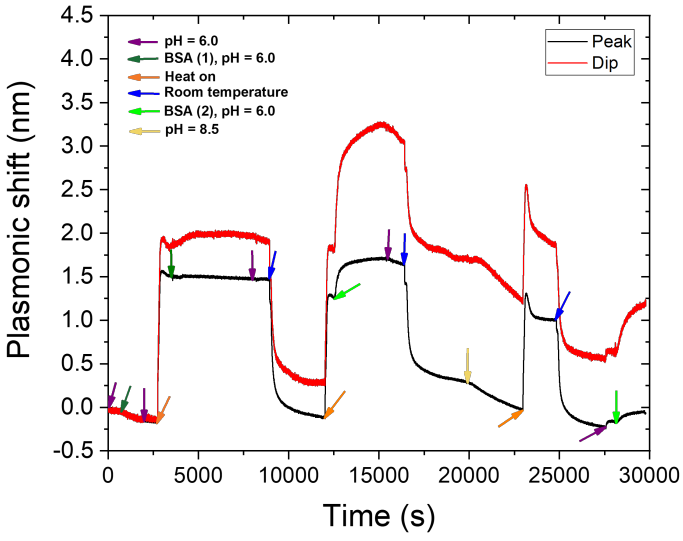

Figure 5.10: Plasmonic shift real-time BSA gating experiment with 2 different protein batches (marked as BSA (1) and (2) and PNIPAM functionalized NWs (39v% MQ; 15 min pol. time).

Finally, when the pH-reversible adsorption of BSA on silica has been established for the future gating experiments, it was necessary to find if pH range of 5.5 - 6.0 is optimal for adsorption. This means that the protein stays at the surface while rinsing with the running buffer. Indeed, upon rinsing for 10 minutes (this time frame was picked because of linearity in the desorption rate; figures 5.8 (b) and 5.9 (b), it can be seen that the frequency shift does not return to the baseline or it would take a significant amount of time to do it. On the other hand, when higher pH buffers are used (i.e. pH = 6.5 and pH 7.0, fig. 5.11 a) and b) after BSA injection at 4200 seconds, the frequency change within 10 minutes of rinsing is 1.67 Hz for BSA adsorbed at pH = 7.0, compared to 1.14 Hz for adsorption at pH = 6.0. These relatively higher desorption rates (0.034 and 0.027 Hz/s for pH = 7.0 and pH = 6.5, respectively) than for pH = 5.5 or pH = 6.0 (0.0165 and 0.028 Hz/s, accordingly) helped us choose the previously mentioned optimal range for further BSA transport gating experiments (pH below 5.5 has not been tested in order to avoid possible protein aggregation).

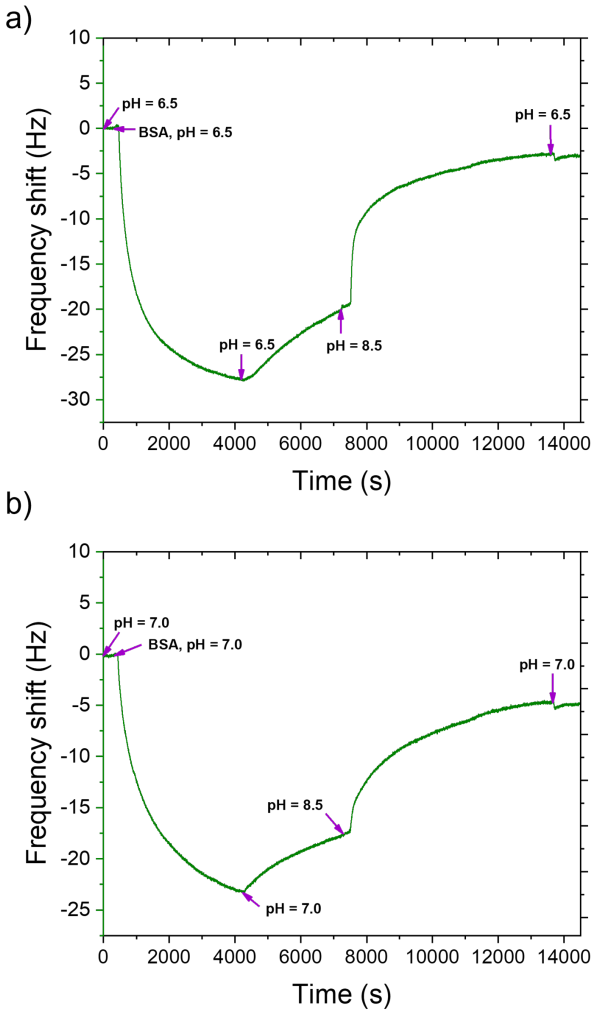

Figure 5.11: QCM-D experiments on reversible BSA adsorption (5th overtone) on SiO_2 chips.

5.3 Flow measurements on nanopore arrays

Further development of single biomolecule trapping platform led to use of nanopore channels, which could have polymer brushes on each side, thus facilitating gating either by stimuli-response or hydrodynamic forces (i.e. shear flow) [312]. In contrast to nanowells, these nanochannels have pores through the substrate and silica interior is replaced with SiN_x (fig. 5.12).

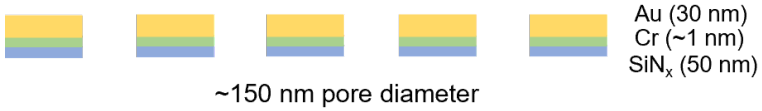

Figure 5.12: A schematic of nanopore arrays with periodicity of ~300 nm.

To begin with, in order to assess flow through the nanochannels, we assume that the Reynold's number (a dimensionless parameter, which describes the behavior of fluid flow) is lower than unity (laminar flow is dominant) as the length scale for nanosystems is small (e.g. if the characteristic velocity is 1 cm/s, Re number is $\sim 1 \cdot 10^{-9}$) [313, 314]. It can be expressed as a ratio between inertial and viscous forces:

$$Re = \frac{\rho \vec{v} L}{\eta} \tag{5.2}$$

here, ρ is the density of the liquid, $\vec{v}$ is characteristic velocity, L is the length scale of characteristic flow and η is dynamic viscosity of the liquid. In addition, when the Re parameter is close to 0, then inertial forces can be neglected and flow through a cylindrical channel at a pressure difference Δp described by a linear Stoke's equation:

$$\nabla p = \eta \nabla^2 \vec{v} \tag{5.3}$$

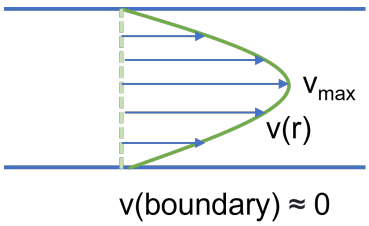

Figure 5.13: A schematic of Hagen-Poiseuille parabolic velocity profile in a cylindrical channel conformation.

Hagen and Poiseuille independently produced an analytical solution for cylindrical shape channels to the equation above, which is called Hagen-Poiseuille (HP) flow [315]:

$$\Delta p = \frac{8 \eta L Q}{\pi R^4} \tag{5.4}$$

where Q is the volumetric flow rate and R is the radius of the cylindrical pore. HP analytical solution assumes that the liquid, flowing through the cylindrical channel, has zero velocity relative to the boundary (also known as no-slip condition; fig. 5.13). Here, v_r and v_{max} are the velocities at a radial distance r from the center and at the center of the flow channel, accordingly. They can be calculated with these formulations:

$$v_{max} = \frac{R^2 \Delta p}{4\eta L} \tag{5.5}$$

$$v(r) = v_{max}\left(1 - \frac{r^2}{R^2}\right) \tag{5.6}$$

In conical shape nanochannels, to calculate Q, an extended formulation of HP (i.e. for tapered nanopores) may be used instead [316]:

$$\Delta p = \frac{8\eta L Q}{\pi R^4}\left(\frac{3\lambda^3}{1 + \lambda + \lambda^2}\right) \tag{5.7}$$

here parameter λ represents the ratio between larger and smaller radii of a truncated channel.

An alternative solution to calculate volumetric flow in nanochannels was proposed by Dagan [317]. In this case Q can be calculated from Δp as follows:

$$\Delta p = \frac{Q\eta\left[3 + \left(\frac{8}{\pi}\right)\left(\frac{L}{R}\right)\right]}{R^3} \tag{5.8}$$

These theoretical models are going to be used to analytically evaluate flow through nanopores and compared to experimental data in the following paragraphs.

The flow setup, which was used for MQ water flow experiments through ~150 nm nanopores (membranes) is illustrated in fig. 5.14. Here, the flow is directed by nitrogen gas inlet through the custom made flow cell (with 2 inlets and 2 outlets, where 1 inlet and outlet is closed on each side) with a membrane sample inside, which is also in series with the flow module (S or M (details about these are given later on). On both sides of the flow cell, two pressure sensors are installed to measure Δp across the membrane, which will be used to calculate theoretical flow rates with models described above. In addition, an online degasser is used to get rid the system of possible air bubbles. Finally, when MQ water passes through the flow meter, it is collected into waste tubes, where the outlet is dipped inside MQ water to keep the pressure constant. Moreover, the flow rate and Δp data is collected in real-time during the whole experiment and used for latter modelling.

In fig. 5.15 flow experiments through ~150 nm nanopores (with 9 membranes) are shown. The inlet pressure (seen on the right hand side of a) and b) was gradually increased to a threshold of 500 mBar to facilitate flow through the pores and to avoid breaking the membrane due to overpressure. In a) almost a linear

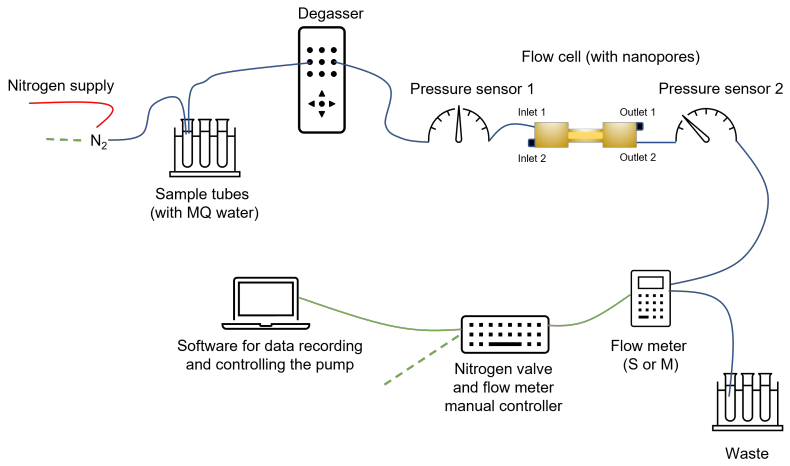

Figure 5.14: An illustration of the flow setup used for measuring MQ water flow through nanopores (membranes).

increase in flow rate is observed, however, significantly lower than the theoretically modelled values. When compared to, for example, with modelled flow rate according to Dagan formulation, experimentally achieved 0.06484 μL/min flow rate is 4377 times smaller (i.e. 284.50 μL/min calculated at Δp = -371.04 mBar; other modelled flow rates may be seen in table 5.1), and the cause for this is membrane clogging (i.e. contamination) with particulates. In addition, this is seen in an optical microscope image 5.15 d) taken after the flow experiment, where the whole membrane with the nanopores is covered with an unknown mesh (same with the other 8 membranes on the sample surface).

An attempt to regenerate the membrane was carried out as shown in fig. 5.15 c), where 10 - 200 mBar pressure pulses were applied every 10 seconds. Unfortunately, after the pump cycles were finished, the flow rate did not increase significantly, therefore it was assumed that the particles adhered irreversibly. Indeed, the nanopores should behave as great filters, but the contamination was expected to be insignificant when pre-filtered (0.2 μm) MQ water is used.

Table 5.1: Experimental and theoretical values for unfunctionalized and PNIPAM polymer brush coated ~150 nm nanopores (9 membranes as described in 3.2.2; S flow module).

Model	Flow rate, μL/min	
	Nanopores	PNIPAM Nanopores
Experimental	0.06484[a]	0.1532[b]
HP solution	478.68	444.53
HP for tapered pores (λ = 80/75)	421.30	391.24
Dagan	284.50	264.20

[a] at Δp = -371.04 mBar
[b] at Δp = -344.57 mBar

Nevertheless, the same membrane surface was coated with PNIPAM polymer brushes to possibly increase the antifouling properties of the surface (fig. 5.15 b). In this case, the flow rate increase is

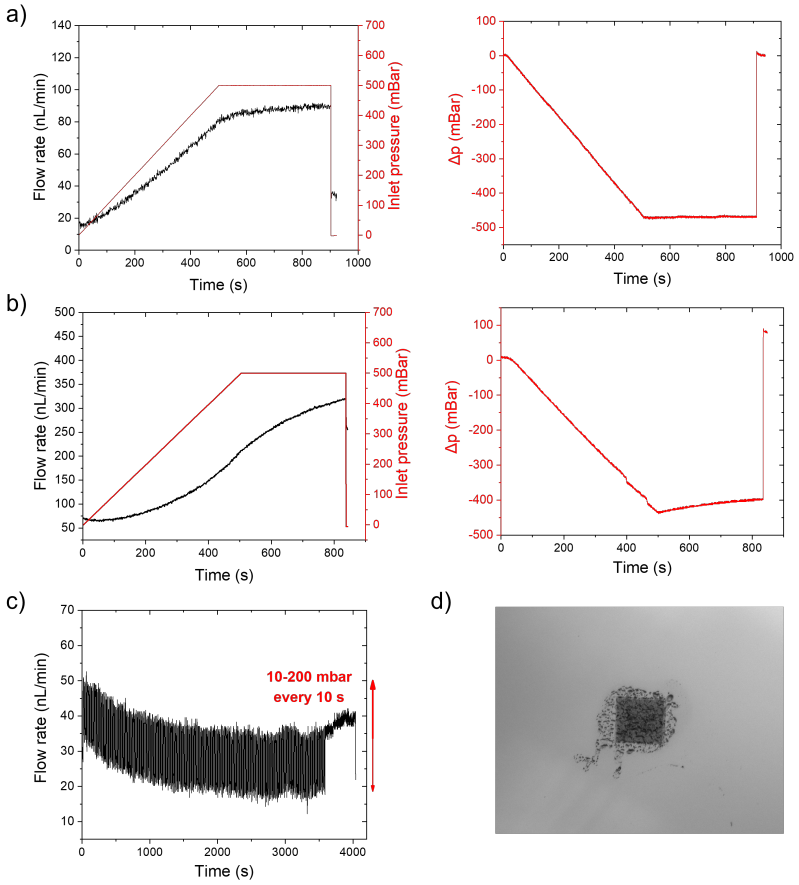

Figure 5.15: MQ water flow experiments through unfunctionalized and PNIPAM coated nanopores. a) Flow measurement with ~150 nm nanopore sample surface. b) Flow measured through PNIPAM functionalized (45v%MQ water, 30 min. polym. time) ~150 nm nanopores. To the right of a) and b), ΔP over the membrane surfaces are measured against time, respectively. c) Variation (pumping cycles) of inlet pressure between 10-200 mBar every 10 seconds for ~150 nm nanopore membrane; S flow module. d) An optical image of a clogged membrane after a flow experiment seen in a) (10x magnification).

not linear in respect to the rising inlet pressure, possibly indicating that the brush film is initially reducing the MQ water flow through the pore (i.e. the fluidic resistance is higher compared to a non-functionalized sample). Secondly, the experimentally obtained flow rate of 0.1532 μL/min is at least twice higher than when measured on non-functionalized nanopores, however still 1725 times smaller than the theoretical value (e.g. with Dagan model, 264.20 μL/min at Δp = -344.57 mBar). The reason why it is higher than for non-functionalized nanopores is probably because it decreases clogging over a long period of time.

The HP solutions for cylindrical and tapered pores result in ~2 times higher flow rates than for Dagans shown in table 5.1. Moreover, HP tapered formulation gives ~50 μL/min smaller flow rate for the same pores, which is also expected due to smaller pore diameter (by ~10 nm) on the other side of the membrane.

Because the experimental flow rates resulted in significantly smaller values compared to theoretical ones, it was assumed that it is due to membrane contamination.

Instead of module S (flow rate range = 0 - 7 μL/min for water with a measured value deviation of 5 % above 0.42 μL/min), flow module unit M was installed with the flow rate measuring range

of 0 - 80 µL/min (for water; measured value deviation is 5 % above 2.4 µL/min) and the results are presented further on.

In fig. 5.16 a) it can be seen that the flow rate saturates at 2.10 µL/min (at 677 seconds) at Δp = -181.38 mBar and gradual decrease in flow rate over the next 800 seconds follows. While changing the flow unit gave a ~20 times increase in flow rate (i.e. 1.33 µL/min; see table 5.2) compared to the case in fig. 5.15 a) (0.06484 µL/min), the variation is still attributed due to different levels of clogging inside the membrane, which dominates Δp and consequently the flow. Also, when the flow rate is modelled with, e.g. Dagan formulation in this case, the difference between the theoretical and experimental values is still huge (i.e. 83.41 µL/min at Δp = -109.4 mBar for Dagan model). This led to a conclusion that the deviation must come mainly from the contamination on the membranes, therefore a more thorough cleaning protocol was introduced, where the membranes were washed twice with RCA-1 protocol instead.

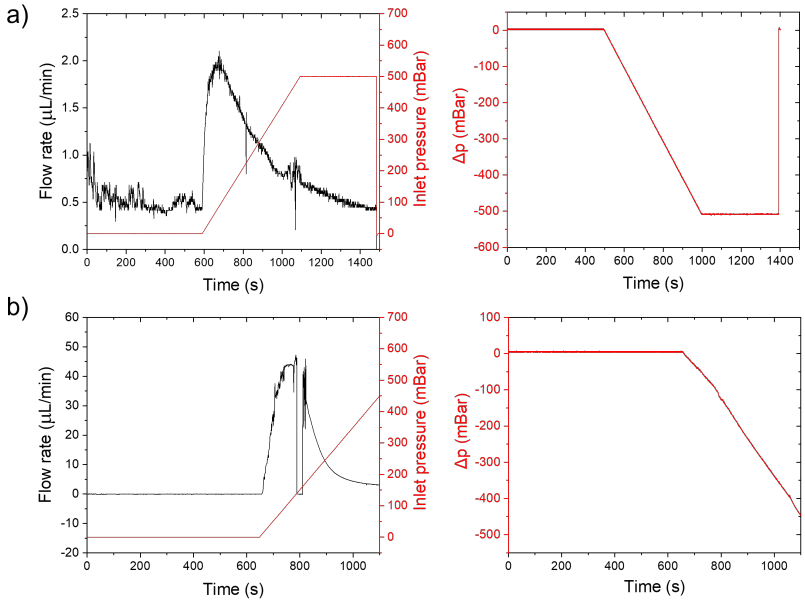

Figure 5.16: Flow experiments through nanopores. a) Flow measurement with M flow meter module and 150 nm nanopore sample surface (with 9 membranes). b) Flow measurement through twice RCA-1 washed 150 nm nanopore membrane (module M). To the right of a) and b) Δp over the membrane surfaces against time for the experiments are shown, accordingly.

In the case of 5.16 b), where the same nanopore sample surface was used as in a) and washed twice with RCA-1 solution, it can be seen that when inlet pressure is gradually increased to 500 mBar, the flow rate saturates at 44.12 µL/min (at 764 seconds) at Δp = -84.88 mBar inlet pressure. This is almost a 23 time fold increase compared to when the nanopore membranes was washed only once with RCA-1 solution.

When compared to theoretical flow rate (e.g. from Dagan; see table 5.2) of 24.69 µL/min calculated at Δp = -32.2 mBar, the experimental flow rate, being 27.08 µL/min, is higher by less than 10 %. In addition, HP solution for flow through tapered pores is

closer (36.56 μL/min) to the experimental flow rate value than the HP solution for a cylindrically shaped pore (41.54 μL/min), possibly being a better fit for the system. However, the solution for tapered pores theoretical value still deviates from the experimental value by ~26%.

Model	Flow rate, μL/min	
	Nanopores (1x RCA-1)	Nanopores (2x RCA-1)
Experimental	1.33[a]	27.08[b]
HP solution	139.39	41.54
HP for tapered pores (λ = 80/75)	122.68	36.56
Dagan	83.41	24.69

Table 5.2: Experimental and theoretical values for unfunctionalized ~150 nm nanopores (9 membranes; M flow module) washed once or twice with RCA-1.

[a] at Δp = -109.4 mBar
[b] at Δp = -32.2 mBar

Further investigations of flow rates through PNIPAM polymer brush coated nanopores (membranes) with module M was not carried out due to time restrictions. Nevertheless, apart from having a more thorough cleaning procedure for the membranes, we believe that the deviation of experimental and theoretical flow rate values may further be improved by installing a pre-column filter (such as used in HPLC systems), which would block the particulates accumulating and diminishing the water flow through the nanopores.

5.4 Protein transport gating in nanopores (membranes) induced by shear flow

An attempt to facilitate BSA protein transport by shear flow through 20 kDa PEG grafted 80 nm diameter nanopores (membranes) can be seen in fig. 5.17. Before the plasmonic shift increase in Peak and Dip at ~3000 seconds, the flow cell was pre-filled with BSA solution (PBS buffer, pH = 5.5; at 620 seconds) on the polymer-gold side and only with PBS buffer pH = 5.5 on the SiN_x side. Because no expected signal from BSA adsorption was seen upon loading the coated gold side of the membrane, it was assumed that 20 kDa PEG is a sufficient barrier (is densely grafted and has the right thickness compared to pore diameter) to block protein from entering the interior of the channel as showed previously with nanowell samples by Emilsson *et al*. [58]. However, when the last outlet on the flow cell was closed (same custom made flow cell as seen in flow setup illustration (fig. 5.14), BSA leaked through as Peak and Dip plasmonic shift increased by 0.604 nm and 0.580 nm, respectively.

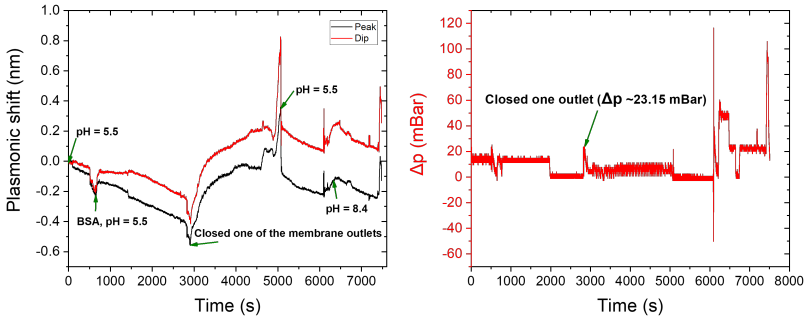

Figure 5.17: Real-time plasmonic shift monitoring of BSA protein transport gating in 20 kDa PEG coated (gold side) nanopores (~80 nm in diameter). The protein is pushed through the PEG polymer brush covered nanopores by an increase of pressure on the gold side. The image on the right shows pressure difference across the membrane during the experiment.

Because during the whole experiment Δp was being recorded (seen on the right hand side of fig. 5.17), it is possible to extrapolate which Δp is required to push BSA protein through the PEG covered pore. At ~3000 seconds, a pressure difference of -23.15 mBar has been found, which caused protein translocation event to occur.

Even though the experiment was not repeated due to time restrictions, we can conclude that controlling protein translocation through otherwise polymer blocked membranes should be possible with shear flow.

Conclusions 6

In **paper I** we have shown that two noble metals, platinum and palladium, can be used in SPR experiments to monitor chemical modifications. The main principles underlying this is measuring full angular spectra and performing accurate quantitative analysis. When a spectrum is acquired in air, Fresnel models are fitted in the angular range between TIR and SPR angles (i.e. where the highest intensity changes occur). Moreover, it was shown that real-time SPR experiments in aqueous solutions can be conducted if the angle range to track the SPR angle is wide enough. When compared to gold sensors, SPR sensograms obtained on platinum and palladium surfaces indicate higher noise levels (especially on platinum), but organic layer binding events (e.g. thiolated PEG adsorption) can still be readily observed. Near field distributions and SPR angle shifts for platinum and palladium show similarity to gold even though the film thicknesses differ by more than a factor of two (20 nm for platinum and palladium, and 50 nm for gold). Grafted PEG films on platinum and palladium proved to be antifouling for BSA proteins as shown in the real-time data. During these experiments in liquid, it was noticed that platinum is less sensitive to bulk refractive index changes, but has a higher field extension than palladium.

In **paper II** we explained how an analytical solution can be used to solve the "bulk contribution" issue in SPR without utilizing a separate reference channel as shown previously [224]. The bulk effect has to be removed in order to correctly analyze low affinity interactions and highly concentrated systems, where it dominates the signal. Moreover, it was shown that the instrument available bulk correction tool leads to incorrect interpretation of data as it does not incorporate film dimensions.

Even if our proposed method may not be applicable for dense organic layers, full Fresnel models can be used in this case. We admit that our technique produces some extra noise in the corrected sensograms, because the TIR angle is noisier than the SPR angle, but it does not limit its application.

An interaction between PEG polymer brushes and lysozyme was investigated at physiological conditions and an equilibrium affinity constant of ~200 μM was determined (**paper II**). In addition, it was shown by SPR measurements, that lysozyme proteins interact reversibly with themselves (i.e. with an irreversibly bound layer of lysozyme proteins on gold). Therefore, we emphasize that SPR can

be used to study protein self-interactions at high concentrations (e.g. >10 g/L) also.

In the review **paper III** we have discussed artificially constructed systems, which are inspired by molecule transport mechanisms and constituents of the nuclear pore complexes (NPCs; found in eukaryotic cells). Most of these, including ours (proposed in **paper IV**), have solid state nanopores chemically functionalized with synthetic polymers or peptides. In some other cases, DNA origami materials are employed to mimic the nuclear pore complex, but biomolecule transport through these remains to be studied. Moreover, we highlight gel systems, which show prominent selectivity when it comes to protein transport, however, due to their macroscopic sizes they do not represent the NPC very well. Also, we contemplate that it would be challenging to produce nanosized gels in contact with multiple separated compartments and observe how biomolecule transport is influenced as a result.

Even though, the shuttle-cargo transport mechanism was shown in a few instances [318, 319], due to lack of selectivity, they are still far performance-wise from the biological assemblies. One of the reasons why it is so burdensome to mimic NPCs with artificial systems is the need of flexibility in construct morphology. A lot of the platforms are usually not switchable and do not prevent protein transportation completely. Second of all, if shuttle molecules with cargo bind to the receptors with too high affinity, the nanopores can clog, rendering the system unusable anymore. Lastly, we mention several contradicting studies regarding the intrinsic disorder (i.e. compared to solid state materials) role in necessary barrier properties (e.g. the density of the barrier) [58, 320, 321], which show our current limited understanding. All in all, we think that creating artificial pores prove advantageous as they give us tips about how the biological systems function even if they are not fully functional yet and can make space for improvements in biomolecule separation technologies.

In **paper IV** we show controlled gating of BSA protein transport and trapping, established with PNIPAM polymer brush functionalized nanowells. Real-time plasmonic shift monitoring and fluorescence experiments on full coverage and individual nanowell arrays yielded complementary results, where BSA was adsorbed at slightly below physiological pH in the interior of the nanowells (i.e. silica surface) and desorbed at high pH. The transport of the biomolecules is prevented below PNIPAM LCST (where the polymers are in the extended state) and allowed when the surface is heated to above PNIPAM LCST. However, we observed that a fraction of polymer coated NWs might not have thick enough polymer brushes in their vicinity, thus some proteins enter when the polymers are in the hydrated state. It was concluded that this

is due to deviation in polymer brush uniformity and/or some contaminants left after nanostructure fabrication (which lead to irreversible protein adsorption). However, we emphasize that the majority of the nanocompartments have the right polymer film thickness, leaving the gating mechanism fully controllable. Furthermore, BSA pH-reversible adsorption was investigated with QCM-D experiments on planar silica and with real-time plasmonic shift monitoring on short PEG chain functionalized nanowells. With SPR time trace data we have illustrated that, in contrast to some previous reports, BSA does not adsorb above PNIPAM LCST on PNIPAM polymer brush coated planar gold. This could be explained by the high grafting density of PNIPAM polymer brushes, which excludes proteins from penetrating the film. Finally, we have presented that small molecules, such as fluorescent dyes, solvent and ions can still pass through the densely packed PNIPAM brush in the hydrated state in contrast to larger proteins, which indicates a certain size cutoff for the permeability of the polymer layer.

In chapter **5** I have presented a series of unpublished results, which include pH-irreversible and pH-reversible BSA adsorption with batches from different suppliers and flow experiments through nanochannels. An investigation of optimal protein adsorption pH was carried out with QCM-D measurements, which allowed selecting a range between pH = 5.5 - 6.0 (slightly above BSA isoelectric point). In terms of flow measurements with non-functionalized and PNIPAM coated nanopores, I have compared the theoretically estimated (e.g. Dagan, HP and HP-tapered models) and experimentally determined flow rates. For most of the cases, the experimentally achieved flow rates are significantly lower than the theoretically predicted. The reason for this is most likely membrane clogging (i.e. nanopores act as excellent filters) and/or air trapped inside the pores. Nevertheless, it was shown in one instance that it is possible to experimentally attain a flow rate, which is comparable to a rate calculated with e.g. Dagan model. Furthermore, when HP solution is compared to Dagan model, the flow rates differ almost by a factor of 2 (HP solution for tapered pores is similar). In the end, I have presented that it is possible to push BSA proteins through the 20 kDa PEG polymer brush coated nanochannel with shear flow, which increases the amount of techniques in the gating mechanism toolbox for biomolecule trapping systems.

Outlook 7

We have have created a polymer brush functionalized nanochamber system to trap many proteins in a reliable manner, therefore the next step is to enable this system to trap, gate and detect single molecules. This would have a huge impact on molecular biology and biotechnology as millions of proteins exist. For example, with this generic platform, scientists around the world could study subpopulations and rare states (e.g. intermediate states) of proteins in ensembles, reaction mechanisms and determine kinetic parameters (e.g. association/dissociation rates) of protein interactions by tracking equilibrium fluctuations in physiological conditions.

Our vision is that single molecules can be detected in the proposed traps by coupling our systems (i.e. membranes) with a patch-clamp amplifier and complementary electronic components to measure changes in ionic current. For example, two electrodes would be located on each side of the membrane and the drops in current would be monitored, relating them to single molecule translocations in time (pore's conductivity is smaller when e.g. a protein blocks a fraction of its volume) [322, 323]. The biomolecules could be pushed through the pore by electrokinetic forces, which are influenced by the applied voltage (i.e. creates the ionic current) and/or directed by varying the solution pH to manipulate protein's net charge as mentioned in section 4.4. In addition, we envision that the membrane could be chemically modified with different polymers (stimuli-responsive or not) on opposite ends of the channel.

The strategy would remain the same as described before in chapter 1 - to have a platform to trap proteins, where they would move freely inside the pore (i.e. to mimic their native environment). However, instead of a cylinder shape nanopore (discussed in the unpublished results section 5.3), one can think of a conically formed channel, where one end is much smaller than the other. Then, the smaller diameter opening could be closed for proteins (i.e. they would not spontaneously leak into the pore), for example, with sufficiently thick and protein-repelling PEG polymer brush. In this case, hydrodynamic forces (due to pressure difference across the nanopore) would be employed to push the proteins into the interior of the channel (same as shown in section 5.4). The other side of the pore (i.e. larger diameter entrance) may be coated with a stimuli-responsive polymer, such as PNIPAM instead, to establish an alternative gating mechanism for biomolecules in the system.

To further ensure that proteins are trapped inside the nanochannels, state-of-the-art single-molecule fluorescence microscopy techniques together with high signal-to-noise ratio CCD camera (for wide-field microscopy experiments) would be used. For example, confocal microscopy can be employed to reduce the background light coming from other focal planes and focus only on the plane of the nanochamber. In this case, it would be possible to track spontaneous translocation events (or lack of) [324] as well, because the biomolecules would be confined to a tiny chamber. For example, when the voltage is applied on the nanopore and a translocation event is detected due to a momentarily reduced current, the fluorescence readout would be carried out. The trapped proteins can be released by collapsing PNIPAM polymer brushes on one side, consequently diminishing the fluorescence signal. In this way, the platform can be re-used for many protein transport gating experiments rather straightforwardly.

Due to the fact that multiple chambers exist on these kind of nanopore arrays, one can envision many biomolecule gating experiments being done at the same time [15]. However, the challenge here is how to focus the electrical reading on the translocation event on an individual nanopore. One possible solution could be to use optical imaging alone, as proposed above, but it would not be ideal for single molecule experiments in practice as bleaching might take place before the proteins are even trapped in the interior of the nanopore. On the other hand, there is already development in parallel readout methods for ion currents in nanopore arrays being conducted nowadays [325], which could deem very useful. By employing these, fast confocal imaging can be used together for high throughput screening of trapped proteins.

It could be possible to trap different biomolecules (not necesserily limited to proteins only) in the interior of the nanochannels with our proposed platform. By labelling proteins with different fluorophores it should be possible to identify at least 3-5 per chamber while still avoiding the spectral overlap. However, one should keep in mind that various proteins are affected by electrokinetic forces differently, depending on their size and charge. Nevertheless, it should not be a significant issue as this can be compensated by knowing a reference current from experiments with each protein to be used individually beforehand.

Finally, FRET could be a great candidate technique to be coupled with polymer functionalized nanochambers as it can be used to monitor protein conformational changes (if one protein is labelled with two fluorophores, for example), ligand-receptor interactions and their rates.

Acknowledgements

With great respect I acknowledge the project sponsors - The Erling-Persson Family Foundation and the European Research Council, who have funded this project.

Special acknowledgement is given to my main supervisor Andreas Dahlin, who has guided me well through the projects in the PhD studies and my co-supervisor Anette Larsson.

I would also like to thank all of my colleagues at Applied Surface Chemistry division, special thank you to my girlfriend Gabriele Valanciute and Felix Hemmingsson, previous and current group members - John Andersson, Zeynep Adali, Oliver Olsson, Gustav Ferrand-Drake Del Castillo, Rebekah Hailes, Jolie Blake, Gustav Emilsson, Asaad Umair, Bita Malekian, Sophia Thiele, Marika Gugole, Kunli Xiong, Tim Robson and others, who have helped me either to edit this thesis, had scientific discussions together or introduced me to the instruments. Also, my family and friends for the moral support.

Justas Svirelis, Göteborg, November 2022

Appendix

Appendix A

Table A.1: Chemicals and materials used for this thesis

Material	Description
Sigma Aldrich	
2-propanol	≥ 99%
Acetone	≥ 99%
Bovine serum albumin	≥ 98% (Lot SLBX0893)
Borate buffer saline	tablets; pH 8.2
Copper (II) Bromide	99%
Bis[2-(2-bromoisobutyryloxy)- -undecyl] disulfide	97%; Stored degassed
Hydrogen chloride	37%
Lysozyme from chicken egg white	≥ 90%
L-Ascorbic acid	99%
Methanol	99.8% anhydrous
N-isopropylacrylamide	≥ 99%; Stored degassed
N, N, N′, N″, N″- -Pentamethyldiethylenetriamine	99%
Phosphate buffer saline	tablets; pH 7.2
Polyethylene glycol	35 kDa
Sulfuric acid	95.0% - 97.0%
Sodium dodecylbenzene sulfonate	≥ 99%
Sodium hydroxide	≥ 97%
Thermo Fisher Scientific	
Ammonium hydroxide solution	28-30%
Bovine serum albumin	≥ 96%
Bovine serum albumin, alexa Fluor 488 Conjugate	7 moles of dye per mole of protein
NML Syringe Filter	Nonsterile, hydrophilic, 0.2 μm
Solveco	
Ethanol	95% anad 99.5%
Circuitworks	
Conductive epoxy glue	Used for gluing insulated copper wires to samples
Merck	
Molecular sieves	0.3 nm
H_2O_2	30%
Prochimia	

Continued on the next page

Table A.1: Chemicals and materials used for this project (cont.).

Material	Description
HS-C11- OC(O)- IzoButyrate-Br	Stored degassed and frozen
RS components	
Polyether ether ketone	Used as the main block material for the flow cell
VWR	
Fused silica	Utilized as a material for flow cell windows
Picodent Twinsil	
Addition-curing duplicating silicone	Used for gluing flow cell windows
Dow Corning	
High vacuum grease	Used when vacuum drying the molecular sieves
Laysan Bio	
Thiolated polyethylene glycol	2 kDa
Lumiprobe	
Sulfo-cyanine 3 NHS ester	A fluorescent dye, which targets primary amines
In-house	
Milli-Q water	ASTM Research grade Type I ultrafiltered water from a Millipore system (18.6 MΩs)
Provided	
3-aminopropylsilatrane	Kindly provided by Chun-Jen from the Department of Biomedical Sciences and Engineering, National Central University, Jhongli City, Taiwan

Appendix B

The first blueprint of the designed flow cell for optical microscopy in-situ experiments:

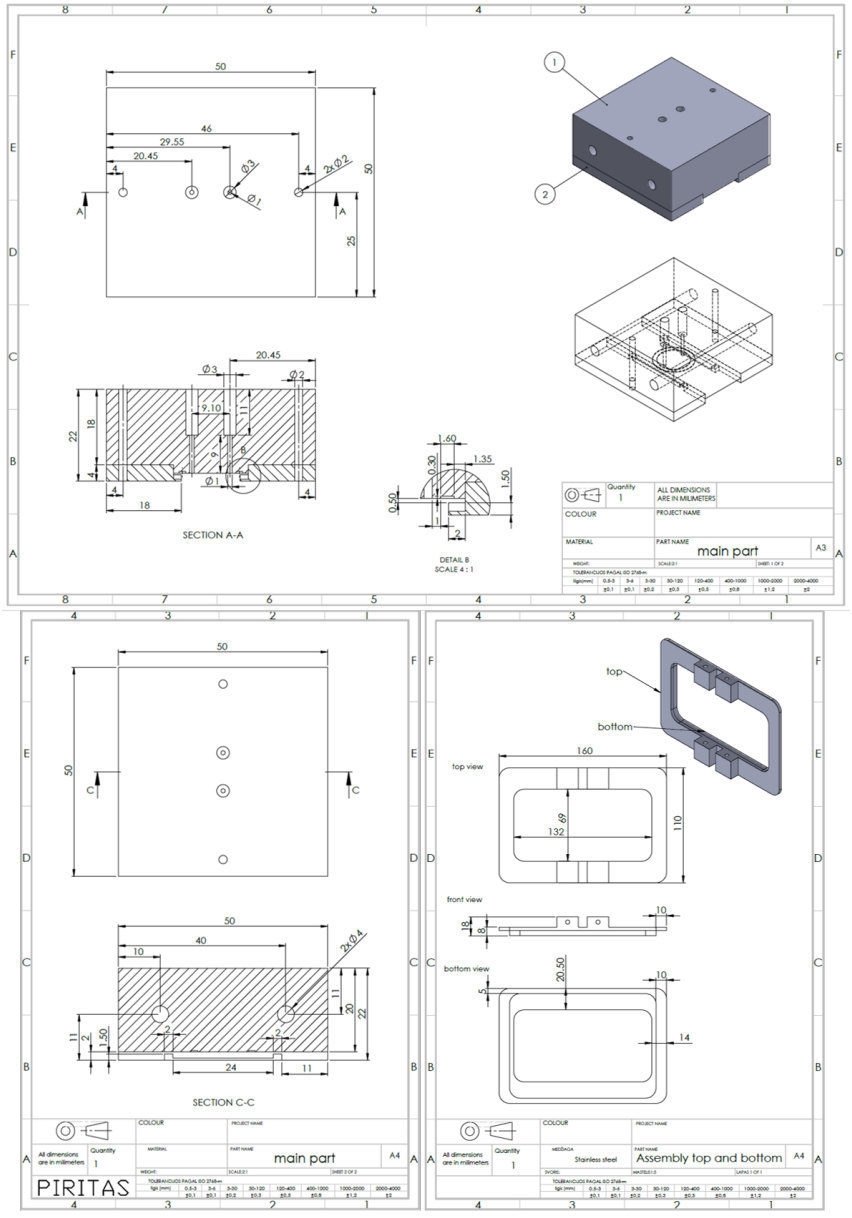

Figure B.1: First model of the flow cell designed for fluorescence microscopy and plasmonic shift experiments.

The first flow cell had to be re-designed because gave too high background noise from the light, which was reflected from the top wall of the flow cell perpendicular to the incident beam. Therefore, a second (up to date) blueprint of the flow cell for optical microscopy in-situ experiments was designed:

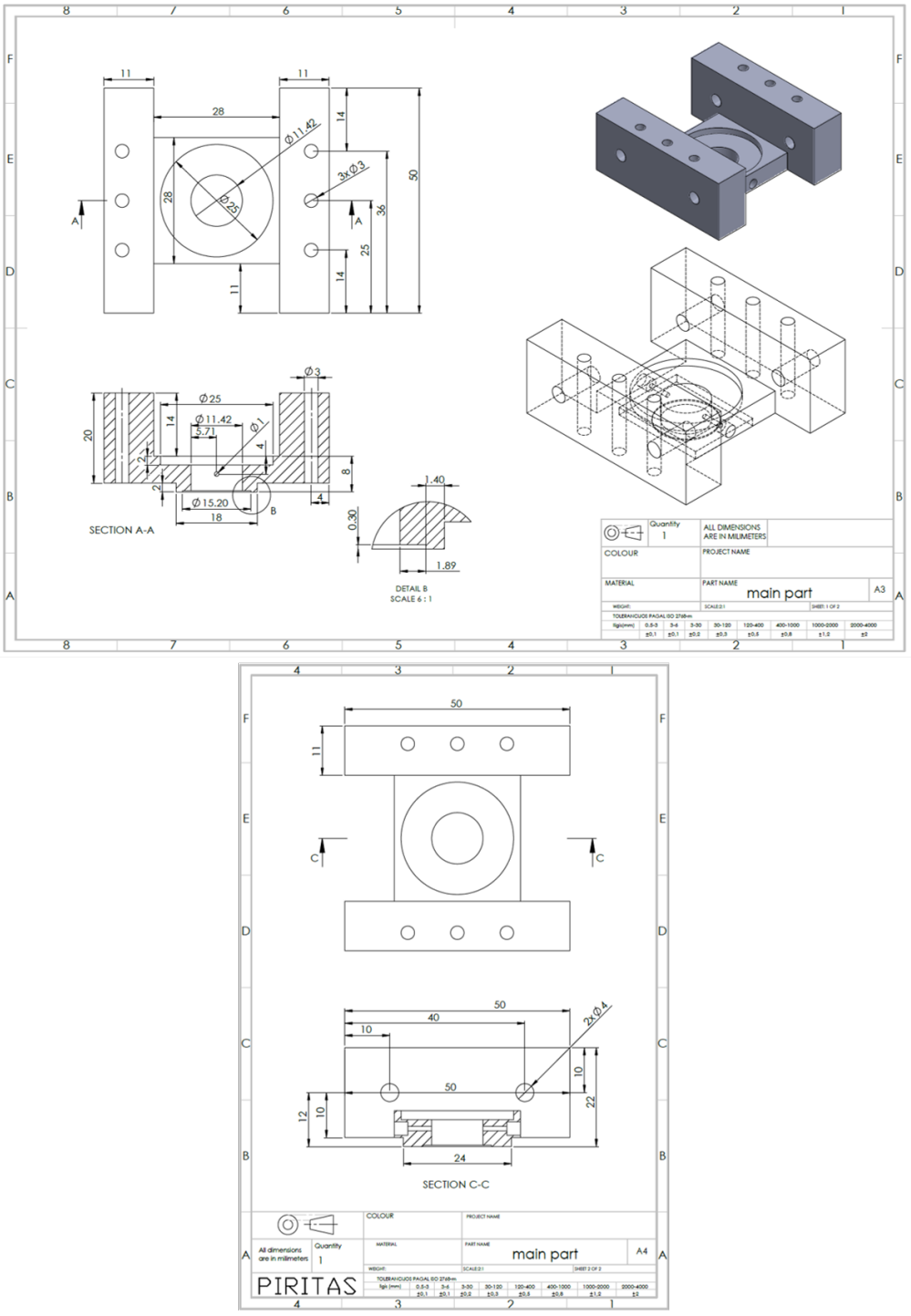

Figure B.2: Up-to date model of the flow cell designed for fluorescence microscopy and plasmonic shift experiments.

Appendix C

All determined plasmonic "peak" and "dip" shift numerical values upon heating DTBU (disulfide) and TBU (thiol) initiated sample surfaces above PNIPAM LCST can be seen in figure C.1.

TBU

MQ water, v%	Polym. time, min	Peak shift, nm	Dip shift, nm
70.3	5	0.609	-0.178
70.3	10	1.293	1.117
70.3	10	0.876	-0.222
70.3	25	-0.275	6.359
70.3	25	0.063	6.843
70.3	25	-0.302	6.35
70.3	25	-0.046	6.6
45	15	-0.254	-0.645
45	15	0.334	0.083
45	15	-0.083	-0.47
45	20	0.102	-0.711
45	20	0.104	-0.305
45	20	1.248	1.286
45	25	3.185	3.432
45	30	0.936	0.535
45	30	3.315	3.937
45	30	3.23	3.413
45	30	1.87	2.83
45	30	3.063	3.045
45	30	3.244	3.628
45	35	4.415	5.31
45	35	4.41	5.66
45	40	3.01	3.48
45	40	3.008	3.453
45	50	1.496	1.37
45	60	4.57	5.85
45	180	4.16	5.27
45	240	4.69	5.16
40	25	1.329	0.973
40	25	1.252	1.1
40	30	1.602	1.54
40	30	0.857	0.656
40	30	0.577	0.531
40	30	0.686	0.433
40	300	0.824	3.17
39	17	0.701	-
39	18	2.039	2.047
39	19	1.03	1.489
39	20	1.11	-
39	21	0.747	0.613
39	24	1.422	1.77
39	25	1.897	2.474
39	25	3.026	1.6102
39	25	3.688	0.4982
39	30	1.03	1.24
39	30	1	1.12
39	60	4.926	2.647
39	120	3.82	1.389
37	25	1.23	1.074
37	25	1.873	1.391

Polym. time, min	MQ water, v%	Peak shift, nm	Dip shift, nm
25	70.3	-0.275	6.359
25	70.3	0.063	6.843
25	70.3	-0.302	6.35
25	70.3	-0.046	6.6
25	45	3.185	3.432
25	43	3.59	3.73
25	40	1.329	0.973
25	40	1.252	1.1
25	37	1.873	1.391
25	37	1.23	1.074
30	35	2.675	2.56
30	39	1	1.12
30	39	1.03	1.24
30	40	1.602	1.54
30	40	0.857	0.656
30	40	0.577	0.531
30	40	0.686	0.433
30	42	3.401	3.45

DTBU

MQ water, v%	Polym. time, min	Peak shift, nm	Dip shift, nm
50	10	2.27	4.06
50	10	4.2	6.39
50	15	4.73	7.7
50	15	4.29	6.41
45	80	1.97	2.716
45	100	2.907	3.99
45	100	1.427	1.148
45	100	1.545	2.17
45	100	1.429	2.032
45	100	1.207	0.935
45	110	0.94	1.41
45	120	1.217	2.23
45	120	2.79	4.43
45	135	1.579	2.12
45	150	1.586	2.101
45	180	0.813	1.16
45	180	2.205	3.66
45	180	2.652	3.275
45	300	2.42	4.34
40	1440	0.57	1.168
40	1440	1.35	2.078
40	300	0.582	1.79
40	300	0.825	3.01

Polym. time, min	MQ water, v%	Peak shift, nm	Dip shift, nm
1440	10	0.26	0.39
1440	20	0.28	0.29
1440	30	0.437	0.734
1440	30	0.448	0.74
1440	35	0.809	1.239
1440	35	0.52	1.13
1440	35	0.664	0.67
1440	35	0.642	1.9
1440	40	0.57	1.168
1440	40	1.35	2.078
300	40	0.582	1.79
300	40	0.825	3.01
300	42	0.754	1.984
300	45	2.42	4.34
10	50	2.27	4.06
10	50	4.2	6.39
10	20	-0.03	-0.13
10	10	-0.08	-0.3

Figure C.1: All measured Peak and Dip plasmonic shifts with TBU (left collumns) and DTBU (right columns) initiated PNIPAM polymer brush surfaces.

Bibliography

[1] J. Andersson, J. Svirelis, G. F.-D. Del Castillo, T. Sannomiya and A. Dahlin. 'Surface plasmon resonance sensing with thin films of palladium and platinum–quantitative and real-time analysis'. In: *Physical Chemistry Chemical Physics* 24.7 (2022), pp. 4588–4594.

[2] J. Svirelis, J. Andersson, A. Stradner and A. Dahlin. 'Accurate Correction of the "Bulk Response" in Surface Plasmon Resonance Sensing Provides New Insights on Interactions Involving Lysozyme and Poly (ethylene glycol)'. In: *ACS sensors* 7.4 (2022), pp. 1175–1182.

[3] J. Andersson, J. Svirelis, J. Medin, J. Järlebark, R. Hailes and A. Dahlin. 'Pore performance: artificial nanoscale constructs that mimic the biomolecular transport of the nuclear pore complex'. In: *Nanoscale Advances* (2022).

[4] J. Svirelis, Z. Adali, G. Emilsson, R. Vattikunta, J. Andersson, K. Kolman, O. Olsson, Y. Sakiyama, R. Y. H. Lim and A. Dahlin. 'Stable Trapping of Multiple Proteins at Physiological Conditions Using Nanoscale Chambers with Macromolecular Gates'. Preprint available. To be submitted to Nature Communications, 2022.

[5] K. Xiong, O. Olsson, J. Svirelis, C. Palasingh, J. Baumberg and A. Dahlin. 'Video Speed Switching of Plasmonic Structural Colors with High Contrast and Superior Lifetime'. In: *Advanced Materials* 33.41 (2021), p. 2103217. DOI: https://doi.org/10.1002/adma.202103217.

[6] F. Banoa, L. Soria Martinez, K. Seier, D. Conca, E. Heidenfels, J. Svirelis, K. Throssteinsson, A. Dahlin, M. Schelhaas and M. Bally. 'Role of sulphation pattern in modulating the interactions between human papillomavirus and cell surface glycosaminoglycans at the single particle level'. In manuscript, 2022.

[7] J. C. Kendrew, G. Bodo, H. M. Dintzis, R. G. Parrish, H. Wyckoff and D. C. Phillips. 'A three-dimensional model of the myoglobin molecule obtained by x-ray analysis'. In: *Nature* 181.4610 (1958), pp. 662–666.

[8] A. Küchler, M. Yoshimoto, S. Luginbühl, F. Mavelli and W. Peter. 'Enzymatic reactions in confined environments'. In: *Nature Nanotechnology* 11 (May 2016), pp. 409–420.

[9] O. Acuner, E. Saliha, Engin Hatice B., A. Gursoy and O. Keskin. 'Transient protein–protein interactions'. In: *Protein Engineering, Design and Selection* 24.9 (June 2011), pp. 635–648.

[10] N. Cremades, S.I.A. Cohen, E. Deas, A. Abramov, A. Chen, A. Orte, M. Sandal, R. Clarke, P. Dunne, F. Aprile, C. Bertoncini, N. Wood, T. Knowles, C. Dobson and D. Klenerman. 'Direct Observation of the Interconversion of Normal and Toxic Forms of α -Synuclein'. In: *Cell* 149 (May 2012), pp. 1048–59.

[11] P. Chene. 'The role of tetramerization in p53 function'. In: *Oncogene* 20 (June 2001), pp. 2611–7.

[12] I. M. Kuznetsova, K. K. Turoverov and V. N. Uversky. 'What macromolecular crowding can do to a protein'. In: *International journal of molecular sciences* 15.12 (2014), pp. 23090–23140.

[13] P. Radivojac, L. M. Iakoucheva, C. J. Oldfield, Z. Obradovic, V. N. Uversky and A. K. Dunker. 'Intrinsic disorder and functional proteomics'. In: *Biophysical journal* 92.5 (2007), pp. 1439–1456.

[14] A. K. Dunker, C. J. Brown, J. D. Lawson, L. M. Iakoucheva and Z. Obradović. 'Intrinsic disorder and protein function'. In: *Biochemistry* 41.21 (2002), pp. 6573–6582.

[15] M. Brucale, B. Schuler and B. Samorì. 'Single-Molecule Studies of Intrinsically Disordered Proteins'. In: *Chemical Reviews* 114.6 (2014), pp. 3281–3317.

[16] Q. Chen, R. Groote, H.r Schönherr and G. J. Vancso. 'Probing single enzyme kinetics in real-time'. In: *Chem. Soc. Rev.* 38 (9 2009), pp. 2671–2683.

[17] N. G. Walter, Cheng-Yen Huang, J. A. Manzo and A. M. Sobhy. 'Do-it-yourself guide: how to use the modern single-molecule toolkit'. In: *Nature Methods* 5 (May 2008), pp. 475–489.

[18] K.C. Holmes. 'Flexibility in tobacco mosaic virus'. In: *Mobility and Function in Proteins and Nucleic Acids* 116 (1983).

[19] S. W. Muchmore, M. Sattler, H. Liang, R. P. Meadows, J. E. Harlan, H. S. Yoon, D. Nettesheim, B. S. Chang, C. B. Thompson, S.-L. Wong et al. 'X-ray and NMR structure of human Bcl-x L, an inhibitor of programmed cell death'. In: *Nature* 381.6580 (1996), pp. 335–341.

[20] V. Receveur-Bréchot and D. Durand. 'How random are intrinsically disordered proteins? A small angle scattering perspective'. In: *Current Protein and Peptide Science* 13.1 (2012), pp. 55–75.

[21] M. Varadi, S. Kosol, P. Lebrun, E. Valentini, M. Blackledge, A. K. Dunker, I. C. Felli, J. D. F.-K., R. W. Kriwacki, R. Pierattelli et al. 'pE-DB: a database of structural ensembles of intrinsically disordered and of unfolded proteins'. In: *Nucleic acids research* 42.D1 (2014), pp. D326–D335.

[22] H. Miller, Z. Zhou, J. Shepherd, A. J. M. Wollman and M. C. Leake. 'Single-molecule techniques in biophysics: a review of the progress in methods and applications'. In: *Reports on Progress in Physics* 81.2 (2017), p. 024601.

[23] *PubMed publication count on intrinsically disordered proteins*. Accessed: 2022-01-20. URL: http://www.ncbi.nlm.nih.gov/pubmed.

[24] Z. Obradovic, K. Peng, S. Vucetic, P. Radivojac, C. J. Brown and A. K. Dunker. 'Predicting intrinsic disorder from amino acid sequence'. In: *Proteins: Structure, Function, and Bioinformatics* 53.S6 (2003), pp. 566–572.

[25] J. W. Weisel and R. I. Litvinov. *Fibrin formation, structure and properties*. Vol. 82. January. 2017, pp. 405–456.

[26] L. Duan, Q. Zheng, H. Zhang, Y. Niu, Y. Lou and H. Wang. 'The SARS-CoV-2 Spike Glycoprotein Biosynthesis, Structure, Function, and Antigenicity: Implications for the Design of Spike-Based Vaccine Immunogens'. In: *Frontiers in Immunology* 11.October (2020), pp. 1–12.

[27] P. E. Wright and H. J. Dyson. 'Intrinsically disordered proteins in cellular signalling and regulation'. In: *Nature Reviews Molecular Cell Biology* 16.1 (2015), pp. 18–29.

[28] G. W. Daughdrill, M. S. Chadsey, J. E. Karlinsey, K. T. Hughes and F. W. Dahlquist. 'The C-terminal half of the anti-sigma factor, FlgM, becomes structured when bound to its target, σ 28'. In: *Nature structural biology* 4.4 (1997), pp. 285–291.

[29] C. A. Galea, A. Nourse, Y. Wang, S. G. Sivakolundu, W. T. Heller and R. W. Kriwacki. 'Role of intrinsic flexibility in signal transduction mediated by the cell cycle regulator, p27Kip1'. In: *Journal of molecular biology* 376.3 (2008), pp. 827–838.

[30] A. K. Dunker and V. N. Uversky. 'Signal transduction via unstructured protein conduits'. In: *Nature chemical biology* 4.4 (2008), pp. 229–230.

[31] A. V. Follis, C. A. Galea and R. W. Kriwacki. 'Intrinsic protein flexibility in regulation of cell proliferation: advantages for signaling and opportunities for novel therapeutics'. In: *Fuzziness* (2012), pp. 27–49.

[32] C. J. Oldfield and A. K. Dunker. 'Intrinsically disordered proteins and intrinsically disordered protein regions'. In: *Annual Review of Biochemistry* 83 (2014), pp. 553–584.

[33] V. N. Uversky. 'Intrinsically disordered proteins and their "Mysterious" (meta)physics'. In: *Frontiers in Physics* 7.FEB (2019), pp. 8–23.

[34] P. Kulkarni, T. Shiraishi and R. V. Kulkarni. 'Cancer : tilting at windmills ?' In: *Mol Cancer* 12 (2013), p. 108.

[35] R. F. Doolittle and J. M. Kollman. 'Natively unfolded regions of the vertebrate fibrinogen molecule'. In: *PROTEINS: Structure, Function, and Bioinformatics* 63.2 (2006), pp. 391–397.

[36] G. Tsurupa, A. Mahid, Y. Veklich, J. W. Weisel and L. Medved. 'Structure, stability, and interaction of fibrin αC-domain polymers'. In: *Biochemistry* 50.37 (2011), pp. 8028–8037.

[37] R. W. Kriwacki, L. Hengst, L. Tennant, S. I. Reed and P. E. Wright. 'Structural studies of p21Waf1/Cip1/Sdi1 in the free and Cdk2-bound state: conformational disorder mediates binding diversity'. In: *Proceedings of the National Academy of Sciences* 93.21 (1996), pp. 11504–11509.

[38] W.-L. Hsu, C. J. Oldfield, B. Xue, J. Meng, F. Huang, P. Romero, V. N. Uversky and A. K. Dunker. 'Exploring the binding diversity of intrinsically disordered proteins involved in one-to-many binding'. In: *Protein Science* 22.3 (2013), pp. 258–273.

[39] J. Ries and P. Schwille. 'Fluorescence correlation spectroscopy'. In: *BioEssays* 34.5 (2012), pp. 361–368.

[40] O. Krichevsky and G. Bonnet. 'Fluorescence correlation spectroscopy: the technique and its applications'. In: *Reports on Progress in Physics* 65.2 (2002), p. 251.

[41] S. T. Hess, T. P.K. Girirajan and M. D. Mason. 'Ultra-high resolution imaging by fluorescence photoactivation localization microscopy'. In: *Biophysical journal* 91.11 (2006), pp. 4258–4272.

[42] T. A. Klar, S. Jakobs, M. Dyba, A. Egner and S. W. Hell. 'Fluorescence microscopy with diffraction resolution barrier broken by stimulated emission'. In: *Proceedings of the National Academy of Sciences* 97.15 (2000), pp. 8206–8210.

[43] M. J. Rust, M. Bates and X. Zhuang. 'Sub-diffraction-limit imaging by stochastic optical reconstruction microscopy (STORM)'. In: *Nature methods* 3.10 (2006), pp. 793–796.

[44] T. Ha, T. Enderle, D.F. Ogletree, D. S. Chemla, P. R. Selvin and S. Weiss. 'Probing the interaction between two single molecules: fluorescence resonance energy transfer between a single donor and a single acceptor'. In: *Proceedings of the National Academy of Sciences* 93.13 (1996), pp. 6264–6268.

[45] B. Bullard, T. Garcia, V. Benes, M. C. Leake, W. A. Linke and A. F. Oberhauser. 'The molecular elasticity of the insect flight muscle proteins projectin and kettin'. In: *Proceedings of the National Academy of Sciences* 103.12 (2006), pp. 4451–4456.

[46] B. Bullard, C. Ferguson, A. Minajeva, M. C. Leake, M. Gautel, D. Labeit, L. Ding, S. Labeit, J. Horwitz, K. R. Leonard et al. 'Association of the chaperone αB-crystallin with titin in heart muscle'. In: *Journal of Biological Chemistry* 279.9 (2004), pp. 7917–7924.

[47] M. C. Leake, A. Grützner, M. Krüger and W. A. Linke. 'Mechanical properties of cardiac titin's N2B-region by single-molecule atomic force spectroscopy'. In: *Journal of structural biology* 155.2 (2006), pp. 263–272.

[48] A. Küchler, M. Yoshimoto, S. Luginbühl, F. Mavelli and P. Walde. 'Enzymatic reactions in confined environments'. In: *Nature nanotechnology* 11.5 (2016), pp. 409–420.

[49] P. Anzenbacher Jr and M. A. Palacios. 'Polymer nanofibre junctions of attolitre volume serve as zeptomole-scale chemical reactors'. In: *Nature chemistry* 1.1 (2009), p. 80.

[50] B. Chatin, M. Mével, J. Devallière, L. Dallet, T. Haudebourg, P. Peuziat, T. Colombani, M. Berchel, O. Lambert, A. Edelman and B. Pitard. 'Liposome-based Formulation for Intracellular Delivery of Functional Proteins'. In: *Molecular Therapy - Nucleic Acids* 4 (2015), e244.

[51] S. Schmid, P. Stömmer, H. Dietz and C. Dekker. 'Nanopore electro-osmotic trap for the label-free study of single proteins and their conformations'. In: *Nature Nanotechnology* 16.11 (2021), pp. 1244–1250.

[52] N. Klughammer and C. Dekker. 'Palladium zero-mode waveguides for optical single-molecule detection with nanopores'. In: *Nanotechnology* 32.18 (2021), 18LT01.

[53] M. Krishnan, N. Mojarad, P. Kukura and V. Sandoghdar. 'Geometry-induced electrostatic trapping of nanometric objects in a fluid'. In: *Nature* 467 (2010), pp. 692–695.

[54] R. Hölzel, N. Calander, Z. Chiragwandi, M. Willander and F. F. Bier. 'Trapping single molecules by dielectrophoresis'. In: *Physical review letters* 95.12 (2005), p. 128102.

[55] K.-T. Liao and C.-F. Chou. 'Nanoscale molecular traps and dams for ultrafast protein enrichment in high-conductivity buffers'. In: *Journal of the American Chemical Society* 134.21 (2012), pp. 8742–8745.

[56] B. Malekian, K. Xiong, G. Emilsson, J. Andersson, C. Fager, E. Olsson, E.M. Larsson-Langhammer and A.B Dahlin. 'Fabrication and Characterization of Plasmonic Nanopores with Cavities in the Solid Support'. In: *Sensors* 17 (2017), p. 1444.

[57] K. Jain, R. Vedarajan, M. Watanabe, M. Ishikiriyama and N. Matsumi. 'Tunable LCST behavior of poly(N-isopropylacrylamide/ionic liquid) copolymers'. In: *Polym. Chem.* 6 (38 2015), pp. 6819–6825.

[58] G. Emilsson, K. Xiong, Y. Sakiyama, B. Malekian, V. A. Gagnér, R. L. Schoch, R. Y. H. Lim and A. B. Dahlin. 'Polymer brushes in solid-state nanopores form an impenetrable entropic barrier for proteins'. In: *Nanoscale* 10.10 (2018), pp. 4663–4669.

[59] N. B. Eisele, A. A. Labokha, S. Frey, D. Görlich and R. P. Richter. 'Cohesiveness tunes assembly and morphology of FG nucleoporin domain meshworks–Implications for nuclear pore permeability'. In: *Biophysical journal* 105.8 (2013), pp. 1860–1870.

[60] H. Staudinger. 'Über Polymerisation'. In: *Berichte der deutschen chemischen Gesellschaft (A and B Series)* 53.6 (1920), pp. 1073–1085.

[61] E.D. Keoke and K.M. Porterfield. *Encyclopedia of American Indian Contributions to the World: 15,000 Years of Inventions and Innovations*. Facts on File library of American history. Facts On File, Incorporated, 2009.

[62] J. Tully. *The Devil's Milk: A Social History of Rubber*. New York University Press, 2011.

[63] M. Rubinstein and R.H. Colby. *Polymer Physics*. Oxford University Press, 2003.

[64] S. Z. D. Cheng. *Polymer Physics*. June. 2003, pp. 656–692.

[65] E.L Mackor and J.H van der Waals. 'The statistics of the adsorption of rod-shaped molecules in connection with the stability of certain colloidal dispersions'. In: *Journal of Colloid Science* 7.5 (1952), pp. 535–550.

[66] S. T. Milner. 'Polymer Brushes Published by : American Association for the Advancement of Science Stable URL : http://www.jstor.org/stable/2874899'. In: 251.4996 (1991), pp. 905–914.

[67] A. Halperin, M. Tirrell and T. P. Lodge. 'Macromolecules: Synthesis, Order and Advanced Properties'. In: *Macromolecules: Synthesis, Order and Advanced Properties* 100 (1992).

[68] B. Zhao and W. J. Brittain. 'Polymer brushes: Surface-immobilized macromolecules'. In: *Progress in Polymer Science (Oxford)* 25.5 (2000), pp. 677–710.

[69] T. B. McPherson, S. J. Lee and K. Park. 'Analysis of the Prevention of Protein Adsorption by Steric Repulsion Theory'. In: (1995), pp. 395–404.

[70] J. Klein, E. Kumacheva, D. Mahalu, D. Perahia and L. J. Fetters. 'Reduction of frictional forces between solid surfaces bearing polymer brushes'. In: *Nature* 370.6491 (1994), pp. 634–636.

[71] S. Alexander. 'Polymer adsorption on small spheres . A scaling approach'. In: *J. Phys.* 38.8 (1977), pp. 977–981.

[72] P.G. De Gennes. 'Scaling theory of polymer adsorption measured in porous structures or on polymers'. In: *J. Phys.* 37.12 (1976), pp. 1445–1452.

[73] R. Cantor. 'Nonionic diblock copolymers as surfactants between immiscible solvents'. In: *Macromolecules* 14.5 (1981), pp. 1186–1193.

[74] J.B. Field, C. Toprakcioglu, R.C. Ball, H.B. Stanley, L. Dai, W. Barford, J. Penfold, G. Smith and W. Hamilton. 'Determination of end-adsorbed polymer density profiles by neutron reflectometry'. In: *Macromolecules* 25.1 (1992), pp. 434–439.

[75] A. Karim, S.K. Satija, J.F. Douglas, J.F. Ankner and L.J. Fetters. 'Neutron reflectivity study of the density profile of a model end-grafted polymer brush: influence of solvent quality'. In: *Physical review letters* 73.25 (1994), p. 3407.

[76] P. G. de Gennes. *Scaling Concepts in Polymer Physics*. Cornell University Press, 1979.

[77] P. J. Flory. *Book Principles of Polymer Chemistry*. 1981.

[78] A. Halperin. 'Collapse of grafted chains in poor solvents'. In: *J. Phys.* 49.3 (1988), pp. 547–550.

[79] S. Minko. 'Responsive Polymer Brushes'. In: *Journal of Macromolecular Science, Part C: Polymer Reviews* 46.4 (2006), pp. 397–420.

[80] S. T. Milner, T. A. Witten and M. E. Cates. 'A parabolic density profile for grafted polymers'. In: *Europhys. letters* 5.5 (1988), pp. 413–418.

[81] G. Conzatti, S. Cavalie, C. Combes, J. Torrisani, N. Carrere and A. Tourrette. 'PNIPAM grafted surfaces through ATRP and RAFT polymerization: Chemistry and bioadhesion'. In: *Colloids and Surfaces B: Biointerfaces* 151 (2017), pp. 143–155.

[82] M. Henze, D. Mädge, O. Prucker and J. Rühe. '"Grafting through": mechanistic aspects of radical polymerization reactions with surface-attached monomers'. In: *Macromolecules* 47.9 (2014), pp. 2929–2937.

[83] G. Xie, A. Khabibullin, J. Pietrasik, J. Yan and K. Matyjaszewski. 'Polymer Brushes by Atom Transfer Radical Polymerization'. In: *Polymer and Biopolymer Brushes: For Materials Science and Biotechnology* i.1 (2017), pp. 29–95.

[84] J. O. Zoppe, N. C. Ataman, P. Mocny, J. Wang, J. Moraes and H. A. Klok. 'Surface-Initiated Controlled Radical Polymerization: State-of-the-Art, Opportunities, and Challenges in Surface and Interface Engineering with Polymer Brushes'. In: *Chemical Reviews* 117.3 (2017), pp. 1105–1318.

[85] M. Barsbay, O. Güven, T. P. Davis, C. Barner-Kowollik and L. Barner. 'RAFT-mediated polymerization and grafting of sodium 4-styrenesulfonate from cellulose initiated via γ-radiation'. In: *Polymer* 50.4 (2009), pp. 973–982.

[86] M. Barsbay, O. Güven, M. H. Stenzel, T. P. Davis, C. Barner-Kowollik and L. Barner. 'Verification of controlled grafting of styrene from cellulose via radiation-induced RAFT polymerization'. In: *Macromolecules* 40.20 (2007), pp. 7140–7147.

[87] D. Roy, M. Semsarilar, J. T. Guthrie and S. Perrier. 'Cellulose modification by polymer grafting: a review'. In: *Chemical Society Reviews* 38.7 (2009), pp. 2046–2064.

[88] S. Hansson, V. Trouillet, T. Tischer, A. S. Goldmann, A. Carlmark, C. Barner-Kowollik and E. Malmström. 'Grafting efficiency of synthetic polymers onto biomaterials: A comparative study of grafting-from versus grafting-to'. In: *Biomacromolecules* 14.1 (2013), pp. 64–74.

[89] C. Xue, B. C. Choi, S. Choi, P. V. Braun and D. E. Leckband. 'Protein adsorption modes determine reversible cell attachment on poly(N-isopropyl acrylamide) brushes'. In: *Advanced Functional Materials* 22.11 (2012), pp. 2394–2401.

[90] G. Ferrand-Drake del Castillo, G. Emilsson and A. Dahlin. 'Quantitative analysis of thickness and pH actuation of weak polyelectrolyte brushes'. In: *The Journal of Physical Chemistry C* 122.48 (2018), pp. 27516–27527.

[91] L. Michalek, L. Barner and C. Barner-Kowollik. 'Polymer on top: Current limits and future perspectives of quantitatively evaluating surface grafting'. In: *Advanced Materials* 30.21 (2018), p. 1706321.

[92] B. Lego, W. G. Skene and S. Giasson. 'Swelling study of responsive polyelectrolyte brushes grafted from mica substrates: Effect of pH, salt, and grafting density'. In: *Macromolecules* 43.9 (2010), pp. 4384–4393.

[93] Y. Zou, J. N. Kizhakkedathu and D. E. Brooks. 'Surface modification of polyvinyl chloride sheets via growth of hydrophilic polymer brushes'. In: *Macromolecules* 42.9 (2009), pp. 3258–3268.

[94] K. Binder, P. -G de Gennes, E.P. Giannelis, G.S. Grest, H. Hervet, R. Krishnamoorti, L. Leger, E. Manias, E. Raphael and S.-Q. Wang. *Polymers in confined environments - Advances in Polymer Science*. Vol. 138. Springer, 1999.

[95] C. M. Hui, J. Pietrasik, M. Schmitt, C. Mahoney, J. Choi, M. R. Bockstaller and K. Matyjaszewski. 'Surface-initiated polymerization as an enabling tool for multifunctional (Nano-)engineered hybrid materials'. In: *Chemistry of Materials* 26.1 (2014), pp. 745–762.

[96] K. Matyjaszewski. 'Controlled/living radical polymerization: State of the art in 2005'. In: (2006).

[97] K. Matyjaszewski, H. Dong, W. Jakubowski, J. Pietrasik and A. Kusumo. 'Grafting from Surfaces for "Everyone": ARGET ATRP in the Presence of Air'. In: *Langmuir* 23.8 (2007). PMID: 17371060, pp. 4528–4531.

[98] F. J. Xu, K. G. Neoh and E. T. Kang. 'Bioactive surfaces and biomaterials via atom transfer radical polymerization'. In: *Progress in Polymer Science (Oxford)* 34.8 (2009), pp. 719–761.

[99] C. J. Fristrup, K. Jankova and S. Hvilsted. 'Surface-initiated atom transfer radical polymerization - A technique to develop biofunctional coatings'. In: *Soft Matter* 5.23 (2009), pp. 4623–4634.

[100] S. Banerjee, T. K. Paira and T. K. Mandal. 'Surface confined atom transfer radical polymerization: Access to custom library of polymer-based hybrid materials for speciality applications'. In: *Polymer Chemistry* 5.14 (2014), pp. 4153–4167.

[101] M. Kato, M. Kamigaito, M. Sawamoto and T. Higashimura. 'Polymerization of Methyl Methacrylate with the Carbon Tetrachloride/Dichlorotris-(triphenylphosphine)ruthenium(II)/ Methylaluminum Bis(2,6-di-tert-butylphenoxide) Initiating System: Possibility of Living Radical Polymerization'. In: *Macromolecules* 28.5 (1995), pp. 1721–1723.

[102] J. S. Wang and K. Matyjaszewski. 'Controlled/"Living" Radical Polymerization. Atom Transfer Radical Polymerization in the Presence of Transition-Metal Complexes'. In: *Journal of the American Chemical Society* 117.20 (1995), pp. 5614–5615.

[103] Y. Kwak and K. Matyjaszewski. 'Photoirradiated atom transfer radical polymerization with an alkyl dithiocarbamate at ambient temperature'. In: *Macromolecules* 43.12 (2010), pp. 5180–5183.

[104] A. J. D. Magenau, N. C. Strandwitz, A. Gennaro and K. Matyjaszewski. 'Electrochemically Mediated Atom Transfer Radical Polymerization'. In: *Science* 332.6025 (2011), pp. 81–84.

[105] K. Min, H. Gao and K. Matyjaszewski. 'Use of ascorbic acid as reducing agent for synthesis of well-defined polymers by ARGET ATRP'. In: *Macromolecules* 40.6 (2007), pp. 1789–1791.

[106] Hui-Chun Lee, Markus Antonietti and Bernhard VKJ Schmidt. 'A Cu (II) metal–organic framework as a recyclable catalyst for ARGET ATRP'. In: *Polymer Chemistry* 7.47 (2016), pp. 7199–7203.

[107] G. Kickelbick, U. Reinöhl, T. S. Ertel, H. Bertagnolli and K. Matyjaszewski. *The Copper Catalyst in Atom Transfer Radical Polymerizations: Structural Observations*. ACS Symposium Series. 768, 2000. Chap. 15, pp. 211–222.

[108] K. Matyjaszewski. 'Atom Transfer Radical Polymerization (ATRP): Current Status and Future Perspectives'. In: *Macromolecules* 45.10 (2012), pp. 4015–4039.

[109] M. Horn and K. Matyjaszewski. 'Solvent Effects on the Activation Rate Constant in Atom Transfer Radical Polymerization'. In: *Macromolecules* 46.9 (2013), pp. 3350–3357.

[110] F. Seeliger and K. Matyjaszewski. 'Temperature Effect on Activation Rate Constants in ATRP: New Mechanistic Insights into the Activation Process'. In: *Macromolecules* 42.16 (2009), pp. 6050–6055.

[111] J. Morick, M. Buback and K. Matyjaszewski. 'Effect of Pressure on Activation–Deactivation Equilibrium Constants for ATRP of Methyl Methacrylate'. In: *Macromolecular Chemistry and Physics* 213.21 (2012), pp. 2287–2292.

[112] G. Emilsson, R. L. Schoch, P. Oertle, K. Xiong, R.Y.H. Lim and A. B. Dahlin. 'Surface plasmon resonance methodology for monitoring polymerization kinetics and morphology changes of brushes—evaluated with poly(N-isopropylacrylamide)'. In: *Applied Surface Science* 396 (2017), pp. 384–392.

[113] G. Emilsson, R. L. Schoch, L. Feuz, F. Höök, R. Y. H. Lim and A. B. Dahlin. 'Strongly stretched protein resistant poly (ethylene glycol) brushes prepared by grafting-to'. In: *ACS applied materials & interfaces* 7.14 (2015), pp. 7505–7515.

[114] G. Pasut and F.M. Veronese. 'Polymer–drug conjugation, recent achievements and general strategies'. In: *Progress in polymer science* 32.8-9 (2007), pp. 933–961.

[115] R. Duncan, M.J. Vicent, F. Greco and R.I. Nicholson. 'Polymer-drug conjugates: towards a novel approach for the treatment of endrocine-related cancer'. In: *Endocrine related cancer* 12.1 (2005), S189.

[116] G. Pasut and F. M. Veronese. 'State of the art in PEGylation: the great versatility achieved after forty years of research'. In: *Journal of controlled release* 161.2 (2012), pp. 461–472.

[117] G. Pasut, F. Greco, A. Mero, R. Mendichi, C. Fante, R. J. Green and F. M. Veronese. 'Polymer-drug conjugates for combination anticancer therapy: investigating the mechanism of action'. In: *Journal of Medicinal Chemistry* 52.20 (2009), pp. 6499–6502.

[118] S. Schöttler, G. Becker, S. Winzen, T. Steinbach, K. Mohr, K. Landfester, V. Mailänder and F. R. Wurm. 'Protein adsorption is required for stealth effect of poly (ethylene glycol)-and poly (phosphoester)-coated nanocarriers'. In: *Nature nanotechnology* 11.4 (2016), pp. 372–377.

[119] K. Knop, D. Hoogenboom R.and Fischer and U. S. Schubert. 'Poly (ethylene glycol) in drug delivery: pros and cons as well as potential alternatives'. In: *Angewandte chemie international edition* 49.36 (2010), pp. 6288–6308.

[120] J. Jin, Y. Han, C. Zhang, J. Liu, W. Jiang, J. Yin and H. Liang. 'Effect of grafted PEG chain conformation on albumin and lysozyme adsorption: A combined study using QCM-D and DPI'. In: *Colloids and Surfaces B: Biointerfaces* 136 (2015), pp. 838–844.

[121] W. Taylor and R. A.L. Jones. 'Protein adsorption on well-characterized polyethylene oxide brushes on gold: Dependence on molecular weight and grafting density'. In: *Langmuir* 29.20 (2013), pp. 6116–6122.

[122] S. Gon, B. Fang and M.M. Santore. 'Interaction of cationic proteins and polypeptides with biocompatible cationically-anchored PEG brushes'. In: *Macromolecules* 44.20 (2011), pp. 8161–8168.

[123] A. S. Hoffman. 'The early days of PEG and PEGylation (1970s–1990s)'. In: *Acta biomaterialia* 40 (2016), pp. 1–5.

[124] E.L. Furness, A. Ross, T.P. Davis and G.C. King. 'A hydrophobic interaction site for lysozyme binding to polyethylene glycol and model contact lens polymers'. In: *Biomaterials* 19.15 (1998), pp. 1361–1369.

[125] J. Bloustine, T. Virmani, G.M. Thurston and S. Fraden. 'Light scattering and phase behavior of lysozyme-poly (ethylene glycol) mixtures'. In: *Physical Review Letters* 96.8 (2006), p. 087803.

[126] S. J. Sofia, V. Premnath and E. W. Merrill. 'Poly (ethylene oxide) grafted to silicon surfaces: grafting density and protein adsorption'. In: *Macromolecules* 31.15 (1998), pp. 5059–5070.

[127] S. R. Benhabbour, L. Liu, H. Sheardown and A. Adronov. 'Protein resistance of surfaces prepared by chemisorption of monothiolated poly (ethylene glycol) to gold and dendronization with aliphatic polyester dendrons: Effect of hydrophilic dendrons'. In: *Macromolecules* 41.7 (2008), pp. 2567–2576.

[128] N. Ngadi, J. Abrahamson, C. Fee and K. Morison. 'QCM-D study on relationship of PEG coated stainless steel surfaces to protein resistance'. In: *International Journal of Chemical and Molecular Engineering* 2.11 (2008), pp. 315–319.

[129] J. Wu, Z. Wang, W. Lin and S. Chen. 'Investigation of the interaction between poly (ethylene glycol) and protein molecules using low field nuclear magnetic resonance'. In: *Acta biomaterialia* 9.5 (2013), pp. 6414–6420.

[130] J. Wu, C. Zhao, W. Lin, R. Hu, Q. Wang, H. Chen, L. Li, S. Chen and J. Zheng. 'Binding characteristics between polyethylene glycol (PEG) and proteins in aqueous solution'. In: *Journal of Materials Chemistry B* 2.20 (2014), pp. 2983–2992.

[131] P. Kingshott, S. McArthur, H. Thissen, D. G. Castner and H. J. Griesser. 'Ultrasensitive probing of the protein resistance of PEG surfaces by secondary ion mass spectrometry'. In: *Biomaterials* 23.24 (2002), pp. 4775–4785.

[132] W. Dai, C. Zheng, B. Zhao, K. Chen, P. Jia, J. Yang and J. Zhao. 'A negative correlation between water content and protein adsorption on polymer brushes'. In: *Journal of Materials Chemistry B* 7.13 (2019), pp. 2162–2168.

[133] S. Sharma, R. W. Johnson and T. A. Desai. 'XPS and AFM analysis of antifouling PEG interfaces for microfabricated silicon biosensors'. In: *Biosensors and Bioelectronics* 20.2 (2004), pp. 227–239.

[134] C. Xue, N. Yonet-Tanyeri, N. Brouette, M. Sferrazza, P. V. Braun and D. E. Leckband. 'Protein adsorption on poly (N-isopropylacrylamide) brushes: dependence on grafting density and chain collapse'. In: *Langmuir* 27.14 (2011), pp. 8810–8818.

[135] G. L. Kenausis, J. Vörös, D. L. Elbert, N. Huang, R. Hofer, L. Ruiz-Taylor, M. Textor, J. A. Hubbell and N. D. Spencer. 'Poly(L-lysine)-g-poly (ethylene glycol) layers on metal oxide surfaces: Attachment mechanism and effects of polymer architecture on resistance to protein adsorption'. In: *The Journal of Physical Chemistry B* 104.14 (2000), pp. 3298–3309.

[136] P. Kingshott, H. Thissen and H. J. Griesser. 'Effects of cloud-point grafting, chain length, and density of PEG layers on competitive adsorption of ocular proteins'. In: *Biomaterials* 23.9 (2002), pp. 2043–2056.

[137] S. Dai, P. Ravi and Kam C. Tam. 'pH-Responsive polymers: synthesis, properties and applications'. In: *Soft Matter* 4 (3 2008), pp. 435–449.

[138] M. Heskins and J. E. Guillet. 'Solution Properties of Poly(N-isopropylacrylamide)'. In: *Journal of Macromolecular Science: Part A - Chemistry* 2.8 (1968), pp. 1441–1455.

[139] D. Davis, A. Hamilton, Yang. J., L.D. Cremar, D. Van Gough, S.L. Potisek, M.T. Ong, T.J. Martinez, S.R. White, J.S. Moore and N.R. Sottos. 'Force-induced activation of covalent bonds in mechanoresponsive polymeric materials'. In: *Nature* 459 (2009), pp. 68–72.

[140] T. Tanaka, I. Nishio, S. Sun and S. UENO-NISHIO. 'Collapse of Gels in an Electric Field'. In: *Science* 218.4571 (1982), pp. 467–469.

[141] J. Thévenot, H. Oliveira, O. Sandre and S. Lecommandoux. 'Magnetic responsive polymer composite materials'. In: *Chem. Soc. Rev.* 42 (17 2013), pp. 7099–7116.

[142] A. S. Hoffman. '"Intelligent" Polymers in Medicine and Biotechnology'. In: *Artificial Organs* 19.5 (1995), pp. 458–467.

[143] P. Theato. 'Synthesis of well-defined polymeric activated esters'. In: *Journal of Polymer Science Part A: Polymer Chemistry* 46.20 (2008), pp. 6677–6687.

[144] J. Hu and S. Liu. 'Responsive Polymers for Detection and Sensing Applications: Current Status and Future Developments'. In: *Macromolecules* 43.20 (2010), pp. 8315–8330.

[145] A.K. Bajpai, K. S. Shukla, S. Bhanu and S. Kankane. 'Responsive polymers in controlled drug delivery'. In: *Progress in Polymer Science* 33.11 (2008), pp. 1088–1118.

[146] M. W. Urban. 'Stratification, stimuli-responsiveness, self-healing, and signaling in polymer networks'. In: *Progress in Polymer Science* 34.8 (2009), pp. 679–687.

[147] D. V. Andreeva, D. Fix, H. Möhwald and D. G. Shchukin. 'Self-Healing Anticorrosion Coatings Based on pH-Sensitive Polyelectrolyte/Inhibitor Sandwichlike Nanostructures'. In: *Advanced Materials* 20.14 (2008), pp. 2789–2794.

[148] C. Alexander and K. M. Shakesheff. 'Responsive polymers at the biology/materials science interface'. In: *Advanced Materials* 18.24 (2006), pp. 3321–3328.

[149] E.H. Specht, Neuman A., Neher H.T. (to Rohm and Haas Co). *US2773063A*. Dec. 1956. URL: https://patents.google.com/patent/US2773063A/en.

[150] C. De Las Heras Alarcón, T. Farhan, V. L. Osborne, W. T.S. Huck and C. Alexander. 'Bioadhesion at micro-patterned stimuli-responsive polymer brushes'. In: *Journal of Materials Chemistry* 15.21 (2005), pp. 2089–2094.

[151] J. J.I. Ramos and S. E. Moya. 'Water content of hydrated polymer brushes measured by an in situ combination of a quartz crystal microbalance with dissipation monitoring and spectroscopic ellipsometry'. In: *Macromolecular Rapid Communications* 32.24 (2011), pp. 1972–1978.

[152] L. Linhui, Z. Yang, L. Bo and G. Changyou. 'Fabrication of thermoresponsive polymer gradients for study of cell adhesion and detachment'. In: *Langmuir* 24.23 (2008), pp. 13632–13639.

[153] K. Nagase, M. Yamato, H. Kanazawa and T. Okano. 'Poly(N-isopropylacrylamide)-based thermoresponsive surfaces provide new types of biomedical applications'. In: *Biomaterials* 153 (2018), pp. 27–48.

[154] A. Halperin and M. Kröger. 'Theoretical considerations on mechanisms of harvesting cells cultured on thermoresponsive polymer brushes'. In: *Biomaterials* 33.20 (2012), pp. 4975–4987.

[155] A. Halperin, G. Fragneto, A. Schollier and M. Sferrazza. 'Primary versus Ternary Adsorption of Proteins onto PEG Brushes'. In: *Langmuir* 23.21 (2007). PMID: 17803323, pp. 10603–10617.

[156] A. Halperin and M. Kröger. 'Ternary Protein Adsorption onto Brushes: Strong versus Weak'. In: *Langmuir* 25.19 (2009). PMID: 19673469, pp. 11621–11634.

[157] F. Fang and I. Szleifer. 'Kinetics and Thermodynamics of Protein Adsorption: A Generalized Molecular Theoretical Approach'. In: *Biophysical Journal* 80.6 (2001), pp. 2568–2589.

[158] N. Willem. 'Adsorption of proteins from solution at the solid-liquid interface'. In: *Advances in Colloid and Interface Science* 25 (1986), pp. 267–340.

[159] J. Fang and C. M. Knobler. 'Phase-Separated Two-Component Self-Assembled Organosilane Monolayers and Their Use in Selective Adsorption of a Protein'. In: *Langmuir* 12.5 (1996), pp. 1368–1374.

[160] N. Xue, X. P. Qiu, V. Aseyev and F. M. Winnik. 'Nonequilibrium Liquid-Liquid Phase Separation of Poly(N-isopropylacrylamide) in Water/Methanol Mixtures'. In: *Macromolecules* 50.11 (2017), pp. 4446–4453.

[161] Y. Yu, M. Cirelli, B. D. Kieviet, E. S. Kooij, G. J. Vancso and S. de Beer. 'Tunable friction by employment of co-non-solvency of PNIPAM brushes'. In: *Polymer* 102 (2016), pp. 372–378.

[162] T. Fukai, N. Shinyashiki, S. Yagihara, R. Kita and F. Tanaka. 'Phase Behavior of Co-Nonsolvent Systems: Poly(N-isopropylacrylamide) in Mixed Solvents of Water and Methanol'. In: *Langmuir* 34.9 (2018), pp. 3003–3009.

[163] I. Bischofberger, D. C.E. Calzolari and V. Trappe. 'Co-nonsolvency of PNiPAM at the transition between solvation mechanisms'. In: *Soft Matter* 10.41 (2014), pp. 8288–8295.

[164] F. Tanaka, T. Koga and F. M. Winnik. 'Temperature-Responsive Polymers in Mixed Solvents: Competitive Hydrogen Bonds Cause Cononsolvency'. In: *Phys. Rev. Lett.* 101 (2 July 2008), p. 028302.

[165] F. Tanaka, T. Koga, H. Kojima and F. M. Winnik. 'Temperature- and Tension-Induced Coil-Globule Transition of Poly(N-isopropylacrylamide) Chains in Water and Mixed Solvent of Water/Methanol'. In: *Macromolecules* 42.4 (2009), pp. 1321–1330.

[166] F. Tanaka, T. Koga, I. Kaneda and F. M. Winnik. 'Hydration, phase separation and nonlinear rheology of temperature-sensitive water-soluble polymers'. In: *Journal of Physics: Condensed Matter* 23.28 (June 2011), p. 284105.

[167] J. Walter, J. Sehrt, J. Vrabec and H. Hasse. 'Molecular Dynamics and Experimental Study of Conformation Change of Poly(N-isopropylacrylamide) Hydrogels in Mixtures of Water and Methanol'. In: *The Journal of Physical Chemistry B* 116.17 (2012). PMID: 22432852, pp. 5251–5259.

[168] A. Pomorska, K. Wolski, A. Puciul-Malinowska and S. Zapotoczny. 'Tailored conditions for controlled and fast growth of surface-grafted PNIPAM brushes'. In: *Polymer* 97 (2016), pp. 380–386.

[169] G. Zhang and C. Wu. 'Reentrant coil-to-globule-to-coil transition of a single linear homopolymer chain in a water/methanol mixture'. In: *Physical Review Letters* 86.5 (2001), pp. 822–825.

[170] G. Zhang and C. Wu. 'The water/methanol complexation induced reentrant coil-to-globule-to-coil transition of individual homopolymer chains in extremely dilute solution'. In: *Journal of the American Chemical Society* 123.7 (2001), pp. 1376–1380.

[171] K. Kyriakos, M. Philipp, L. Silvi, W. Lohstroh, W. Petry, P. Müller-Buschbaum and C. M. Papadakis. 'Solvent Dynamics in Solutions of PNIPAM in Water/Methanol Mixtures-A Quasi-Elastic Neutron Scattering Study'. In: *Journal of Physical Chemistry B* 120.20 (2016), pp. 4679–4688.

[172] S. Nian and L. Pu. 'Racemic Fluorescence Probe for Enantiomeric Excess Determination: Application of Cononsolvency of a Polymer in Sensing'. In: *The Journal of Organic Chemistry* 84.2 (2019), pp. 909–913.

[173] Y. Yu, R. A. Lopez de la Cruz, B. D. Kieviet, H. Gojzewski, A. Pons, G. Julius Vancso and S. de Beer. 'Pick up, move and release of nanoparticles utilizing co-non-solvency of PNIPAM brushes'. In: *Nanoscale* 9 (4 2017), pp. 1670–1675.

[174] Deborah Leckband and Jacob Israelachvili. 'Intermolecular forces in biology'. In: *Quarterly reviews of biophysics* 34.2 (2001), pp. 105–267.

[175] H.-J. Butt, G. Karlheinz and M. Kappl. *Physics and Chemistry of Interfaces*. Vol. I. WILEY-VCH GmbH and Co. KGaA, 1995, pp. 255–257.

[176] G. Trefalt and M. Borkovec. *Overview of DLVO Theory*. Accessed: 10-04-2018, 15:48. URL: www.colloid.ch/dlvo.

[177] P. D. Ross and S. Subramanian. 'Thermodynamics of protein association reactions: forces contributing to stability'. In: *Biochemistry* 20.11 (1981), pp. 3096–3102.

[178] C. N. Pace, B. A. Shirley, M. McNutt and K. Gajiwala. 'Forces contributing to the conformational stability of proteins'. In: *The FASEB journal* 10.1 (1996), pp. 75–83.

[179] R. W. Newberry and R. T. Raines. 'Secondary forces in protein folding'. In: *ACS chemical biology* 14.8 (2019), pp. 1677–1686.

[180] K.H. Jürgen Buschow, R.W. Cahn, M.C. Flemings, B. Ilschner, E.J. Kramer, S. Mahajan and P. Veyssière. *Encyclopedia of Materials: Science and Technology*. Elsevier Science Ltd, 2001.

[181] S.-J. Park and M.-K. Seo. *Chapter 1 - Intermolecular Force*. Vol. 18. Interface Science and Technology. Elsevier, 2011, pp. 1–57.

[182] D. N. Petsev. *Chapter 8 Theory of emulsion flocculation*. Vol. 4. C. Elsevier Masson SAS, 2004, pp. 313–350.

[183] J. Marra and J. Israelachvili. 'Direct measurements of forces between phosphatidylcholine and phosphatidylethanolamine bilayers in aqueous electrolyte solutions'. In: *Biochemistry* 24.17 (1985), pp. 4608–4618.

[184] J. Marra. 'Controlled deposition of lipid monolayers and bilayers onto mica and direct force measurements between galactolipid bilayers in aqueous solutions'. In: *Journal of colloid and interface science* 107.2 (1985), pp. 446–458.

[185] C. M. Roth and A. M. Lenhoff. 'Electrostatic and van der Waals contributions to protein adsorption: computation of equilibrium constants'. In: *Langmuir* 9.4 (1993), pp. 962–972.

[186] C. M. Roth, B. L. Neal and A. M. Lenhoff. 'Van der Waals interactions involving proteins'. In: *Biophysical journal* 70.2 (1996), pp. 977–987.

[187] W. Arnold, S. Hunklinger and K. Dransfeld. 'Influence of optical absorption on the Van der Waals interaction between solids'. In: *Physical Review B* 19.12 (1979), p. 6049.

[188] X. Zhang, Y. He, M. L. Sushko, J. Liu, L. Luo, J. J. De Yoreo, S. X. Mao, C. Wang and K. M. Rosso. 'Direction-specific van der Waals attraction between rutile TiO2 nanocrystals'. In: *Science* 356.6336 (2017), pp. 434–437.

[189] A. C. Zettlemoyer. 'Hydrophobic surfaces'. In: *Journal of Colloid and Interface Science* 28.3-4 (1968), pp. 343–369.

[190] H. K. Christenson and P. M. Claesson. 'Direct measurements of the force between hydrophobic surfaces in water'. In: *Advances in Colloid and Interface Science* 91.3 (2001), pp. 391–436.

[191] H.K. Christenson, P.M. Claesson, J. Berg and P.C. Herder. 'Forces between fluorocarbon surfactant monolayers: Salt effects on the hydrophobic interaction'. In: *The Journal of Physical Chemistry* 93.4 (1989), pp. 1472–1478.

[192] H. K. Christenson, J. Fang, B. W. Ninham and J. L. Parker. 'Effect of divalent electrolyte on the hydrophobic attraction'. In: *Journal of Physical Chemistry* 94.21 (1990), pp. 8004–8006.

[193] M. Banach, P. Fabian, K. Stapor, L. Konieczny et al. 'Structure of the Hydrophobic Core Determines the 3D Protein Structure—Verification by Single Mutation Proteins'. In: *Biomolecules* 10.5 (2020), p. 767.

[194] B. Kalinowska, M. Banach, Z. Wiśniowski, L. Konieczny and I. Roterman. 'Is the hydrophobic core a universal structural element in proteins?' In: *Journal of Molecular Modeling* 23.7 (2017), pp. 1–16.

[195] D. R. Schmidt, H. Waldeck and W. J. Kao. 'Protein adsorption to biomaterials'. In: *Biological interactions on materials surfaces*. Springer, 2009, pp. 1–18.

[196] K. Nakanishi, T. Sakiyama and K. Imamura. 'On the adsorption of proteins on solid surfaces, a common but very complicated phenomenon'. In: *Journal of bioscience and bioengineering* 91.3 (2001), pp. 233–244.

[197] K. C. Dee, D. A. Puleo and R. Bizios. 'An introduction to tissue-biomaterial interactions'. In: *Cell Mol. Biol* 8 (2004), pp. 419–425.

[198] A. Jungbauer, C. Machold and R. Hahn. 'Hydrophobic interaction chromatography of proteins: III. Unfolding of proteins upon adsorption'. In: *Journal of Chromatography A* 1079.1-2 (2005), pp. 221–228.

[199] G. D. Rose and R. Wolfenden. 'Hydrogen bonding, hydrophobicity, packing, and protein folding'. In: *Annual review of biophysics and biomolecular structure* 22.1 (1993), pp. 381–415.

[200] E. N. Baker and R. E. Hubbard. 'Hydrogen bonding in globular proteins'. In: *Progress in biophysics and molecular biology* 44.2 (1984), pp. 97–179.

[201] C. N. Pace. '[24] Evaluating contribution of hydrogen bonding and hydrophobic bonding to protein folding'. In: *Methods in enzymology*. Vol. 259. Elsevier, 1995, pp. 538–554.

[202] D. F. Sticke, L. G. Presta, K. A. Dill and G. D. Rose. 'Hydrogen bonding in globular proteins'. In: *Journal of molecular biology* 226.4 (1992), pp. 1143–1159.

[203] H. Raether. *Surface plasmons on smooth and Rough Surfaces and on Gratings*. Vol. 111. Springer Tracts in Modern Physics. Springer, 1981.

[204] R. H. Ritchie. 'Plasma Losses by Fast Electrons in Thin Films'. In: *Phys. Rev.* 106 (5 June 1957), pp. 874–881.

[205] C. J. Powell and J. B. Swan. 'Effect of Oxidation on the Characteristic Loss Spectra of Aluminum and Magnesium'. In: *Phys. Rev.* 118 (3 May 1960), pp. 640–643.

[206] A. Otto. 'Excitation of nonradiative surface plasma waves in silver by the method of frustrated total reflection'. In: *Z. Physik* 216 (1968), pp. 398–410.

[207] E. Kretschmann and H. Raether. 'Notizen: Radiative Decay of Non Radiative Surface Plasmons Excited by Light'. In: *Zeitschrift für Naturforschung A* 23.12 (1968), pp. 2135–2136.

[208] A.D. Boardman. *Electromagnetic Surface Modes*. John Wiley & Sons, 1982.

[209] A.B. Dahlin. *Plasmonic Biosensors: An Integrated View of Refractometric Detection*. IOS press BV, 2012.

[210] K. Xiong, G. Emilsson and A. B. Dahlin. 'Biosensing using plasmonic nanohole arrays with small, homogenous and tunable aperture diameters'. In: *Analyst* 141 (12 2016), pp. 3803–3810.

[211] T. Sannomiya, O. Scholder, K. Jefimovs, C. Hafner and A. B. Dahlin. 'Investigation of plasmon resonances in metal films with nanohole arrays for biosensing applications'. In: *Small* 7.12 (2011), pp. 1653–1663.

[212] L. S. Jung, Charles T. Campbell, Timothy M. Chinowsky, Mimi N. Mar and Sinclair S. Yee. 'Quantitative Interpretation of the Response of Surface Plasmon Resonance Sensors to Adsorbed Films'. In: *Langmuir* 14.19 (1998), pp. 5636–5648.

[213] J. Homola. 'Surface Plasmon Resonance Sensors for Detection of Chemical and Biological Species'. In: *Chemical reviews* 108 (Mar. 2008), pp. 462–93.

[214] S.A. Maier. *Plasmonics. Fundamentals and Applications*. Springer, 2007.

[215] R. B. M. Schasfoort. 'Chapter 1:Introduction to surface plasmon resonance'. In: *Handbook of Surface Plasmon Resonance (2)* (2017), pp. 1–26.

[216] C.C. Homes, Q. Du, C. Petrovic, W.H. Brito, S. Choi and G. Kotliar. 'Unusual electronic and vibrational properties in the colossal thermopower material FeSb2'. In: *Scientific reports* 8.1 (2018), pp. 1–9.

[217] L. S. Jung, C. T. Campbell, T. M. Chinowsky, M. N. Mar and S. S. Yee. 'Quantitative Interpretation of the Response of Surface Plasmon Resonance Sensors to Adsorbed Films'. In: *Langmuir* 14.19 (1998), pp. 5636–5648.

[218] R. L. Schoch and R. Y. H. Lim. 'Non-Interacting Molecules as Innate Structural Probes in Surface Plasmon Resonance'. In: *Langmuir* 29.12 (2013). PMID: 23437874, pp. 4068–4076.

[219] J. Andersson, G. Ferrand-Drake del Castillo, P. Bilotto, F. Höök, M. Valtiner and A. Dahlin. 'Control of polymer brush morphology, rheology, and protein repulsion by hydrogen bond complexation'. In: *Langmuir* 37.16 (2021), pp. 4943–4952.

[220] H. Lee, D. H. Kim, H.-W. Park, N. A. Mahynski, K. Kim, M. Meron, B. Lin and Y.-Y. Won. 'Reduced water density in a poly (ethylene oxide) brush'. In: *The Journal of Physical Chemistry Letters* 3.12 (2012), pp. 1589–1595.

[221] J. Vörös. 'The density and refractive index of adsorbing protein layers'. In: *Biophysical journal* 87.1 (2004), pp. 553–561.

[222] B. Zeng, Y. Gao and F. J. Bartoli. 'Differentiating surface and bulk interactions in nanoplasmonic interferometric sensor arrays'. In: *Nanoscale* 7.1 (2015), pp. 166–170.

[223] T. M. Chinowsky and S. S. Yee. 'Data analysis and calibration for a bulk-refractive-index-compensated surface plasmon resonance affinity sensor'. In: *Fiber Optic Sensor Technology and Applications 2001*. Vol. 4578. International Society for Optics and Photonics. 2002, pp. 442–453.

[224] S. Löfås, M. Malmqvist, I. Rönnberg, E. Stenberg, B. Liedberg and I. Lundström. 'Bioanalysis with surface plasmon resonance'. In: *Sensors and Actuators B: Chemical* 5.1-4 (1991), pp. 79–84.

[225] J. Junesch, T. Sannomiya and A. B. Dahlin. 'Optical properties of nanohole arrays in metal–dielectric double films prepared by mask-on-metal colloidal lithography'. In: *ACS nano* 6.11 (2012), pp. 10405–10415.

[226] A. B. Dahlin, N. J. Wittenberg, F. Höök and S. H. Oh. 'Promises and challenges of nanoplasmonic devices for refractometric biosensing'. In: *Nanophotonics* 2.2 (2013), pp. 83–101.

[227] A. B. Dahlin, M. Mapar, K. Xiong, F. Mazzotta, F. Höök and T. Sannomiya. 'Plasmonic Nanopores in Metal-Insulator-Metal Films'. In: *Advanced Optical Materials* 2.6 (2014), pp. 556–564.

[228] J. Kundu, C. S. Levin and N. J. Halas. 'Real-time monitoring of lipid transfer between vesicles and hybrid bilayers on Au nanoshells using surface enhanced Raman scattering (SERS)'. In: *Nanoscale* 1.1 (2009), pp. 114–117.

[229] F. McKenzie, K. Faulds and D. Graham. 'Mixed metal nanoparticle assembly and the effect on surface-enhanced Raman scattering'. In: *Nanoscale* 2.1 (2010), pp. 78–80.

[230] F. Vetrone, R. Naccache, A. J. de la Fuente, F. Sanz-Rodriguez, A. Blazquez-Castro, E. M. Rodriguez, D. Jaque, J. G. Solé and J. A. Capobianco. 'Intracellular imaging of HeLa cells by non-functionalized NaYF4: Er 3+, Yb 3+ upconverting nanoparticles'. In: *Nanoscale* 2.4 (2010), pp. 495–498.

[231] A. B. Dahlin. 'Sensing applications based on plasmonic nanopores: The hole story'. In: *Analyst* 140 (14 2015), pp. 4748–4759.

[232] J. Junesch, G. Emilsson, K. Xiong, S. Kumar, T. Sannomiya, H. Pace, J. Vörös, S. Oh, M. Bally and A. B. Dahlin. 'Location-specific nanoplasmonic sensing of biomolecular binding to lipid membranes with negative curvature'. In: *Nanoscale* 7 (37 2015), pp. 15080–15085.

[233] F. Mazzotta, T. W. Johnson, A. B Dahlin, J. Shaver, S. Oh and F. Höök. 'Influence of the evanescent field decay length on the sensitivity of plasmonic nanodisks and nanoholes'. In: *Acs Photonics* 2.2 (2015), pp. 256–262.

[234] I. Reviakine, D. Johannsmann and R. P. Richter. 'Hearing what you cannot see and visualizing what you hear: Interpreting quartz crystal microbalance data from solvated interfaces'. In: *Analytical Chemistry* 83.23 (2011), pp. 8838–8848.

[235] M. D. Ward and D. A. Buttry. 'In Situ Interfacial Mass Detection with Piezoelectric Transducers'. In: *Science* 249.4972 (1990), pp. 1000–1007.

[236] M. C. Dixon. 'Quartz crystal microbalance with dissipation monitoring: Enabling real-time characterization of biological materials and their interactions'. In: *Journal of Biomolecular Techniques* 19.3 (2008), pp. 151–158.

[237] D. Johannsmann, I. Reviakine and Ralf P. Richter. 'Dissipation in films of adsorbed nanospheres studied by quartz crystal microbalance (QCM)'. In: *Analytical Chemistry* 81.19 (2009), pp. 8167–8176.

[238] W. Yang, D. Li, X. D. Chen and R. Mercadé-Prieto. 'Effect of calcium on the fouling of whey protein isolate on stainless steel using QCM-D'. In: *Chemical Engineering Science* 177 (2018), pp. 501–508.

[239] P. J. Molino, O. M. Hodson, J. F. Quinn and R. Wetherbee. 'Utilizing QCM-D to characterize the adhesive mucilage secreted by two marine diatom species in-situ and in real-time'. In: *Biomacromolecules* 7.11 (2006), pp. 3276–3282.

[240] Q. Chen, W. Tang, D. Wang, X. Wu, N. Li and F. Liu. 'Amplified QCM-D biosensor for protein based on aptamer-functionalized gold nanoparticles'. In: *Biosensors and Bioelectronics* 26.2 (2010), pp. 575–579.

[241] M. Rodahl and B. Kasemo. 'On the measurement of thin liquid overlayers with the quartz-crystal microbalance'. In: *Sensors and Actuators A: Physical* 54.1-3 (1996), pp. 448–456.

[242] X. Huang, Q. Bai, J. Hu and D. Hou. 'A practical model of quartz crystal microbalance in actual applications'. In: *Sensors* 17.8 (2017), p. 1785.

[243] M. V. Voinova, M. Rodahl, M. Jonson and B. Kasemo. 'Viscoelastic acoustic response of layered polymer films at fluid-solid interfaces: continuum mechanics approach'. In: *Physica Scripta* 59.5 (1999), p. 391.

[244] J. Iruthayaraj, G. Olanya and Per M. Claesson. 'Viscoelastic properties of adsorbed bottle-brush polymer layers studied by quartz crystal microbalance -dissipation measurements'. In: *Journal of Physical Chemistry C* 112.38 (2008), pp. 15028–15036.

[245] G. Liu, H. Cheng, L. Yan and G. Zhang. 'Study of the kinetics of the pancake-to-brush transition of poly(N-isopropylacrylamide) chains'. In: *Journal of Physical Chemistry B* 109.47 (2005), pp. 22603–22607.

[246] D. Johannsmann. 'Viscoelastic analysis of organic thin films on quartz resonators'. In: *Macromolecular Chemistry and Physics* 200.3 (1999), pp. 501–516.

[247] J. W. Lichtman and J.-A. Conchello. 'Fluorescence microscopy'. In: *Nature methods* 2.12 (2005), pp. 910–919.

[248] *ThermoFisherScientific*. Accessed: 2022-03-15. URL: https://www.thermofisher.com/order/fluorescence-spectraviewer!/.

[249] S. J. Sahl, S. W. Hell and S. Jakobs. 'Fluorescence nanoscopy in cell biology'. In: *Nature reviews Molecular cell biology* 18.11 (2017), pp. 685–701.

[250] W. E. Moerner and David. P. Fromm. 'Methods of single-molecule fluorescence spectroscopy and microscopy'. In: *Review of Scientific instruments* 74.8 (2003), pp. 3597–3619.

[251] C. Joo, H. Balci, Y. Ishitsuka, C. Buranachai and T. Ha. 'Advances in single-molecule fluorescence methods for molecular biology'. In: *Annu. Rev. Biochem.* 77 (2008), pp. 51–76.

[252] P. Anger, P. Bharadwaj and L. Novotny. 'Enhancement and quenching of single-molecule fluorescence'. In: *Physical review letters* 96.11 (2006), p. 113002.

[253] J. R. Lakowicz. *Principles of fluorescence spectroscopy*. Springer, 2006.

[254] B. Valeur. 'Introduction: On the origin of the terms fluorescence, phosphorescence, and luminescence'. In: *New Trends in Fluorescence Spectroscopy*. Springer, 2001, pp. 3–6.

[255] B. Valeur and J.-C. Brochon. *New trends in fluorescence spectroscopy: applications to chemical and life sciences*. Vol. 1. Springer Science & Business Media, 2012.

[256] B. Valeur and M. N. Berberan-Santos. *Molecular fluorescence: principles and applications*. John Wiley & Sons, 2012.

[257] C. A. Combs. 'Fluorescence microscopy: a concise guide to current imaging methods'. In: *Current protocols in neuroscience* 50.1 (2010), pp. 2–1.

[258] E. Abbe. 'Beiträge zur Theorie des Mikroskops und der mikroskopischen Wahrnehmung'. In: *Archiv für mikroskopische Anatomie* 9.1 (1873), pp. 413–468.

[259] G. B. Airy. 'On the diffraction of an object-glass with circular aperture'. In: *Transactions of the Cambridge Philosophical Society* 5 (1835), p. 283.

[260] S. Inoué. 'Foundations of confocal scanned imaging in light microscopy'. In: *Handbook of biological confocal microscopy*. Springer, 2006, pp. 1–19.

[261] L. Rayleigh. 'XV. On the theory of optical images, with special reference to the microscope'. In: *The London, Edinburgh, and Dublin Philosophical Magazine and Journal of Science* 42.255 (1896), pp. 167–195.

[262] M. Minsky. 'Confocal patent focal scanning microscope'. In: *US patent, serial* 3 (1957).

[263] J. S. Verdaasdonk, A. D. Stephens, J. Haase and K. Bloom. 'Bending the Rules: Widefield Microscopy and the Abbe Limit of Resolution'. In: *Journal of cellular physiology* 229.2 (2014), pp. 132–138.

[264] A. D. Elliott. 'Confocal microscopy: principles and modern practices'. In: *Current protocols in Cytometry* 92.1 (2020), e68.

[265] J. Jonkman, C. M. Brown, G. D. Wright, K. I. Anderson and A. J. North. 'Tutorial: guidance for quantitative confocal microscopy'. In: *Nature protocols* 15.5 (2020), pp. 1585–1611.

[266] L. Sfakis, T. Kamaldinov, M. Larsen, J. Castracane and A. Khmaladze. 'Quantification of Confocal images using LabVIEW for tissue engineering applications'. In: *Tissue Engineering Part C: Methods* 22.11 (2016), pp. 1028–1037.

[267] H. Sahoo. 'Förster resonance energy transfer–A spectroscopic nanoruler: Principle and applications'. In: *Journal of Photochemistry and Photobiology C: Photochemistry Reviews* 12.1 (2011), pp. 20–30.

[268] G. A. Jones and D. S. Bradshaw. 'Resonance energy transfer: from fundamental theory to recent applications'. In: *Frontiers in Physics* 7 (2019), p. 100.

[269] M. Y. Berezin and S. Achilefu. 'Fluorescence lifetime measurements and biological imaging'. In: *Chemical reviews* 110.5 (2010), pp. 2641–2684.

[270] A. A. Deniz, T. A. Laurence, G. S. Beligere, M. Dahan, A. B. Martin, D. S. Chemla, P. E. Dawson, P. G. Schultz and S. Weiss. 'Single-molecule protein folding: diffusion fluorescence resonance energy transfer studies of the denaturation of chymotrypsin inhibitor 2'. In: *Proceedings of the National Academy of Sciences* 97.10 (2000), pp. 5179–5184.

[271] M. Margittai, J. Widengren, E. Schweinberger, G. F. Schröder, S. Felekyan, E. Haustein, M. König, D. Fasshauer, H. Grubmüller, R. Jahn and C. A. M. Seidel. 'Single-molecule fluorescence resonance energy transfer reveals a dynamic equilibrium between closed and open conformations of syntaxin 1'. In: *Proceedings of the National Academy of Sciences* 100.26 (2003), pp. 15516–15521.

[272] B. Schuler and W. A. Eaton. 'Protein folding studied by single-molecule FRET'. In: *Current opinion in structural biology* 18.1 (2008), pp. 16–26.

[273] R. N. Day and M. W. Davidson. 'Fluorescent proteins for FRET microscopy: monitoring protein interactions in living cells'. In: *Bioessays* 34.5 (2012), pp. 341–350.

[274] B. K. Müller, E. Zaychikov, C. Bräuchle and D. C. Lamb. 'Pulsed interleaved excitation'. In: *Biophysical journal* 89.5 (2005), pp. 3508–3522.

[275] E. F. Y. Hom and A. S. Verkman. 'Analysis of Coupled Bimolecular Reaction Kinetics and Diffusion byTwo-Color Fluorescence Correlation Spectroscopy: Enhanced Resolution of Kinetics by Resonance Energy Transfer'. In: *Biophysical Journal* 83.1 (2002), pp. 533–546.

[276] C. Eggeling, P. Kask, D. Winkler and S. Jäger. 'Rapid analysis of Förster resonance energy transfer by two-color global fluorescence correlation spectroscopy: trypsin proteinase reaction'. In: *Biophysical journal* 89.1 (2005), pp. 605–618.

[277] K. Takemura. 'Surface plasmon resonance (SPR)-and localized SPR (LSPR)-based virus sensing systems: Optical vibration of nano-and micro-metallic materials for the development of next-generation virus detection technology'. In: *Biosensors* 11.8 (2021), p. 250.

[278] N. Ravindran, S. Kumar, M. CA, N. Thirunavookarasu S and S. CK. 'Recent advances in Surface Plasmon Resonance (SPR) biosensors for food analysis: A review'. In: *Critical Reviews in Food Science and Nutrition* (2021), pp. 1–23.

[279] V. S. Chaudhary, D. Kumar and S. Kumar. 'Gold-immobilized photonic crystal fiber-based SPR biosensor for detection of malaria disease in human body'. In: *IEEE Sensors Journal* 21.16 (2021), pp. 17800–17807.

[280] Y. Zhang and S. N. Riduan. 'Functional porous organic polymers for heterogeneous catalysis'. In: *Chemical Society Reviews* 41.6 (2012), pp. 2083–2094.

[281] Z. Zhang, B. Zandkarimi and A. N. Alexandrova. 'Ensembles of metastable states govern heterogeneous catalysis on dynamic interfaces'. In: *Accounts of chemical research* 53.2 (2020), pp. 447–458.

[282] M. K. Debe. 'Electrocatalyst approaches and challenges for automotive fuel cells'. In: *Nature* 486.7401 (2012), pp. 43–51.

[283] H. Liu, B. Wang, E. S.P. Leong, P. Yang, Y. Zong, G. Si, J. Teng and S. A. Maier. 'Enhanced surface plasmon resonance on a smooth silver film with a seed growth layer'. In: *ACS nano* 4.6 (2010), pp. 3139–3146.

[284] S. Szunerits, X. Castel and R. Boukherroub. 'Preparation of electrochemical and surface plasmon resonance active interfaces: deposition of indium tin oxide on silver thin films'. In: *The Journal of Physical Chemistry C* 112.29 (2008), pp. 10883–10888.

[285] M. Manesse, R. Sanjines, V. Stambouli, C. Jorel, B. Pelissier, M. Pisarek, R. Boukherroub and S. Szunerits. 'Preparation and characterization of silver substrates coated with antimony-doped SnO2 thin films for surface plasmon resonance studies'. In: *Langmuir* 25.14 (2009), pp. 8036–8041.

[286] J. W. Sadowski, J. Lekkala and I. Vikholm. 'Biosensors based on surface plasmons excited in non-noble metals'. In: *Biosensors and Bioelectronics* 6.5 (1991), pp. 439–444.

[287] A. D. Rakić, A. B. Djurišić, J. M. Elazar and M. L. Majewski. 'Optical properties of metallic films for vertical-cavity optoelectronic devices'. In: *Applied optics* 37.22 (1998), pp. 5271–5283.

[288] P.B. Johnson and R.W. Christy. 'Optical constants of transition metals: Ti, v, cr, mn, fe, co, ni, and pd'. In: *Physical review B* 9.12 (1974), p. 5056.

[289] K. J. Palm, J. B. Murray, T. C. Narayan and J. N. Munday. 'Dynamic optical properties of metal hydrides'. In: *Acs Photonics* 5.11 (2018), pp. 4677–4686.

[290] W. S.M. Werner, K. Glantschnig and C. Ambrosch-Draxl. 'Optical constants and inelastic electron-scattering data for 17 elemental metals'. In: *Journal of Physical and Chemical Reference Data* 38.4 (2009), pp. 1013–1092.

[291] J. A. Baird, R. Olayo-Valles, C. Rinaldi and L. S. Taylor. 'Effect of molecular weight, temperature, and additives on the moisture sorption properties of polyethylene glycol'. In: *Journal of pharmaceutical sciences* 99.1 (2010), pp. 154–168.

[292] F. Liu, X. Zhang, K. Li, T. Guo, A. Ianoul and J. Albert. 'Discrimination of bulk and surface refractive index change in plasmonic sensors with narrow bandwidth resonance combs'. In: *ACS sensors* 6.8 (2021), pp. 3013–3023.

[293] R. L. Rich and D. G. Myszka. 'Survey of the 2009 commercial optical biosensor literature'. In: *Journal of Molecular Recognition* 24.6 (2011), pp. 892–914.

[294] L. S. Jung, C. T. Campbell, T. M. Chinowsky, M. N. Mar and S. S. Yee. 'Quantitative interpretation of the response of surface plasmon resonance sensors to adsorbed films'. In: *Langmuir* 14.19 (1998), pp. 5636–5648.

[295] G. Emilsson, Y. Sakiyama, B. Malekian, K. Xiong, Z. Adali-Kaya, R. Y.H. Lim and A. B. Dahlin. 'Gating protein transport in solid state nanopores by single molecule recognition'. In: *ACS central science* 4.8 (2018), pp. 1007–1014.

[296] H. Zhao, P. H. Brown and P. Schuck. 'On the distribution of protein refractive index increments'. In: *Biophysical journal* 100.9 (2011), pp. 2309–2317.

[297] A. Stradner, H. Sedgwick, F. Cardinaux, W. C.K. Poon, S. U. Egelhaaf and P. Schurtenberger. 'Equilibrium cluster formation in concentrated protein solutions and colloids'. In: *Nature* 432.7016 (2004), pp. 492–495.

[298] A. Stradner, F. Cardinaux and P. Schurtenberger. 'A small-angle scattering study on equilibrium clusters in lysozyme solutions'. In: *The Journal of Physical Chemistry B* 110.42 (2006), pp. 21222–21231.

[299] *AlexaFluor488 bleaching rate*. Accessed: 2022-07-05. URL: https://www.thermofisher.com/se/en/home/brands/molecular-probes/key-molecular-probes-products/alexa-fluor/alexa-fluor-dyes-excellent-photostability.html.

[300] A. C. McUmber, T. W. Randolph and D. K. Schwartz. 'Electrostatic interactions influence protein adsorption (but not desorption) at the silica–aqueous interface'. In: *The journal of physical chemistry letters* 6.13 (2015), pp. 2583–2587.

[301] S. H. Brewer, W. R. Glomm, M. C. Johnson, M. K. Knag and S. Franzen. 'Probing BSA binding to citrate-coated gold nanoparticles and surfaces'. In: *Langmuir* 21.20 (2005), pp. 9303–9307.

[302] Q. Shi, Y. Zhou and Y. Sun. 'Influence of pH and ionic strength on the steric mass-action model parameters around the isoelectric point of protein'. In: *Biotechnology progress* 21.2 (2005), pp. 516–523.

[303] D. L. Huber, R. P. Manginell, M. A. Samara, B. Kim and B. C. Bunker. 'Programmed adsorption and release of proteins in a microfluidic device'. In: *Science* 301.5631 (2003), pp. 352–354.

[304] P. Shivapooja, L. K. Ista, H. E. Canavan and G. P. Lopez. 'ARGET–ATRP synthesis and characterization of PNIPAAm brushes for quantitative cell detachment studies'. In: *Biointerphases* 7.1 (2012), pp. 1–9.

[305] Q. Yu, L. M. Johnson and G. P. López. 'Nanopatterned Polymer Brushes for Triggered Detachment of Anchorage-Dependent Cells'. In: *Advanced Functional Materials* 24.24 (2014), pp. 3751–3759.

[306] J. C. Love, L. A. Estroff, J. K. Kriebel, R. G. Nuzzo and G. M. Whitesides. 'Self-assembled monolayers of thiolates on metals as a form of nanotechnology'. In: *Chemical reviews* 105.4 (2005), pp. 1103–1170.

[307] S. Terrettaz, Wolf-Peter Ulrich, H. Vogel, Q. Hong, L. G. Dover and J. H. Lakey. 'Stable self-assembly of a protein engineering scaffold on gold surfaces'. In: *Protein Science* 11.8 (2002), pp. 1917–1925.

[308] E. Ostuni, L. Yan and G. M. Whitesides. 'The interaction of proteins and cells with self-assembled monolayers of alkanethiolates on gold and silver'. In: *Colloids and Surfaces B: Biointerfaces* 15.1 (1999), pp. 3–30.

[309] L.R.S Barbosa, M. G. Ortore, F. Spinozzi, P. Mariani, S. Bernstorff and R. Itri. 'The importance of protein-protein interactions on the pH-induced conformational changes of bovine serum albumin: a small-angle X-ray scattering study'. In: *Biophysical journal* 98.1 (2010), pp. 147–157.

[310] A. Koichiro, S. Kenji, N. Shunji, K. Mitsuo and H. Koichi. 'Heat denaturation of bovine serum albumin in alkaline pH region'. In: *Biochimica et Biophysica Acta (BBA) - Protein Structure* 328.2 (1973), pp. 323–333.

[311] S. Heider, E. Reimhult and C. Metzner. 'Real-time analysis of protein and protein mixture interaction with lipid bilayers'. In: *Biochimica et Biophysica Acta (BBA) - Biomembranes* 1860.2 (2018), pp. 319–328.

[312] P. Jönsson, J. McColl, R. W. Clarke, V. P. Ostanin, B. Jönsson and D. Klenerman. 'Hydrodynamic trapping of molecules in lipid bilayers'. In: *Proceedings of the National Academy of Sciences* 109.26 (2012), pp. 10328–10333.

[313] H. Bruus. *Theoretical Microfluidics*. Jan. 2008, pp. 52–55.

[314] J. P. Brody, P. Yager, R. E. Goldstein and R. H. Austin. 'Biotechnology at low Reynolds numbers'. In: *Biophysical journal* 71.6 (1996), pp. 3430–3441.

[315] S.P. Sutera and R. Shalak. 'The History of Poiseulles's law, AnnualReview of Fluid Mechanics'. In: *25: 1* 19 (1993).

[316] *HP for tapered pores*. Accessed: 2022-03-15. URL: http://www.polymertechnology.it/bacheca/fluid/Slightly$%5C%$20tapered$%5C%$20tube_fds.pdf.

[317] Z. Dagan, S. Weinbaum and R. Pfeffer. 'An infinite-series solution for the creeping motion through an orifice of finite length'. In: *Journal of Fluid Mechanics* 115 (1982), pp. 505–523.

[318] T. Jovanovic-Talisman, J. Tetenbaum-Novatt, A. S. McKenney, A. Zilman, R. Peters, M. P. Rout and B. T. Chait. 'Artificial nanopores that mimic the transport selectivity of the nuclear pore complex'. In: *Nature* 457.7232 (2009), pp. 1023–1027.

[319] Y. Caspi, D. Zbaida, H. Cohen and M. Elbaum. 'Synthetic mimic of selective transport through the nuclear pore complex'. In: *Nano letters* 8.11 (2008), pp. 3728–3734.

[320] H. B. Schmidt and D. Görlich. 'Transport selectivity of nuclear pores, phase separation, and membraneless organelles'. In: *Trends in biochemical sciences* 41.1 (2016), pp. 46–61.

[321] A. N. Ananth, A. Mishra, S. Frey, A. Dwarkasing, R. Versloot, E. van der Giessen, D. Görlich, P. Onck and C. Dekker. 'Spatial structure of disordered proteins dictates conductance and selectivity in nuclear pore complex mimics'. In: *Elife* 7 (2018), e31510.

[322] S. Zeng, C. Wen, P. Solomon, S.-L. Zhang and Z. Zhang. 'Rectification of protein translocation in truncated pyramidal nanopores'. In: *Nature nanotechnology* 14.11 (2019), pp. 1056–1062.

[323] H. Bayley. 'Nanopore sequencing: from imagination to reality'. In: *Clinical chemistry* 61.1 (2015), pp. 25–31.

[324] S. W. Kowalczyk, L. Kapinos, T. R. Blosser, T. Magalhães, P. Van Nies, R. Y. H. Lim and C. Dekker. 'Single-molecule transport across an individual biomimetic nuclear pore complex'. In: *Nature nanotechnology* 6.7 (2011), pp. 433–438.

[325] S. Zeng, C. Wen, S.-L. Zhang and Z. Zhang. 'A nanopore array of individual addressability enabled by integrating microfluidics and a multiplexer'. In: *IEEE Sensors Journal* 20.3 (2019), pp. 1558–1563.